Charged hadron production in elementary and nuclear collisions at 158 GeV/c

Andrzej Rybicki

Ph.D. Dissertation

H. Niewodniczański Institute of Nuclear Physics
Kraków, March 2002

Mojej żonie

Abstract

A comparative study of p+p, p+Pb and Pb+Pb reactions is presented. For the first time, the same experimental apparatus is used for investigating the three reaction types.

Data on identified baryons in the projectile hemisphere of p+p and centrality-selected p+Pb and Pb+Pb collisions are shown. Information from pion-induced interactions is used to isolate the projectile role in the observed phenomena. A common picture emerges for p+p, p+Pb and Pb+Pb reactions: with increasing centrality, the projectile baryon number is strongly "pushed" towards the backward hemisphere of the collision.

Semi-inclusive data on identified pions in the forward hemisphere of p+p interactions are presented. The observed trends are compared to results on pion production in centrality-selected p+Pb and Pb+Pb reactions. It is argued that at least a part of effects observed in nuclear collisions can be explained by correlations present in p+p events. Conclusions about similarities and differences between elementary and nuclear reactions are drawn.

The obtained results are followed by an inspection of the role played by resonance production in inelastic hadronic collisions. This role appears significant in many of the observed phenomena. Resonance decays influence both pion and proton production in a wide region of available phase-space.

The contribution made to particle identification performance of the detector is described. It consists in a high precision calibration procedure, using radioactive ^{83}Kr gas. This method is also applied for studying various detector effects.

Contents

Chapter 1. Introduction

1.1　The current situation in soft hadronic physics

Among various domains of High Energy Physics, the investigation of low momentum transfer ("soft") hadronic interactions presents a very special challenge. Indeed, the detailed features of these reactions - building up the bulk of the total hadronic cross-section - cannot be derived *a priori* from quantum chromodynamics (QCD). The problem here is the large value of the effective coupling constant, which makes the use of perturbation methods impossible. This leads to a necessity of using phenomenological models in order to describe the data, in a hope that by eliminating wrong dynamical scenarios of the interaction one can get closer and closer to the experimental "truth".

A very large number of such models have appeared on the market during the past decades. Although this dissertation is not thought as a review of the whole phenomenology employed in order to describe the uncalculable soft processes (a review which, by the way, seems difficult to find), at least two separate approaches should be mentioned. Historically speaking, the first is the Regge method [1, 2] and the resulting models based on the exchange of Regge trajectories, like the multiperipheral Regge model [3]. This approach, although prior to QCD and therefore not based on e.g. the quark-gluon structure of the hadron, has proven successful as far as many phenomena are concerned. The second, more recent approach are the parton models, inspired both by QCD and by the e^+e^- and lepton+hadron deep inelastic scattering (DIS) results. The diversity of these models is very large [4]. Here we will quote the example of the Dual Parton Model (DPM), based on colour exchange between the projectile and target hadrons, and subsequent colour string fragmentation [5].

Despite all unsolved problems and the proliferation of possible dynamical scenarios of the soft interaction, the situation of the field still looked very attractive in 1983 [4]. In later years, however, a general "drawback" of the High Energy community from soft hadronic physics can be observed. The main reason for this might have been the internal complexity of hadronic interactions, which appeared to be such that the limited amount of experimental data did not make it possible to differentiate between various - partially contradictory - scenarios of their dynamics. It appeared in fact that several Monte-Carlo event generators, based on such scenarios [6, 7], have been more or less successful in describing the bulk of existing data.

Thus, no decisive information about the nature of soft processes has been provided so far, and at least a few crucial points remain still unclear. Several questions are still waiting for unambiguous answers, like for instance:

- what is the mechanism of colour exchange and colour neutralisation in hadronic collisions?

- what happens to the valence quarks of the projectile and target?

- what is the nature of the "intermediate" phase between the primary interaction and the final state hadrons?

A connection can be drawn between the generally poor level of knowledge discussed above and several other problems which remain unsolved. One example is that of differences between elementary hadron+hadron (h+h) and nuclear hadron+nucleus (h+A) and nucleus+nucleus (A+A) reactions. It

has been long believed that by studies of h+A collisions, one can get more insight into the space-time evolution of the strong interaction, and a rich phenomenology (partially described in reviews [4] and [8]) has been developed. It is nevertheless still unclear whether "new" phenomena, not observed in elementary reactions, are taking place in h+A. Another well-known problem closely connected with the latter is that of quark-gluon plasma (QGP) formation in high-energy A+A reactions [9]. According to several claims, such an intermediate state of deconfined quarks and gluons could have been obtained in heavy ion collisions at SPS energies [10]. According to other claims, however, the various phenomena interpreted as signatures of QGP formation could be explained by the Dual Parton Model without a necessity of invoking a qualitatively new state of matter [11]. Here again, it would seem that both the theoretical and experimental studies suffer strongly from a lack of well understood hadron+hadron and hadron+nucleus "reference", which could limit the freedom of existing model predictions.

In the eyes of a young newcomer, this situation seems quite unsatisfactory, and clearly appealing for more advanced experimental studies. In the lack of a quantitative theory, it seems indeed that the only chance to get more insight into the physics of soft processes is to put more constraints on the existing models, and thus to eliminate wrong dynamical scenarios. This is only possible if a detailed information, going deeper than the existing studies, is provided about various phenomena observed in hadronic collisions. Thus, the challenge of the field appears as much experimental as theoretical.

In order to face such a challenge, an appropriate set of data has to be provided. Seen as a whole, such a set should fulfil several requirements:

1. *versatility.* The dataset cannot be limited to one specific reaction like e.g. the p+p collisions. A full set of reaction types (like e.g.: p+p, π+p, p+A, π+A, A+A), is necessary to see the evolution of features of the strong interaction when going from simpler to more complex systems, and to get hold on their dependence on the projectile valence structure.

2. *impact parameter control.* The more complex interaction types (p/π+A, A+A), have to be studied with full use of the information on how the number of nucleons crossed by the projectile ("number of elementary subcollisions", "centrality") affects the features of the interaction.

3. *energy dependence.* The evolution of the strong interaction with available energy $\sqrt{s}$ is another valuable parameter, which can provide a way of differentiating between various scenarios of the hadronic collision dynamics.

4. *acceptance and hermeticity.* Already at the inclusive level, only a wide acceptance coverage can provide us with information about the details of particle production. Moreover, any study of the internal correlation structure of hadronic final states requires a reasonably hermetic detector, without large areas of low acceptance. It is important to underline that this *hermeticity* should not be limited to charged particles only. It should extend also to neutrals.

5. *particle identification* plays obviously a key role for both inclusive and non-inclusive studies, as the behaviour of various types of particles constitutes a natural way of testing the supposed mechanism of the collision (the phenomena of "baryon stopping" and of strangeness production can be quoted as two important examples). Here again, apart from charged particles, neutral final states like n or π^0 have to be identified.

6. *large statistics.* A detailed study of the inclusive behaviour and most of all, of the internal correlation structure of hadronic interactions requires large data samples, of an order of several million events.

In spite of the large amount of experimental effort invested in the field during the past decades, one has to state that the above requirements have so far been fulfilled at best only partially. The principal drawbacks of existing h+h and h+A datasets were mostly low statistics (typically below 500K events), an incomplete acceptance coverage and often inexisting or weak particle identification.

Centrality control in hadron+nucleus collisions has been available only in low statistics bubble chamber experiments and emulsion exposures. The situation is better for A+A data, as their collection is driven by the quark-gluon plasma search. However, what has been always lacking is a possibility of investigating the three basic hadronic reaction types: hadron+hadron, hadron+nucleus, and nucleus+nucleus, using the same experimental apparatus.

Thus, although a lot of versatile data has been collected ([4, 8, 12] may serve as partial reference), the gathered information remains incomplete. In the case of elementary h+h interactions, a lot of results have been obtained as far as their "inclusive surface" and energy dependence are concerned. With limited statistics, several experiments have investigated the internal correlation structure of hadronic events, but it remains far from being well understood. Precise information about the impact parameter dependence of h+A reactions is - to a large extent - missing. Possible connections between h+h and h+A, and their impact on our understanding of A+A collisions, are far from being explored.

Seen in this "historical" context of the general situation in soft hadronic physics, the NA49 experiment at the CERN SPS presents a sizeable step forward in the domain of experimental studies of soft processes. Originally aimed at examining central Pb+Pb collisions for signatures of QGP formation, its experimental programme has been extended with a systematic study of hadron+hadron, hadron+nucleus, and nucleus+nucleus reactions at various centralities and energies. The work described in this dissertation constitutes a part of this effort.

1.2   This study

The specific work presented in this thesis was inspired by the following questions:

- what is the role of projectile valence structure in hadronic collisions?
  Can it be isolated by comparison of reactions induced by different projectiles?

- what are the similarities and differences between h+h, h+A, and A+A reactions?
  Can one learn more about this problem with better data, e.g. on h+A centrality dependence?

- how does this relate to the internal correlation structure of elementary events?
  Can one learn more about this structure once particle identification is available?

- what are the possible ways of understanding the observed phenomena?
  Can one try to draw any conclusions about the dynamics of soft processes?

This work consists of a comparative study of p+p and centrality-selected p+Pb and Pb+Pb reactions, with additional use of π+p and π+Pb samples in specific parts of the analysis. Experimentally, it mainly focuses on the production of charged hadrons, that is pions and protons[1], and on their correlations. Due to its relatively wide scope, it is limited to a single beam energy of 158 GeV/n (corresponding, for a nucleon+nucleon collision, to a c.m.s. energy of $\sqrt{s_{\mathrm{N+N}}} \approx 17.3$ GeV).

Two basic aspects have now to be addressed. These are **a)** the *experimental possibilities* of NA49, that is, how well does it fulfil the requirements listed in Sec. 1.1, and **b)** the *strategy* applied in the study, that is, the exact objectives and the general line according to which they will be discussed.

1.3   The experimental possibilities

The NA49 fixed-target experiment at the CERN SPS provides a possibility of studying the projectile hemisphere of hadron+proton, hadron+nucleus and nucleus+nucleus collisions. The detector is shown

---

[1]As far as this dissertation is concerned, protons will also be called "produced" particles. This is quite natural in the inelastic sector where the connection between the projectile and final state proton is *a priori* unknown.
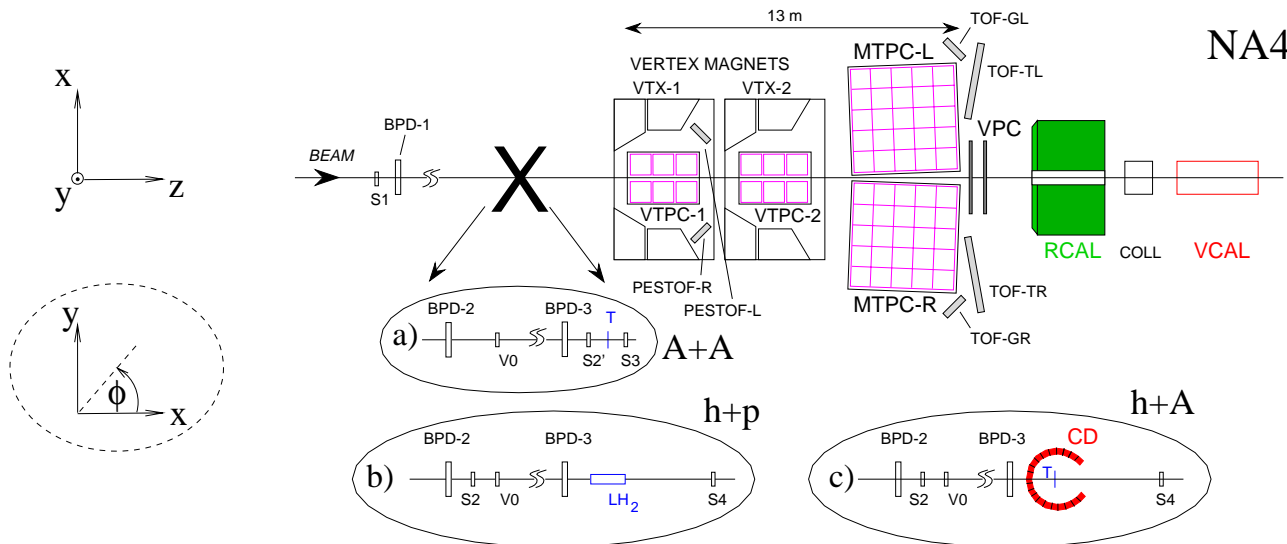
Figure 1: Set-up of the NA49 detector with different target arrangements for **a)** A+A, **b)** h+p, and **c)** h+A collisions. The Figure contains also the definition of the NA49 coordinate system and of the azimuthal angle ϕ.

in Fig 1. Its main components are four large acceptance Time Projection Chambers (TPC) providing charged particle tracking and identification (VTPC-1/VTPC-2, MTPC-L/MTPC-R), and a Ring Hadron Calorimeter (RCAL) for neutral particle identification. The detector is supplemented by Time of Flight (TOF) scintillator arrays to improve identification of charged hadrons in specific regions of phase-space, a set of two Vertical Proportional Chambers (VPC) for charged/neutral differentiation, and a zero-degree Veto Calorimeter (VCAL) for centrality triggering in A+A collisions. Depending on studied reaction type the target is either a liquid hydrogen tube (hadron+proton) or a thin metal foil (hadron+nucleus, nucleus+nucleus). In the special case of hadron+nucleus collisions, a Centrality Detector (CD) is placed around the target.

A detailed description of the NA49 detector can be found in [13]. Below are presented only some aspects of the experiment and of the collected data which are relevant for the study described in this thesis. For consistency, their ordering is similar to what has been presented in Sec. 1.1. For completeness, the problem of energy dependence is also briefly discussed.

1.3.1 versatility
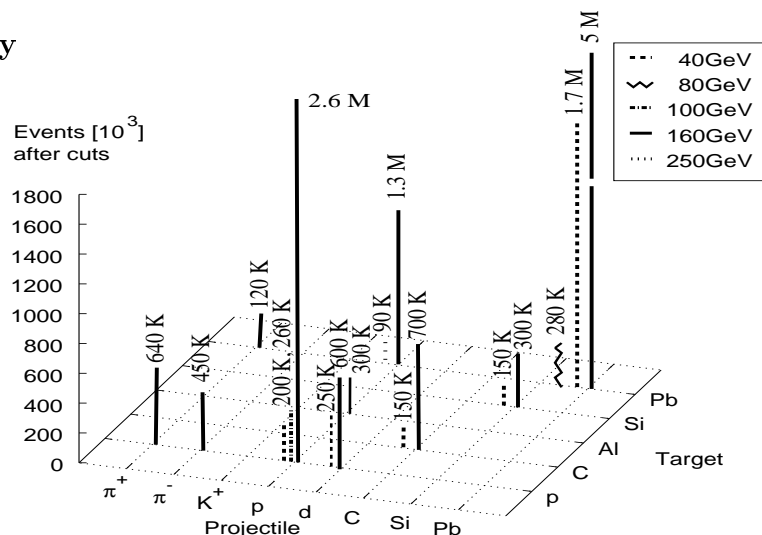

Figure 2: Data collected so far by NA49 - event sample size for different combinations of projectile, target and beam energy. Note: the Figure does not include the latest data collected in 2001.

As can be seen in Fig. 2, the total dataset collected by NA49 extends over a large variety of h+p, h+A and A+A reactions. Although very far from a saturation of the possible projectile-target

configurations, this gives already a possibility of studying the dependence of the interaction on system size and projectile type. This possibility will be exploited in Chapters 2 and 3.

The unique ability of NA49 of studying different collision types is made possible by the three target arrangements shown in Fig. 1, each of them related to a specific interaction trigger. Thus, for hadron+proton reactions, interactions with the target are selected by anti-coincidence of the incoming beam particle with the S4 scintillation counter (Fig. 1b). For inclusive - "minimum bias" - p+p interactions at 158 GeV beam energy, this defines a trigger cross-section of typically 29 mb. The trigger losses account for 85% of the elastic and 65% of the diffractive cross-section, both processes being anyway beyond the TPC tracking acceptance discussed in Sec. 1.3.4. For hadron+nucleus reactions, the h+p interaction trigger is strengthened by requiring a given number of hits in the Centrality Detector (Sec. 1.3.2). Finally, minimum bias A+A interactions are selected by anti-coincidence with the S3 Cherenkov counter (Fig. 1a). If required, additional on-line centrality triggering is available via the VCAL calorimeter.

It should be underlined that different reaction types are associated with different data taking and analysis problems. For A+A collisions, the principal problem is the high ionization density of the ion beam. It does not allow the beam to pass through the TPC chambers, and therefore forces the split configuration of the total NA49 TPC system (Fig. 1). A change of configuration between ion- and hadron-beam data-taking periods is practically impossible. This results in a partial loss of detector acceptance for all investigated collision types.

The h+p and h+A reactions present a specific difficulty due to their relatively low charged multiplicity (about 7 for p+p at E_{beam}=158 GeV, to be compared with about 1500 for central Pb+Pb). As the primary interaction vertex is reconstructed by back-extrapolating the TPC tracks, the efficiency and resolution of the reconstruction depends on the number of observed particles. This results in the necessity of applying multiplicity-dependent corrections, further described in Ch. 2.

1.3.2   impact parameter control
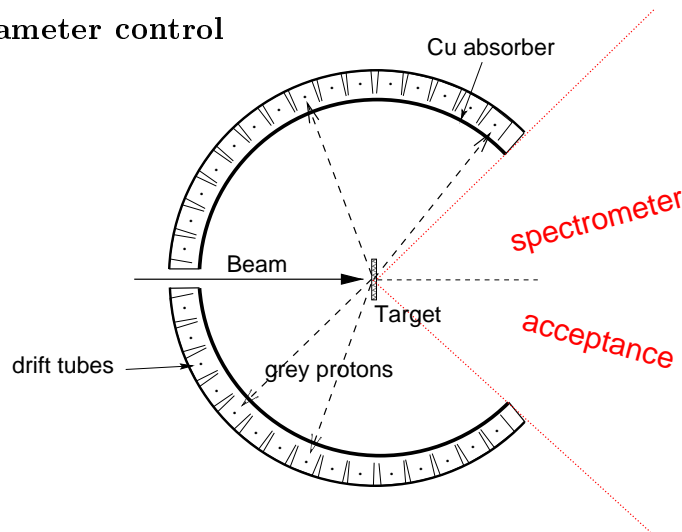
Figure 3: The Centrality Detector.

The on-line centrality selection in hadron+nucleus collisions relies on the measurement of the number of "grey" target protons in the laboratory momentum range of 0.15 to 1 GeV/c. The Centrality Detector dedicated to this purpose is a vertical cylinder composed of drift tubes surrounding the target foil (Fig. 3). In order to select grey protons falling in the CD acceptance, a Cu absorber eliminates by range the "black" evaporation protons and fragments. A cut in minimal pulseheight gets rid of faster ionizing particles (e.g. pions produced in the collision). The cylinder subtends lab polar angles from 45° to 315°, leaving free the NA49 TPC tracking wedge[2]. Grey protons entering this wedge are identified using the dE/dx method (described in detail in Sec. 1.3.5). The connection between the

---

[2]The total acceptance of the CD counter has been estimated to be about 40% of the produced grey protons [13].
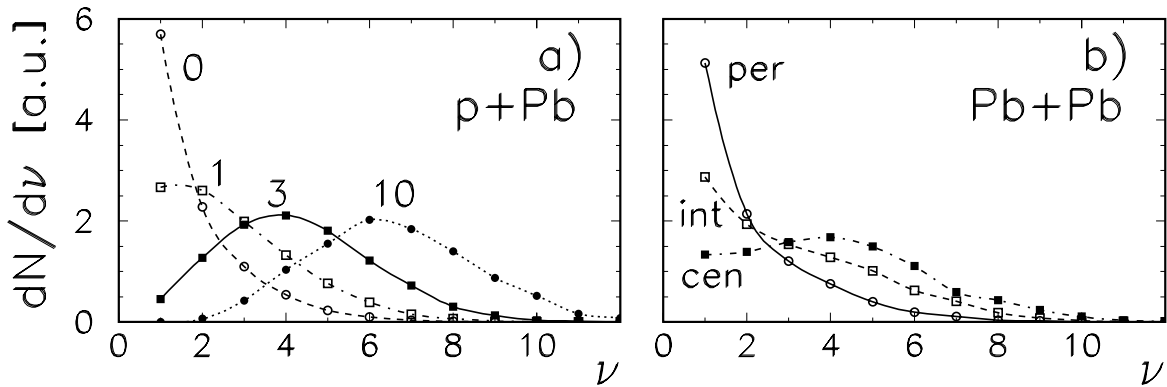
Figure 4: Exemplary distributions of the number of subcollisions ν (see text) for **a)** four p+Pb samples, selected by requiring respectively 0, 1, 3, and 10 grey protons registered by the CD detector, and **b)** three Pb+Pb samples (peripheral, intermediate, central), selected by the energy deposited in the VCAL calorimeter. Both distributions are obtained using the VENUS 4.12 event generator.

number of observed grey protons n_{grey} and the number of elementary subcollisions suffered by the projectile ν is traced using the VENUS 4.12 event generator [7], including a simulation of the detector response. Thus, each h+A data sample selected by a given number of observed grey protons can be characterised by the *mean* number of elementary subcollisions, $<\nu>$.

In nucleus+nucleus collisions, the on-line centrality selection relies on the energy deposit of beam fragments in the VCAL calorimeter. The connection between this energy deposit and the number ν of elementary subcollisions suffered by each nucleon participating in the A+A interaction, is again traced using VENUS. The number of such nucleons ("participants") can be directly obtained by estimating the net baryon number carried by produced particles [14]. Thus each centrality-selected A+A sample can be characterized either by the corresponding mean number of participants[3], or by the mean number $<\nu>$ analogically to the h+A case. In this dissertation this second possibility is chosen.

It should not be forgotten that for both h+A and A+A reactions, the $<\nu>$ values defined as above represent only the *mean values of broad and overlapping distributions*. This is illustrated by a few examples in Fig. 4.

1.3.3 energy dependence

As far as the investigation of $\sqrt{s}$ dependence is concerned, the principal NA49 limitation is the change of detector acceptance (in the interaction c.m.s.) with the change of beam momentum. As can be seen from Fig. 2, the so far collected data span over the beam energy range of 40 to 250 GeV/n, which corresponds to $\sqrt{s_{\mathrm{N+N}}}$ in the range of 8.8-21.7 GeV. Lower beam energy ion runs, down to 20 GeV/n ($\sqrt{s_{\mathrm{N+N}}} \approx 6.3$ GeV), are planned [15]. Proton runs at maximal SPS beam energy of 450 GeV ($\sqrt{s_{\mathrm{N+N}}} \approx 29.1$ GeV) could be considered.

1.3.4 acceptance and hermeticity

The total coverage of the combined NA49 TPC tracking system amounts to ca. 80% of charged particles produced in a hadronic interaction. Its laboratory momentum resolution dp/p^2 is typically below 10^{-3} $(\mathrm{GeV/c})^{-1}$ in the momentum range of 0.5-8 GeV/c. It is typically 3×10^{-5} $(\mathrm{GeV/c})^{-1}$ at higher lab momenta.

For practical purposes, the description presented below is made in the nucleon+nucleon c.m.s., assuming 158 GeV beam energy. The kinematical variables used are the Feynman variable $x_F = \frac{p_L}{p_{L\,max}}$, the transverse momentum p_T, and the azimuthal angle ϕ defined in Fig. 1.

Fig. 5 shows the average acceptance of the TPC system in the positive pion x_F-p_T plane. It is calculated using a Monte-Carlo based on parametrizations of the sensitive volume of the chambers obtained from physics data. A given (x_F, p_T, ϕ) point is accepted if the respective charged track crosses

---

[3]Note that the term "participant" used in this thesis refers to nucleons suffering *inelastic* subcollisions.
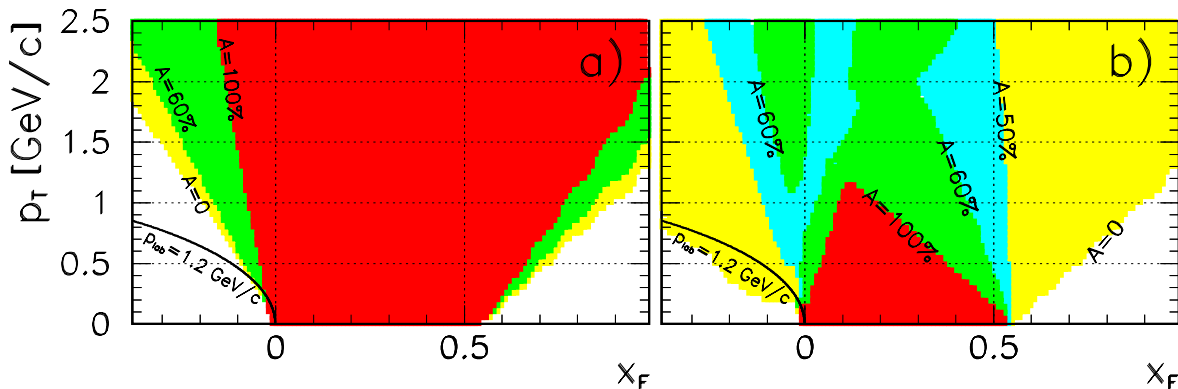
Figure 5: Geometrical acceptance of the combined NA49 TPC system for positive pions **a)** averaged over azimuthal angle ϕ in the range $|\phi| < 50°$, and **b)** averaged over the full azimuthal angle. The solid curves ($p_{lab} = 1.2$ GeV/c) will serve the discussion made in Sec. 1.3.5.

at least 30 pad rows (that is, potentially leaves 30 electron clusters) in all TPC's put together. The obtained acceptance $A(x_F, p_T, \phi)$ is then averaged over azimuthal angle as indicated in the Figure.

As can be seen from Fig. 5a, within a ϕ edge of $\pm 50°$, the TPC's provide a full acceptance covering the region $0 < x_F < 0.53$, $p_T < 2.5$ GeV/c. The x_F range extends further with increasing p_T. Without ϕ restriction acceptance losses appear, due to the horizontal separation of the TPC's (Sec. 1.3.1). Nevertheless, acceptance stays reasonably high at least up to $x_F = 0.4$ (Fig. 5b).

For negative pions, the situation is very closely symmetric to what is presented in Fig. 5. For protons, the acceptance coverage stays very similar to that for positive pions for forward x_F values, but extends further into the backward hemisphere (down to $x_F \approx -0.15$). Altogether therefore, for inclusive studies where cuts on ϕ can be applied, the TPC system provides full coverage for all charged particle types in the range $0 < x_F < 0.53$. The situation is more involved for correlation studies, where a reasonable coverage extends up to $x_F = 0.4$.

The forward hermeticity of the NA49 detector is ensured by the Ring Hadron Calorimeter. For the case of neutrons and protons at $x_F \geq 0.2$, this device provides full-azimuth acceptance up to $p_T = 1$ GeV/c. The p_T coverage further increases with x_F, up to 2.5 GeV/c at $x_F = 0.6$. Due to finite energy resolution of the calorimeter (typically 30%), special analysis techniques have to be used in order to obtain e.g. neutron spectra (discussed in Ch. 2). Due to particle density effects in A+A collisions, its use for single particle measurement stays limited to hadron-induced reactions.

1.3.5   particle identification (PID)
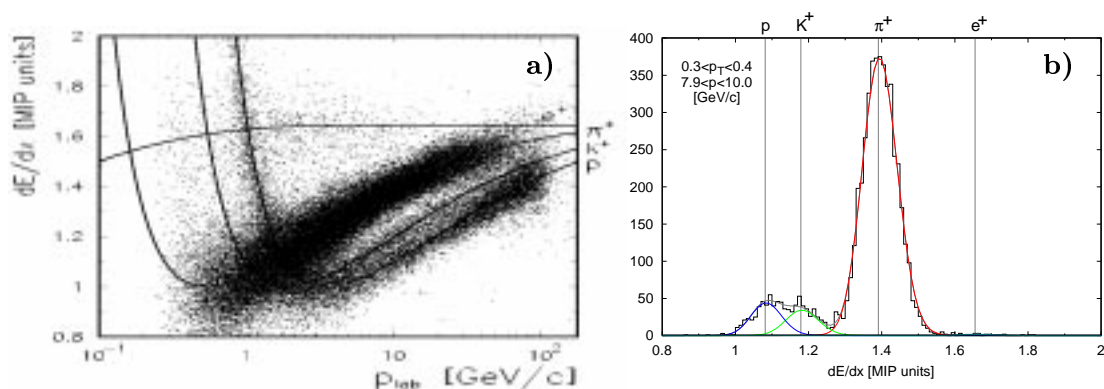
Figure 6: **a)** Truncated mean dE/dx as function of lab momentum for positive particles produced in p+p collisions at 158 GeV beam energy. The solid curves are energy loss functions described in the text. **b)** An example of truncated mean dE/dx spectrum in the relativistic rise region.

The identification of charged particles in the TPC system is achieved by measuring their specific energy loss in the TPC gas (*the dE/dx method*). This method consists in a measurement of charge

of all electron clusters belonging to a given track, and of the resulting energy deposit per unit length $dE/dx \sim dq/dx$. Then, a "trunctated mean" dE/dx characterising the track is calculated. As can be seen in Fig. 6a, the total lab momentum of the reconstructed tracks varies between a few hundred MeV/c up to about 100 GeV/c. Therefore the dE/dx measurement spans over the full range of the energy loss function from the $1/\beta^2$ dependence (e.g. grey protons entering the TPC) through minimum ionization into the relativistic rise up to the Fermi plateau (e.g. fast pions, electrons). In most of these regions the separation of various particle types (like protons and kaons in the example given in Fig. 6b) is indeed a challenging task due to the relatively small difference in expected truncated mean values. Thus a reliable PID requires an excellent resolution in the specific energy loss measurement, of the order of a few percent.

In order to achieve such a resolution, a 1% accuracy in the knowledge of detector response (both electronics and gas gain) is needed. This can be obtained by a dedicated method, using radioactive [83]Kr gas injected into the TPC volume, as shown in Fig. 7a. The [83]Kr isotope decays in the TPC gas with a characteristic energy deposit spectrum (Fig. 7b). The multi-peak structure of this spectrum is reflected in the resulting charge deposit spectrum, seen by the TPC readout in a given region of the chamber (Fig. 7c). Due to differences in detector gain, charge deposit spectra in different regions have different x scales: they are shrunk or stretched relative to each other (Fig. 7d). It is therefore possible to measure the local relative detector gain by comparing these spectra. Thus, a high-granularity calibration ("krypton calibration") of the TPC response can be achieved. In the case of NA49, this calibration is done on a single chip level. Additionally, the main systematics of gain variations inside the chips is taken out.

The krypton calibration of the whole NA49 TPC system (ca. 11,000 chips) has been an important part of the work described in this thesis. It has been performed for 1996, 98, and 99 krypton data, ensuring the high quality of NA49 dE/dx measurements and providing a detailed control of the long-range stability of the detector response. The details of this method, together with the principal results obtained, will be presented in Appendix A.
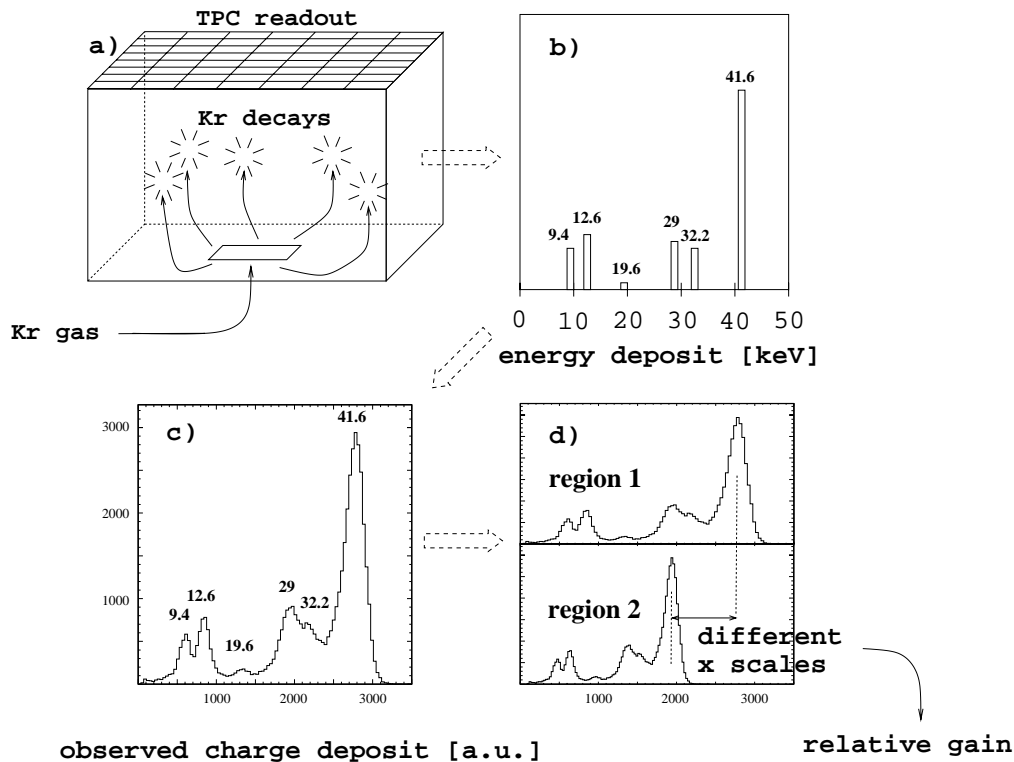

Figure 7: The logic of the krypton calibration procedure, as described in the text. Note: the peaks in the charge spectrum in panel c) correspond to energy deposit values given in panel b).

Apart from the krypton calibration, additional corrections have to be applied to the cluster charge, in order to take account of such detector phenomena as e.g. charge losses caused by electron attachment and by electronics threshold cuts. The optimized truncation procedure includes 50% of the smallest charge clusters in the truncated mean dE/dx. Then the effective energy loss functions (Fig. 6a) have to be obtained, which describe the expected truncated mean value for each particle type (e, π, K, p). These functions must be known with a precision better than 1% for the specific gas mixture in the NA49 TPC's, and must take account of various detector effects. Therefore, they are adjusted to physics data. As they preserve the main characteristics of the standard Bethe-Bloch formula [16] ($\beta\gamma$ scaling, general shape), they will be referred as "Bethe-Bloch functions" - for simplicity - in the following Chapters.

After the whole calibration procedure has been applied, the resolution in the measurement of the dE/dx truncated mean (relative to its expected value) is typically about $\sigma_{dE/dx} \approx 4\%$ in the p+p case, and $\sigma_{dE/dx} \approx 5\%$ in the Pb+Pb case. The worsening of the latter is caused by particle density effects. Its dependence on the number N of clusters on track is roughly $\sigma_{dE/dx} \sim 1/\sqrt{N}$. For reconstructed TPC tracks, N varies in the range of 10-234, and $\sigma_{dE/dx}$ depends strongly on p_{lab}, p_T, and ϕ. Using PID techniques described in Chapters 2 and 3, reliable identification is typically possible for $N \geq 30$, $p_{lab} \geq 1.2$ GeV/c. Thus, the full TPC PID coverage can be read from Fig. 5.

A completely separate problem is the identification of neutral particles, and of charged particles beyond the TPC acceptance. This is achieved by a combined use of the Ring Hadron Calorimeter and of the VPC chambers. The latter give a "veto" signal for charged particles entering the calorimeter. The particle charge is assigned accordingly to its "left-right" position relative to the beam (due to strong track bending the resulting misidentification effects can be neglected). Thus, for 158 GeV hadron beams, neutron identification is possible above $x_F = 0.2$. Below this value it becomes problematic due to K_L^0 contamination. As there is no $n/\bar{n}$ differentiation, assumptions about the $\bar{n}$ component have to be made (Ch. 2). Finally, information about forward protons ($x_F > 0.5$) also becomes available e.g. for p+p reactions, where π^+ and K^+ contamination can be neglected.

1.3.6   statistics

The total statistics of the NA49 dataset, available for analysis, has been presented in Fig. 2. In the context of the discussion made in Sec. 1.1, most of the samples allow for detailed studies on the inclusive level, and some of them have sufficient statistics for correlation analysis. These are for instance the p+p collisions at 158 GeV/c, the internal correlation structure of which will be investigated in Ch. 3. A more detailed discussion of the data samples selected for the study presented in this dissertation will be made in Sec. 1.4.

Let us sum up what has been said in this Section. In the context of requirements 1-6 made in Sec. 1.1, NA49 is definitely *not* the implicitly postulated "ideal experiment". Such experiments simply do not exist. The existing ones always constitute compromises between several constraints which usually are mutually contradictory - acceptance, beam intensity, cost, and others. NA49 has not escaped this universal rule. Let us however point at a few positive aspects of the compromises which it has achieved:

→ up to now, NA49 is the only experiment able to compare the projectile hemisphere for three basic hadronic reaction types in a single apparatus;

→ it is one of the two existing experiments providing large statistics h+A data with centrality control[4];

→ it is able to provide information about identified particles in a wide acceptance range;

→ a possibility exists to go deeper than the inclusive surface of soft processes, using the forward hermeticity of the detector with respect to charged and neutral particles.

The study presented in this thesis will exploit - partially - the possibilities presented above.

---

[4]The second experiment to be mentioned here is E910 at the AGS, measuring p+A reactions in the 6-18 GeV beam energy range [17].
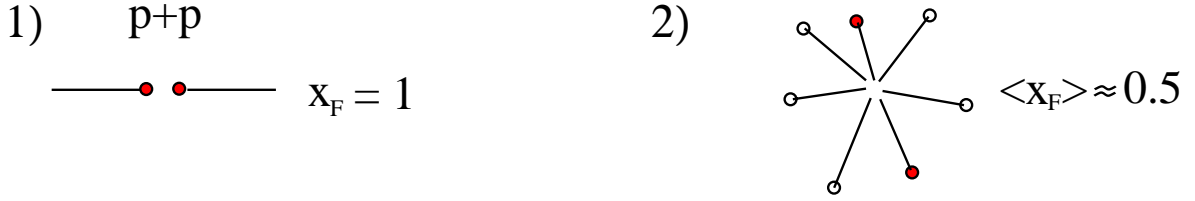
Figure 8: "Typical" inelastic p+p collision. Incoming protons at $x_F = \pm 1$ in the interaction c.m.s. After the collision, outcoming protons have a very wide x_F distribution with a mean value around $x_F \approx \pm 0.5$ in each hemisphere.

1.4 The strategy

The main aim of this Section is to discuss the general line along which the analysis described in this dissertation is organized. The resulting selection of used data samples will also be presented.

1.4.1 Role of baryon number conservation

The first subject to be addressed is the role which baryon number conservation plays in the presented study. Generally, its "usefulness" can be shown on the simplified example of Fig. 8. In any p+p collision, independently of its mechanism, the outcoming baryon number has to be equal to the incoming one. This trivial statement, however, says nothing about the baryon distribution over available phase-space. The *untrivial* experimental fact is that a phenomenon of *baryon number transfer* is taking place: at least as far as outcoming protons are concerned, the incoming net baryon number, positioned at $x_F = \pm 1$, may find itself even at very low $|x_F|$ values in the final state[5]. This fact will put constraints on the possible scenarios of the reaction. Any phenomenological model will have to provide answers to the following questions:

- what is the mechanism which transfers the projectile/target baryon number down to, e.g., $x_F = 0$?
- what does this say about the fate of the projectile and of its valence structure, originally responsible for its baryon number?

A given hypothetical mechanism of baryon number transfer will most likely be connected with the production of other particles. This opens a new way of verification of the model by investigating correlations between the two. Another possibility opens up when nuclear p+A collisions are considered. Here, the effect of baryon stopping - which could be called "increased baryon number transfer" - is present, indicating some kind of difference between the dynamics of p+p and p+A collisions. This again puts experimental constraints on models and thus tests their predictive power.

It seems therefore that if a deeper insight into the dynamics of soft processes is to be gained, a detailed analysis of baryon number transfer, its centrality dependence and its correlation to other observed phenomena, constitutes a good starting point. This fact finds its reflection in the study presented here, focussed at baryon number transfer and its connection to charged pion production.

Before continuing the discussion, additional remarks should be made. Experimental studies of baryon number transfer are more complicated than the simplified situation presented in Fig. 8. This has two main reasons:

- at beam energies high enough, the problem of baryon-antibaryon ($B\bar{B}$) pair production appears, thus the "net" baryon number distribution has to be isolated.
- the total baryon number is not limited to final state protons, but divided between protons and other baryon types (neutrons, hyperons). The latter are usually more difficult to measure.

This thesis will address both problems.

---

[5]As far as this dissertation is concerned, the term "baryon number transfer" should not be understood as "exchange of baryon number". The meaning of this term is limited to the experimental observation described in the text.

1.4.2 The objectives

What has been said in Sec. 1.4.1 defines the line of analysis and discussion which is presented in this thesis. This line consists of the following objectives:

a) study of baryon number transfer in p+p reactions. Comparison to π+p collisions in order to investigate the dependence of the phenomenon on the projectile valence structure.

b) application of the knowledge obtained in (a) for exploring the centrality dependence of baryon number transfer in p+Pb and Pb+Pb collisions. Investigation of differences and similarities between p+p, p+Pb and Pb+Pb.

c) study of correlation between baryon number transfer and charged pion production in p+p interactions. Comparison of the obtained results to the centrality dependence of pion production in p+Pb and Pb+Pb reactions.

d) investigation of connections between the observed effects and other known phenomena, specifically resonance production in p+p collisions.

The whole analysis is limited to *inelastic* elementary and nuclear collisions. For experimental reasons, the study of pions is limited to the projectile hemisphere of the interaction. For protons, it is extended down to $x_F \approx -0.1$.

1.4.3 The data

The total set of NA49 physics data used in this study is in fact the minimum required to accomplish the objectives described above. It consists of p+p, π+p, p+Pb, π+Pb, and Pb+Pb data at a single beam energy of 158 GeV/n. The data samples are listed in Table 1. Apart from the total statistics available for analysis, the typical size of centrality-selected samples is also given. In order to complete the picture, the Table includes the typical size of p+p sub-samples used in correlation studies.

It should be pointed out that not all the results based on this very large dataset and presented in the following Chapters have been obtained within the framework of this thesis' work. With kind agreement of the authors, many other results have been included without which the discussion would be incomplete. All these results will be enumerated at the beginning of each Chapter. The description of the corresponding data analysis and systematic errors will be included if relevant for the discussion.

reaction	total statistics (events)	typical statistics after centrality selection (events)	typical sub-sample size in correlation studies (events)
p+p	2,541,000	-	25,000 - 80,000
π^++p	639,000	-	-
π^-+p	447,000	-	-
p+Pb	845,000	50,000 - 200,000	-
π^++Pb	118,000	28,000	-
Pb+Pb	121,000	20,000	-

Table 1: NA49 physics data samples used in this thesis. All reactions were collected at the same beam energy of 158 GeV/n. The table does not include krypton calibration data discussed in Appendix A.

1.4.4 Data presentation

Unless explicitly specified, the kinematic variables used in the following Chapters are calculated in the nucleon+nucleon c.m.s. Unless specified, the presented error bars are only statistical. Unless specified, all lines and curves added to the plots serve only to guide the eye.

1.5 The outline of this thesis

The remainder of this dissertation is organized as follows:

Chapter 2 contains a study of baryon number transfer in elementary (p+p, π+p) and nuclear (p+Pb, π+Pb, Pb+Pb) collisions.

In Chapter 3, an analysis of the correlation between baryon number transfer and charged pion production in p+p interactions is presented. It is followed by a study of centrality dependence of charged pion production in p+Pb and Pb+Pb reactions.

In Chapter 4, additional information concerning hadronic resonance production in p+p interactions is included. The role of resonance decays in some of the observed phenomena is investigated.

Finally, Chapter 5 contains a summary of the obtained results and a short outlook.

This dissertation contains two appendices. In Appendix A, the main aspects of krypton calibration of NA49 TPC's are presented. Appendix B describes a few specific details of baryon number transfer studies.

Chapter 2. Baryon Number Transfer

This Chapter contains a study of baryon number transfer in both elementary and centrality-selected nuclear collisions. A comparison of p+p and π+p interactions is made in order to isolate the role of the projectile, and also of the target, in the observed phenomena. This serves as a basis for a study of the baryon stopping effects in proton+nucleus and nucleus+nucleus collisions. Conclusions about the basic characteristics of baryon number transfer in p+p, p+Pb and Pb+Pb reactions are drawn.

Most of the study is based on "net" proton $(p - \bar{p})$ x_F spectra[1], but the discussion includes also neutron data. On top of the results obtained within the framework of this thesis (all the presented p+Pb and π^++Pb net proton data), the discussion is supplemented with a large number of results coming from independent analyses. These are preliminary net proton spectra in p+p and π+p collisions [18], in Pb+Pb reactions [19], and preliminary neutron spectra [20]. As this is important for the discussion, some of these analyses will be briefly described, and an estimate of their systematic errors will be presented.

2.1 Elementary collisions

This Section describes the behaviour of $p - \bar{p}$ spectra in inclusive (minimum bias) p+p, π^++p, and π^-+p reactions. First the data analysis and then its results are presented.

2.1.1 Data analysis

dE/dx fits. The inclusive p and $\bar{p}$ yields used for $p - \bar{p}$ studies are extracted by fitting truncated mean dE/dx distributions in appropriately defined bins of phase space (Fig. 9).
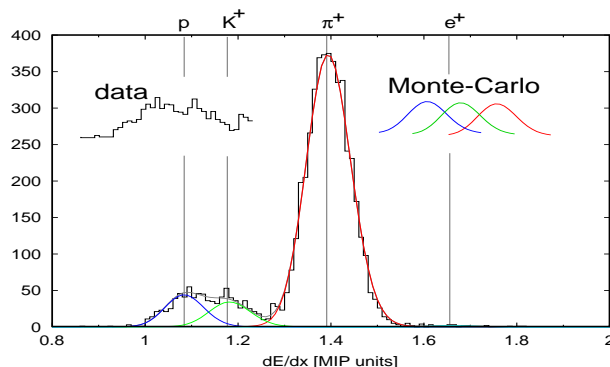

Figure 9: An example of dE/dx spectrum together with adjusted Monte-Carlo curves and positions of the e^+, π^+, K^+ and p Bethe-Bloch functions.

The logic of this method is the following: for a given bin $(x_F, x_F + \Delta x_F)$ where the proton yield is to be measured, a specific region of the (p, p_T) space is defined, corresponding to this x_F bin under the assumption that all particles are protons. Positively charged particles (TPC tracks) belonging to that region are used to fill the dE/dx spectrum. This spectrum is then fitted using Monte-Carlo distributions (Fig. 9) which describe the detector response in detail. The free parameters of the fit are the numbers of e^+, π^+, K^+ and p contributing to the spectrum. The input parameters of the Monte-Carlo are the positions of the four Bethe-Bloch functions (Ch. 1) and an overall resolution parameter. These input parameters can be modified if required. Thus, possible imperfections of

---

[1]The usage of $p - \bar{p}$ spectra seems to be the simplest way to eliminate the effect of baryon-antibaryon pair production in baryon number transfer studies. The problem is in fact untrivial and will be discussed in Appendix B.
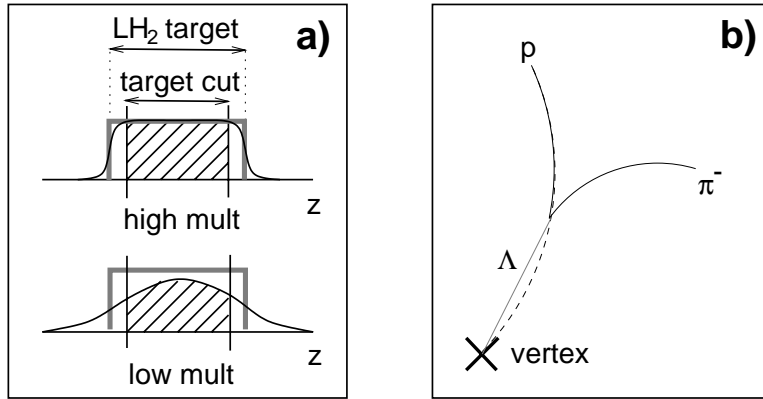
Figure 10: **a)** Reconstructed interaction vertex z distribution (solid curve) for the high and low multiplicity cases, together with the contour of the liquid hydrogen target tube. Events available for analysis (falling in the target cut) are marked by the filled area. **b)** Example of hyperon feed-down to measured proton spectra.

the dE/dx calibration procedure, like slightly wrong Bethe-Bloch adjustments, are corrected at the analysis stage.

As has been shown in Ch. 1, the acceptance of the TPC system depends on azimuthal angle ϕ. For this reason, the analysis is restricted to azimuthal wedges assuring full acceptance with at least 30 electron clusters ("points") on each TPC track. Note that the above restriction can be applied due to azimuthal symmetry of the results. In order to make full use of available statistics, the azimuthal wedges are adjusted separately for each x_F bin.

The obtained proton yields are corrected for azimuthal cuts. Then, they are divided by the bin width Δx_F, and normalized to the total number of events in the data sample. This results in the final $\frac{1}{N_{events}}\frac{dN}{dx_F}$ values, labeled "dN/dx_F" for simplicity. The present estimate of systematic precision of proton dN/dx_F yields is typically 4% for p+p, and 5-7% for π+p reactions. An exactly analogous method is used for antiproton dN/dx_F yields. A precision of 10% (p+p) and 5-7% (π+p) is estimated in this case.

Due to space limitations, the contribution of this thesis' work to the development of the dE/dx fit methods is not presented in this dissertation. Additional information can be found in [21].

Corrections. The methods applied to obtain various corrections used in this analysis will be described in great detail in two Ph.D. theses [22]. Below only their basic aspects are discussed.

Vertex losses. As has been said in Ch. 1, the resolution of the interaction vertex reconstruction depends on the event charged multiplicity n_{ch}, as seen by the NA49 TPC system. The situation is schematically drawn in Fig. 10a. For triggered low multiplicity p+p (π+p) events, the vertex z position is more smeared and consequently escapes the target cut, placed in order to avoid e.g. events originating in the target walls. Additionally, for very low multiplicities, it may happen that the reconstruction software will completely fail to reconstruct the interaction vertex. Both effects need to be corrected for. This is done by measuring the vertex resolution in z as function of n_{ch}, and by comparing the number of triggered events to that of reconstructed ones, again as function of n_{ch}. The resulting correction factors are typically of an order of several per cent, but strongly increase with decreasing multiplicity. Due to this strong dependence on n_{ch} they have to be applied on an event-by-event basis: each particle entering the dE/dx spectrum in Fig. 9 has to be weighted up by an appropriate correction factor. Taken account of the finite accuracy of correction factors' measurement, the resulting systematic error of net proton spectra is estimated to about 1-2%, plus an additional 1% normalization uncertainty.

Trigger losses. As has been described in Ch. 1, the NA49 minimum bias h+p trigger does not cover 100% of the total inelastic cross-section. The non-triggered events are mostly diffractive, and it is not expected that they will significantly contribute to particle multiplicities observed within the

TPC acceptance. Nevertheless, in order to obtain inclusive dN/dx_F spectra ($\frac{1}{N_{events}}\frac{dN}{dx_F} = \frac{1}{\sigma_{inel}}\frac{d\sigma}{dx_F}$), these non-triggered events have to be accounted for in their *normalization*. The finite precision of the trigger cross-section measurement results in a normalization uncertainty, estimated to 4-5% and 5-6% for respectively p+p and π+p reactions.

Hyperon feed-down. A very important problem in obtaining p and $\bar{p}$ spectra is that of contamination of the obtained distributions by products of weak decays of hyperons produced in the collision (like $\Lambda/\bar{\Lambda}$ and $\Sigma/\bar{\Sigma}$). The problem is illustrated in Fig. 10b. The Λ hyperon decays away from the primary interaction vertex, but the reconstruction software "manages" to fit the decay proton back to the vertex. This proton is then assigned as originating from the interaction point, and contaminates the experimental proton spectrum. This contamination can be large and depends strongly on x_F. In p+p reactions, at $x_F = 0$, some 9% of protons and 18% of antiprotons assigned as "vertex tracks" originate in fact from Λ, Σ and $\bar{\Lambda}, \bar{\Sigma}$ decays.

In order to cure the problem, a dedicated Monte-Carlo has been developed, which simulates the emission and decay of $\Lambda/\bar{\Lambda}$ and $\Sigma/\bar{\Sigma}$ particles. These are generated according to inclusive distributions adjusted to a wide compilation of published data on hyperon production in p+p and π+p collisions. The decay modes taken into account are $\Lambda^0 \rightarrow p\pi^-$, $\bar{\Lambda}^0 \rightarrow \bar{p}\pi^+$, $\Sigma^+ \rightarrow p\pi^0$, and $\bar{\Sigma}^- \rightarrow \bar{p}\pi^0$. The probability of a daughter proton (antiproton) to be fitted back to the vertex is obtained from a detailed GEANT [23] simulation of the NA49 detector, upon which the NA49 reconstruction software is applied. The outcome of the whole procedure are x_F distributions of wrongly assigned p and $\bar{p}$, which can be subtracted from experimental spectra.

The systematic uncertainty of this correction corresponds to the accuracy to which the hyperon cross-sections and distributions are known. For net proton spectra, typical estimates of resulting systematic errors are about 1% (p+p), 2% (π^++p), and 3% (π^-+p).

Total systematic errors. An overall calculation of systematic uncertainties coming from different sources is quite untrivial due to their non-statistical character. The rough estimates given in Table 2 are obtained by adding in quadrature all systematic error sources for all x_F bins used in the analysis. In the Table, a few representative values are listed. Overall estimates of normalization errors are given separately. The main ingredient in the presented values is the dE/dx uncertainty discussed above. For the case of π^-+p collisions, the very large value of *relative* systematic uncertainty at $x_F \approx 0.2$ (marked * in the Table) is due to a very small value of the *difference* between p and $\bar{p}$ distributions, as shown in Sec 2.1.2.

reaction	$p - \bar{p}$ systematic error			normalization error
	$x_F \approx 0$	$x_F \approx 0.2$	$x_F \approx 0.4$	
p+p	6%	5%	5%	5%
π^++p	11%	14%	16%	6%
π^-+p	16%	>50%(*)	13%	6%

Table 2: Estimates of total systematic errors of net proton dN/dx_F spectra in p+p and π+p reactions.
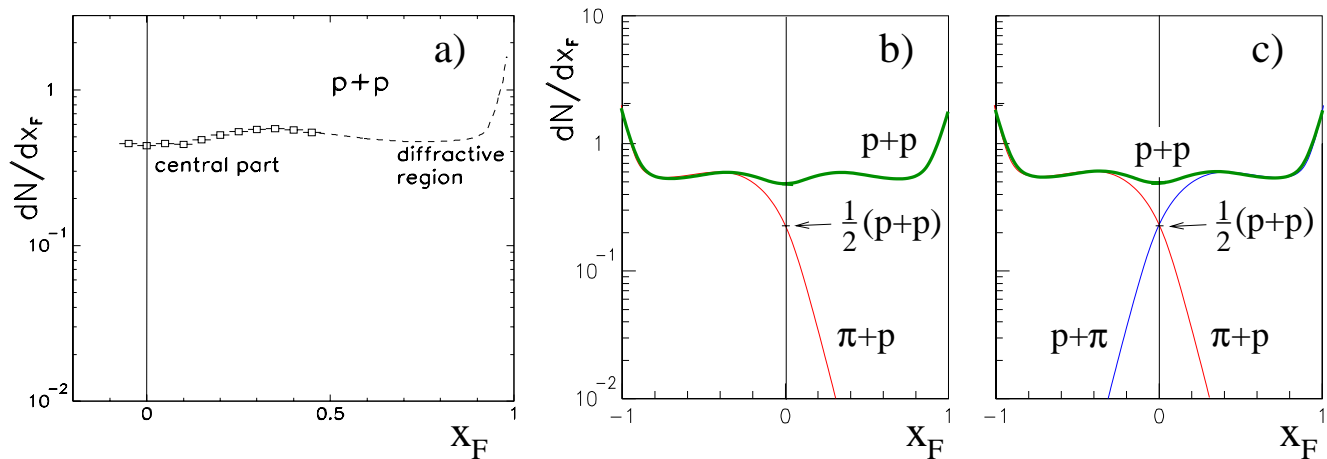
Figure 11: **a)** Net proton spectrum in p+p collisions. Outside the limit of the TPC acceptance, the NA49 data (squares) are supplemented with a compilation of existing results (dashed curve, based on [24]). Note: the data point at $x_F = -0.05$ is a reflection of the measurement made at $x_F = 0.05$. **b)** Hypothetical comparison of net baryon spectra in p+p and π+p reactions. **c)** Same comparison as in panel b), with a reflected "p+π" curve added to the plot.

2.1.2 A two-component picture of net proton spectra

This Section presents the results of the analysis described above.

A good starting point for studying the phenomenon of baryon number transfer in hadronic collisions is the longitudinal net proton spectrum in inelastic p+p reactions (Fig. 11a). The distribution can be divided into two parts: a "diffractive region" at high $|x_F|$ values, and a "central part" for lower $|x_F|$. In the diffractive region, the interaction is considered to proceed via the excitation of one or both of the colliding protons into "clusters" inheriting their quantum numbers. Each of the clusters gives rise to final state particles [4]. Thus in that region, the baryon number transfer occurs separately for the projectile and target. In diffractive events, the x_F distribution of final state baryons could be divided into two separate components: one of them could be attributed exclusively to the target, the other to the projectile.

The main interest of this study is not the diffractive but the central region. A basic question is whether some analogous *two-component picture* could not be valid also for the non-diffractive part of baryon spectra. Can one still speak of baryon number transfer occuring separately for the projectile and target, or do the two valence structures become "melted" in a way that no separation is anymore possible[2]?

Let us formulate a simple hypothesis (Fig. 11b). Let us assume that we have full knowledge of the net baryon $(B - \bar{B})$ spectrum in p+p and π+p interactions. Let us conjecture that the π+p distribution behaves as shown in the Figure: it approaches the p+p spectrum in the backward region, reaches $\frac{1}{2}$ of the p+p value at $x_F = 0$, and decreases in the forward direction. In such a case we would have reasons to suppose that the p+p spectrum can in fact be *separated* into two components, as shown in Fig. 11c: the π+p distribution, and the reflected "p+π" spectrum.

In both π+p and p+π interactions, the baryon number transfer can occur *uniquely* from the proton target or projectile. Thus, we could draw the following conclusions:

→ the net baryon spectrum in p+p reactions is a sum of two components which can be attributed to the target and to the projectile. Let us label them as "projectile component" and "target component".

→ the target component is identical in p+p and π+p reactions.

→ it is possible to obtain the "pure" projectile component in p+p by subtracting the target component from the total spectrum.

---

[2]The two-component picture discussed here should not be mistaken for the one formulated by Fiałkowski and Kittel for inclusive particle and resonance production [4].
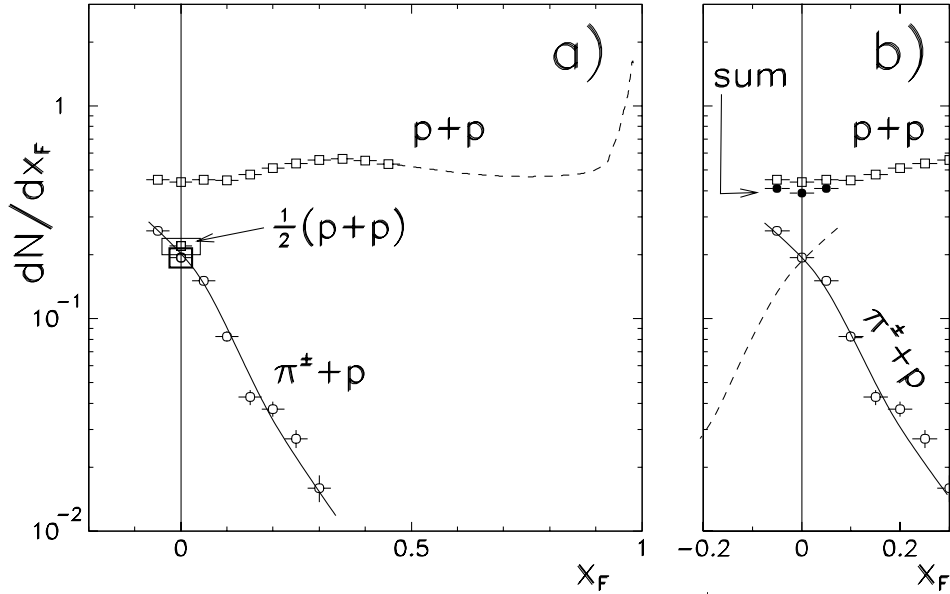
Figure 12: **a)** Net proton spectrum in p+p (shown before) and in $\pi^{\pm}$+p (see text). At $x_F = 0$, $\frac{1}{2}$ of the p+p value is marked. Note: the rectangles at $x_F = 0$ illustrate the systematic error of the two measurements (only their vertical size is meaningful). **b)** The same p+p spectrum, compared to the sum (dots) of the $\pi^{\pm}$+p distribution and of its reflection with respect to $x_F = 0$ (dash).
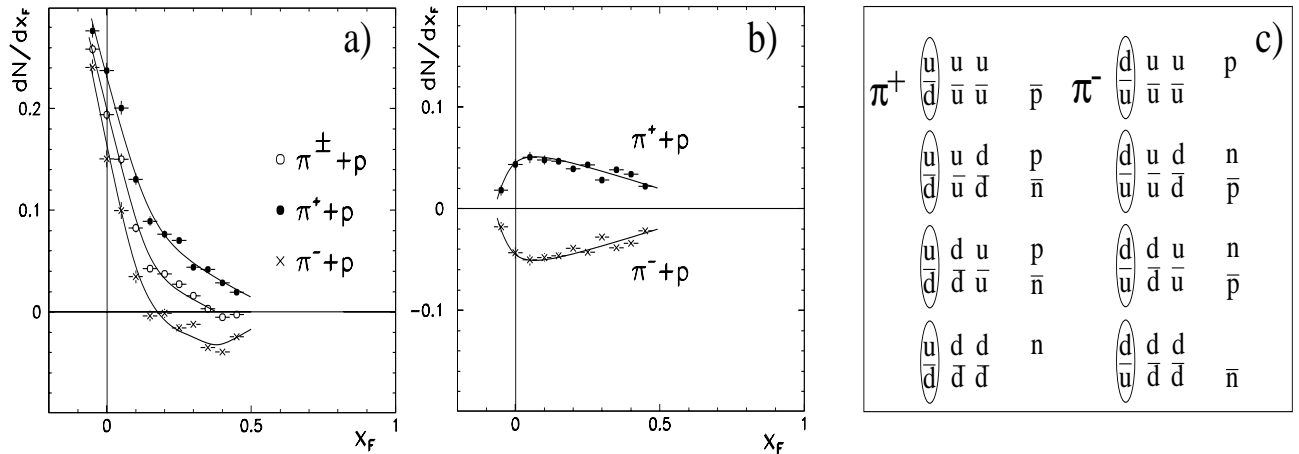

Figure 13: **a)** Net proton spectra in π^++p and π^-+p reactions, and their mean value: $\pi^{\pm}$+p. Note: a negative dN/dx_F value means that more antiprotons than protons are observed. **b)** Difference from the mean for π^++p and π^-+p reactions. **c)** Scheme of $B\bar{B}$ pair production based on the projectile pion valence structure. Note that the number of produced net protons $(p - \bar{p})$ is opposite for π^+ and π^-.

The hypothesis presented above is verified in Fig. 12a, using experimental net proton spectra. The hypothetical "π+p" curve from Fig. 11b is represented by the mean value of net proton x_F distributions in π^++p and π^-+p collisions. It is labeled "$\pi^{\pm}$+p". Note that at $x_F = 0$, it reaches $\frac{1}{2}$ of the p+p value within an accuracy comparable to experimental errors. Within this accuracy, Fig. 12a repeats what has been shown in Fig. 11b. In the very limited available x_F range (Fig. 12b), the *sum* of π+p and p+π distributions also behaves as expected. With the present accuracy, the two-component hypothesis is not contradicted by the data.

This hypothesis can be further verified. In Fig. 13a, the two ingredients of the mean $\pi^{\pm}$+p spectrum are presented: the $p - \bar{p}$ distributions for π^++p and π^-+p collisions. The two curves come close in the backward hemisphere, but show a sizeable difference in the forward region. After the subtraction of the mean $\pi^{\pm}$+p spectrum, a set of two curves is obtained (Fig. 13b). It is by definition antisymmetric and will be labeled "π^+/π^- antisymmetric component". It is well localised in the projectile hemisphere of the collision, and decreases for $x_F < 0$.

What is presented in Figs 13a-b seems to spoil the two-component picture hypothesis proposed

17

above. In this picture, the net baryon spectrum in any pion+proton reaction should contain only a target component - it should be independent of the projectile. The π^+/π^- antisymmetric component should not exist. The question is: where does it come from?

It should be remarked that baryon number conservation in baryon-antibaryon pair production does not necessarily require a symmetric production of protons and antiprotons. Specifically, the fact that non-baryonic projectiles (π^+, π^-) lead to different yields of observed p and $\bar{p}$ could be explained by an asymmetry in production of $p\bar{p}$, $n\bar{n}$, $n\bar{p}$ and $p\bar{n}$ pairs. Following this line of reasoning, a connection can be drawn between the π^+/π^- antisymmetric component and the valence structure of the pion projectile. This is illustrated in Fig. 13c. Assuming a production of $B\bar{B}$ pairs originating directly from the pion, an asymmetry in p and $\bar{p}$ production is indeed to be expected. Its behaviour for the two projectile types, i.e.:

$$Number\ of\ produced\ net\ protons\ (\pi^+)\ =\ -\ Number\ of\ produced\ net\ protons\ (\pi^-)$$

is just what is being observed for the π^+/π^- antisymmetric component! Thus, the latter can be explained by asymmetric pair production, *and attributed directly to the projectile*. The two antisymmetric curves from Fig. 13b will be the *projectile components* of net proton spectra in respectively π^++p and π^-+p reactions. As is immediately apparent from Fig. 13c, the symmetrized $\pi^\pm$+p curve will be free from any such "projectile pair production" ingredient. Therefore it can be attributed to the target.

Thus, the behaviour of π^++p and π^-+p collisions taken *separately* is also consistent with our hypothesis of the two-component picture of net proton spectra. In this picture, the target component would be represented by the mean $\pi^\pm$+p curve and would be common to p+p, π^++p, and π^-+p reactions. The projectile component would be different for each projectile, represented by the symmetrically reflected $\pi^\pm$+p curve in the p+p case, and by the π^+/π^- antisymmetric curves for pion+proton collisions. For *non-baryonic projectiles*, the projectile component would not reflect the transfer of baryon number but asymmetric pair production.

The aim of the next Section will be to verify whether the findings presented above can shed any new light on the baryon stopping effects observed in p+A and A+A reactions.

2.2   Baryon stopping in nuclear collisions

This Section contains an analysis of net proton distributions in centrality-selected nuclear collisions. The study is supplemented by preliminary net neutron spectra. After a description of the data analysis methods the results of the study are presented. First hadron+nucleus (p+Pb, π^++Pb), and then nucleus+nucleus (Pb+Pb) collisions are discussed.

The study presented here is subject to a few experimental limitations. The principal ones are the lack of π^-+Pb data (not yet available), and a relatively low statistics of π^++Pb data (only ca 20,000 events per centrality-selected sample). Therefore, a more precise "final word" analysis has still to come. Nevertheless, the systematic accuracy of the presented results (Sec. 2.2.1) is already good enough to allow for several conclusions made in the next Sections.

For simplicity, the discussion made here assumes that asymmetric $B\bar{B}$ pair production effects, postulated in Sec 2.1 for π+p reactions, can to first order be neglected for p+p, p+Pb, and Pb+Pb collisions. This assumption could be justified by the relatively low importance of pair production at $\sqrt{s_{\mathrm{N+N}}} \approx 17.3$ GeV. The impact of this problem on the presented results is discussed in Appendix B.

2.2.1   Data analysis

This presentation of data analysis focuses on methods applied to obtain $p - \bar{p}$ spectra in p+Pb and π^++Pb reactions. A short discussion of the included p+p and p+Pb neutron data is also presented. A summary of the Pb+Pb data analysis, and a preliminary estimate of systematic errors, can be found in [19].
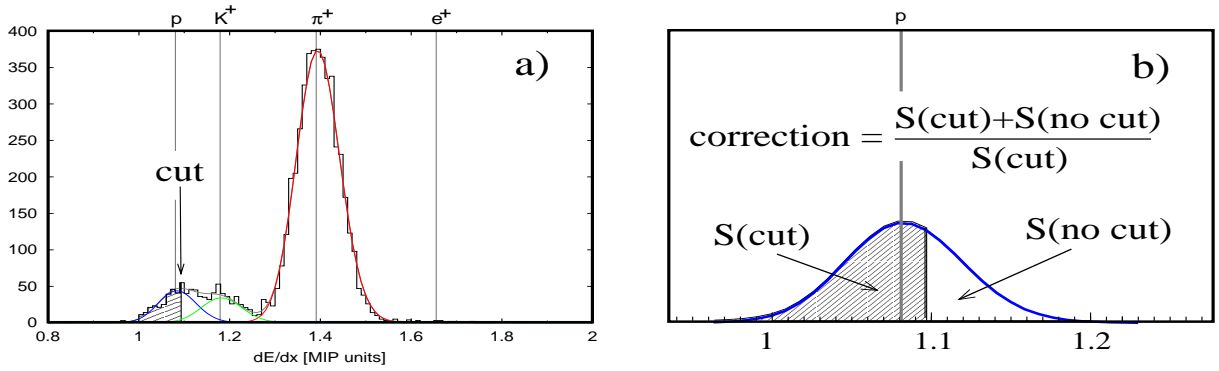
Figure 14: **a)** Simplified illustration of the dE/dx cut method. The contributions of different particle types to the total spectrum, and the respective positions of the four Bethe-Bloch functions, are also marked in the plot. **b)** Magnification of the p contribution from panel a): correction for cut losses.

dE/dx cuts. The p and $\bar{p}$ yields have been obtained by selection of highly enriched proton and antiproton samples. This has been achieved by appropriate cuts on the truncated mean dE/dx. This method induces higher systematic uncertainties than the dE/dx fit discussed in Sec. 2.1.1, but it is not limited by statistics and therefore can be applied to the currently available $\pi^+ +$Pb data. For practical reasons, this analysis procedure is also faster by an order of magnitude.

The method is schematically illustrated in Fig. 14a. Applying an appropriate cut on the positive particle dE/dx spectrum, a highly enriched proton sample is obtained. The number of thus selected "proton candidates" is then multiplied by an appropriate correction factor. This factor compensates for protons remaining outside the cut, as shown in Fig. 14b. In the present analysis, the p and $\bar{p}$ candidates are selected by a cut of $(-3\sigma, +0.5\sigma)$ around the proton/antiproton Bethe-Bloch value, σ being the absolute value of the dE/dx resolution. Note that σ depends on the number N of points on TPC track (Ch. 1). For a fixed N, the shape of the $e/\pi/K/p$ contribution curves shown in Figs 14a and 14b is very close to Gaussian[3], with a st. deviation equal to σ. Thus the correction factors can easily be computed.

The analysis is restricted to an azimuthal wedge of $|\phi| < 50°$ for positives, and an identical wedge around $\phi = 180°$ for negatives. In the investigated x_F range, this insures a 100% acceptance with minimum 30 points on TPC track (see discussion in Ch. 1). Similarly to Sec. 2.1.1, the obtained yields are corrected for azimuthal cuts. Then, they are divided by the x_F bin width, and normalized to the number of events in the given centrality-selected data sample.

The dE/dx cut method is subject to two principal sources of systematic error. The first is *kaon contamination*, i.e. misidentification of kaons as proton candidates (see the K^+ curve extending to the cut region in Fig. 14a). The second problem is the *limited precision of adjustment of Bethe-Bloch functions*. This precision is typically better than 1%. However, even a shift of the nominal Bethe-Bloch position by 0.005 from the center of the curve shown in Fig. 14b can have a sizeable effect on the measured yield.

The sensitivity of $p - \bar{p}$ spectra to both problems depends on reaction type and x_F value. It has been investigated by comparing the results obtained with a wide variety of dE/dx cuts. The selection $(-3\sigma, +0.5\sigma)$ has been judged optimal. The estimated systematic uncertainty of thus obtained net proton spectra is typically 10-15% for p+Pb and 15-20% for $\pi^+ +$Pb reactions.

Corrections. The problem of *vertex losses* is less significant for h+A than for h+p data, due to higher multiplicity. The number of charged particles seen by the NA49 TPC system increases from typically 7 in reconstructed p+p events to 12 for low centrality and 19 for high centrality p+Pb reactions. The overall vertex resolution is better, and the effect of the corrections is much smaller. Thus, even if the appropriate p+Pb correction factors are currently available only in a preliminary form, the systematic error they induce on net proton spectra is estimated to be below 1%. For $\pi^+ +$Pb reactions, where no correction factors are available as yet, the systematic uncertainty is estimated by the total effect of the corrections in the p+Pb case. It is typically 2%.

---

[3]Note: this statement is true for all the results presented in this thesis, but false if applied to tracks with $N < 30$.

The problem of *trigger losses* discussed for inclusive elementary reactions does not apply to centrality-selected h+A events. Here, the event samples are defined by the number of *triggered* grey protons, observed by the NA49 detector. Events lost by the trigger simply do not enter the sample.

The problem of *hyperon feed-down* in h+A interactions is still under investigation. It is more difficult than in h+p collisions due to missing reference data on the centrality dependence of hyperon production. For p+Pb data, a preliminary set of corrections has so far been devised, based on existing knowledge and several assumptions. The systematic uncertainty which this correction induces on $p - \bar{p}$ spectra is tentatively estimated to about 4%. No feed-down correction has as yet been devised for π^++Pb reactions. In the present analysis, an *ad hoc* correction is applied. It is based on the observation that the relative contribution of hyperon decay products to p and $\bar{p}$ yields is similar in p+p and π^++p reactions. A analogous similarity is assumed for p+Pb and π^++Pb collisions. The systematic error induced by this provisional correction is estimated to 7%. Note that both estimates are rough.

Total systematic errors. The summary of systematic error estimates given in Table 3 is obtained in a similar way as for elementary collisions. The errors change little with centrality. The main ingredient in the presented values is the dE/dx cut uncertainty. As the problem of trigger losses does not apply here, the additional normalization errors are negligible.

reaction	$p - \bar{p}$ systematic error		
	$x_F \approx 0$	$x_F \approx 0.2$	$x_F \approx 0.4$
p+Pb	13%	12%	15%
π^++Pb	18%	20%	20-25%

Table 3: Estimates of total systematic errors of net proton dN/dx_F spectra for h+A reactions.

Neutron data. The preliminary neutron spectra for p+p and p+Pb reactions, presented in the following Section have been deconvoluted for the energy resolution of the Ring Hadron Calorimeter. This has been made using a function describing precisely the response of this device[4]. The vertex and trigger loss corrections have not been available at the time the analysis was made. An *ad hoc* correction has been applied to p+p spectra, where the above losses are the most important. As the calorimeter provides no possibility of distinguishing between neutrons and antineutrons, an $\bar{n} = \bar{p}$ assumption has been applied in order to obtain $n - \bar{n}$ distributions. Both n and $\bar{p}$ spectra have been corrected for hyperon feed-down (the method applied has been exactly similar as for net protons). For reasons described in Ch. 1, the analysis has been limited to the region above $x_F = 0.2$. The systematic errors of this preliminary data are still to be investigated. They should be at least comparable to these of $p - \bar{p}$ spectra.

2.2.2 The results: hadron+nucleus collisions

The fact that the two-component picture of net proton spectra appears consistent with the data on several elementary reactions (Sec. 2.1) has an important consequence. It is possible to extract the projectile component of the $p - \bar{p}$ distribution by subtracting the target component, provided an experimental access to the latter is available. This possibility will now be exploited to get an idea of the "projectile baryon number transfer" in nuclear collisions, and to provide a basis for a sound comparison of the baryon stopping effects in centrality-selected p+Pb and Pb+Pb interactions.

Fig. 15a presents the hypothetical behaviour of projectile and target components of the net baryon spectrum in a centrality-selected p+Pb reaction. Due to multiple subcollisions of the projectile with target nucleons, the target component piles up proportionally to ν. The behaviour of the projectile component is *a priori* unknown, but *baryon stopping* is expected. After the projectile has undergone several subcollisions, its contribution to the net baryon spectrum will change shape and get more

---

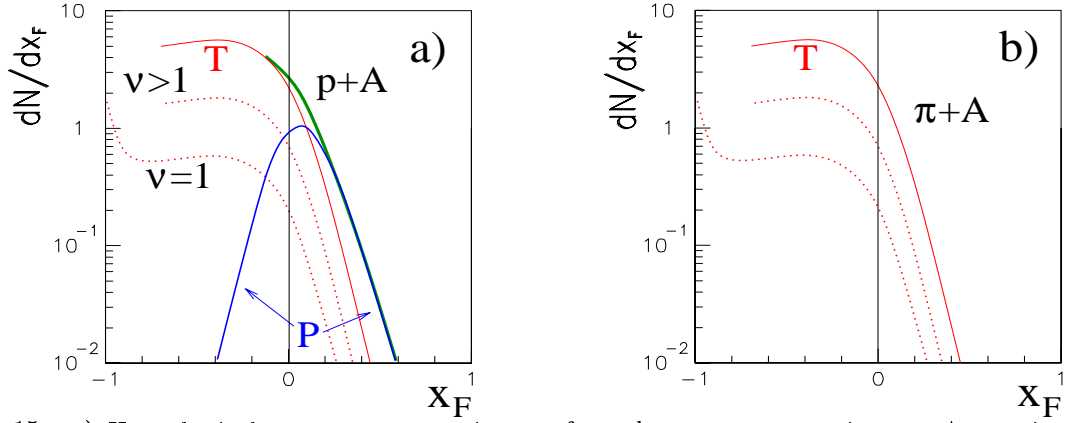[4]The technical aspects of the problem will be described in a Ph.D. thesis in preparation [25].

Figure 15: **a)** Hypothetical two-component picture of net baryon spectrum in a p+A reaction at a given centrality. The total p+A spectrum is a sum of two components: T-target, P-projectile. The T component piles up proportionally to ν, as shown in the plot. **b)** The same for a π+A interaction. The total π+A net baryon spectrum contains only the target component.
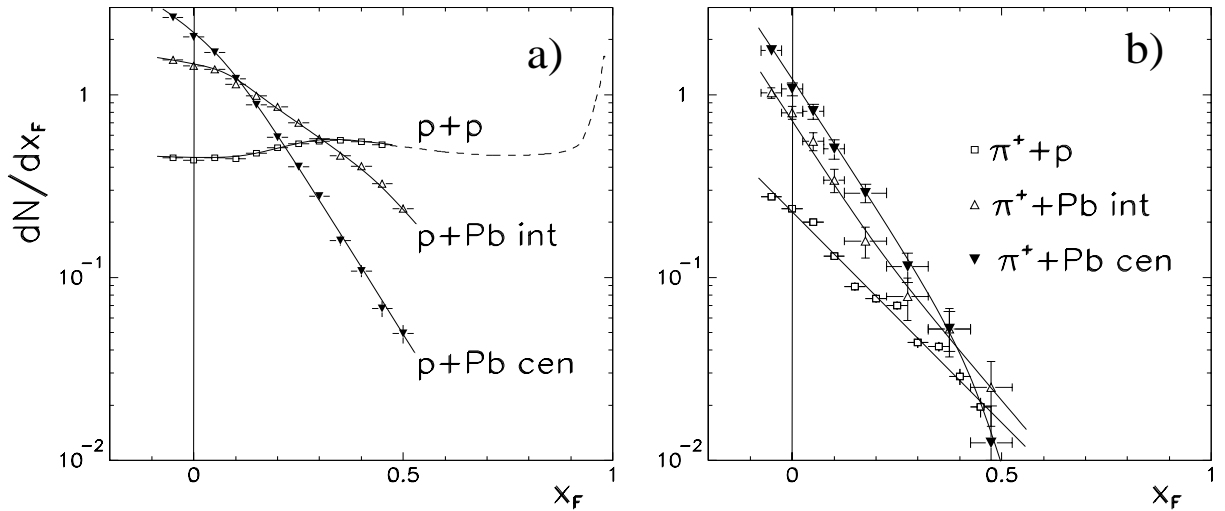

Figure 16: Longitudinal net proton spectra for **a)** p+p, p+Pb, and **b)** π^++p, π^++Pb collisions. The definitions of the "int" (intermediate) and "cen" (central) samples are given in the text.

central. It can be accessed experimentally using π+Pb data to subtract the contribution of the target, shown in Fig. 15b.

The experimental $p - \bar{p}$ spectra for p+p and p+Pb reactions are shown in Fig. 16a. The two centrality-defined p+Pb samples are obtained by requesting a given number of grey protons n_{grey} observed in each selected event. The intermediate sample has been selected by requesting $0 \le n_{grey} \le 3$. This corresponds to $<\nu> \approx 3.1$ elementary subcollisions as given by the VENUS generator (Ch. 1). This average $<\nu>$ value is close to that for minimum bias p+Pb collisions (about 3.7). The central sample has been obtained by requesting $n_{grey} \ge 10$. This corresponds to the highest practically accessible value of $<\nu> \approx 6.3$. As expected from Fig. 15a, a strong steepening of the total $p - \bar{p}$ spectrum with increasing number of elementary subcollisions is apparent.

Fig. 16b shows the corresponding $p - \bar{p}$ spectra for π^++p and π^++Pb collisions. The two π^++Pb centrality samples are obtained by the same n_{grey} selections as applied for p+Pb. The subsequent discussion assumes that this corresponds to the same $<\nu>$ values. Note that this assumption does not have to be fully correct. Its impact on the results will be discussed in Appendix B.

The fast increase of dN/dx_F values with centrality, observed for lower x_F in Fig. 16b, is expected from Fig. 15b as a result of the target pile-up. However, the steepening of the spectra is interesting. It is tempting to say "the projectile is tiring out of pushing target nucleons into the opposite hemisphere". Still, the Figure should be taken with caution: in analogy to what has been said in Sec. 2.1 about π^++p and π^-+p reactions, the π^++Pb spectrum is expected to contain not only a target component, but
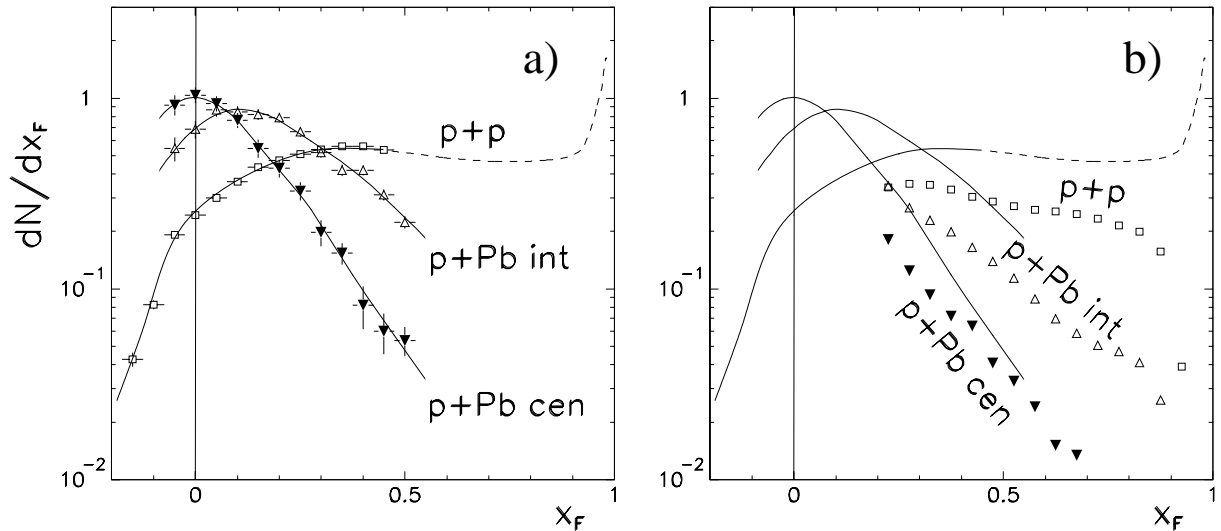
21

Figure 17: **a)** The projectile component of net proton spectra in p+p and centrality-selected p+Pb reactions. **b)** Data points: $n - \bar{n}$ spectra in p+p and p+Pb collisions. Curves: projectile component of $p - \bar{p}$ spectra (shown in panel a).

also a projectile contribution originating from an asymmetric $B\bar{B}$ pair production. Only a "$\pi^{\pm}$+Pb" curve (average between π^{+}+Pb and π^{-}+Pb) would be free from this contribution. The problem is that this curve can not yet be produced due to lack of π^{-}+Pb data. Thus, to what extent this steepening effect indeed concerns the target nucleons is still to be elucidated.

The next step of this study is the extraction of projectile components of net proton spectra in p+p and p+Pb collisions. For p+p interactions, this is done by subtracting the target component (the $\pi^{\pm}$+p curve from Sec. 2.1) from the total p+p spectrum. For p+Pb, the absence of π^{-}+Pb data does not allow an experimental construction of the two corresponding $\pi^{\pm}$+Pb curves. Thus, assumptions have to be made about the π^{+}+Pb projectile component. In this study, this component is assumed to remain *constant* with centrality and identical to that in π^{+}+p collisions. The results do not depend strongly on its exact behaviour (see Appendix B for discussion).

With the above assumption, the two $\pi^{\pm}$+Pb curves can be obtained on the basis of π^{+}+Pb distributions (Fig. 16b), and subtracted from corresponding p+Pb spectra (Fig. 16a). The resulting projectile components of net proton distributions are shown in Fig. 17a (note that for $x_F \leq -0.1$, p+p data points are obtained by reflection of the $\pi^{\pm}$+p spectrum). A dramatic centrality dependence is apparent in the Figure. In p+p interactions the $p - \bar{p}$ distribution is mostly "flattish" and well localised in the forward hemisphere. In central p+Pb collisions, the bulk of it appears concentrated in the vicinity of $x_F = 0$. The presented result suggests a strong "push" of projectile baryon number towards the backward hemisphere, increasing with centrality of the p+Pb reaction.

In order to complete this Section, an additional point has to be clarified. Up to now, the whole baryon number transfer discussion has been based on $p - \bar{p}$ spectra. This implies the assumption that these spectra are representative of the total net baryon distributions - that there is no basic difference between, e.g., proton and neutron behaviour. In view of the strong baryon stopping effect shown above for protons, the problem of validity of this assumption becomes important. It can be investigated with net neutron distributions shown in Fig. 17b. In principle, the presented comparison between $n - \bar{n}$ spectra and the projectile component of $p - \bar{p}$ spectra is not fully relevant - for neutrons, the target component has *not* been subtracted. However, the corresponding effect is expected to be very small above $x_F = 0.3$. As can be seen in the Figure, the above assumption appears valid: the baryon stopping effect is very similar for protons and neutrons.

2.2.3 Comparison to nucleus+nucleus reactions

The above analysis of "projectile baryon number transfer" brings an important benefit in comparisons between p+A and A+A interactions. In an A+A reaction, *each* participating nucleon suffers multiple
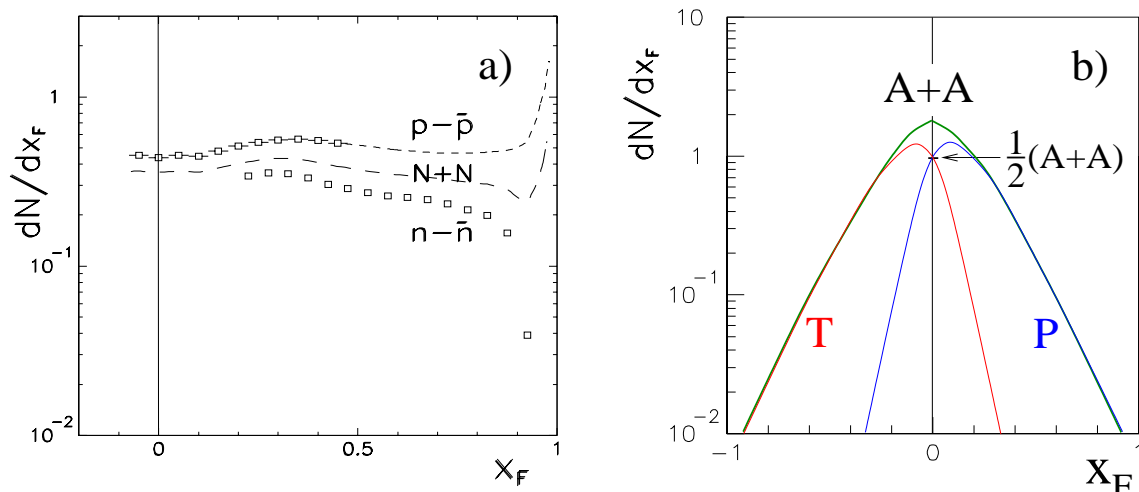
Figure 18: **a)** The N+N net proton spectrum (see text), compared to net proton and net neutron distributions obtained in p+p reactions. **b)** Expected two-component picture of net baryon spectrum in A+A reactions. Note: at $x_F = 0$, the value of both components (T-target, P-projectile) must be equal to $\frac{1}{2}$ of the total A+A value.

subcollisions. In any "classical" study, based on a comparison of net baryon spectra *without* target subtraction, a sizeable part of the effects observed in p+A collisions results from the pile-up of the target component. The contribution of the projectile, suffering multiple subcollisions, is "hidden" in the total spectrum. The interpretation of such an *indirect* comparison is difficult. The study presented in Sec. 2.2.2 provides a way to solve this problem.

The aim of this Section is to perform a more *direct* comparison of p+Pb and Pb+Pb reactions: to compare the behaviour of *projectile components* of net proton spectra. These have already been obtained for p+p and p+Pb reactions. However, a similar analysis has to be performed for Pb+Pb data. This is not possible without answering the following questions:

a) What is the appropriate elementary reference curve for net proton spectra in Pb+Pb reactions? These reactions could be imagined as consisting of p+p, n+p, p+n, and n+n subcollisions. Thus, the $p - \bar{p}$ spectrum originating only from p+p is *not* the correct reference.

b) How to extract the projectile component in Pb+Pb collisions? A logical continuation of the procedure applied in Sec. 2.2.2 would imply the use of a nuclear projectile containing no baryon number (a "pion nucleus"). This does not exist.

Below the following answers are proposed:

Ad a) The appropriate "elementary reaction" to provide a correct reference for Pb+Pb collisions would be a fictitious "N+N" interaction, where the "nucleon" N would reflect the isospin content of the Pb nucleus:

$N = 0.39p + 0.61n$

Assuming the two-component picture of net baryon spectra, the distribution of net protons produced in the N+N collision can be obtained[5] from a weighted sum of p+p net proton and net neutron spectra:

$N + N \rightarrow p = 0.39(p + p \rightarrow p) + 0.61(p + p \rightarrow n)$

Therefore, this distribution can be obtained from experimental data. This is shown in Fig. 18a. Note that below $x_F = 0.2$, the curve drawn in the Figure is only a conjecture.

Ad b) The projectile and target components of the Pb+Pb spectrum cannot be isolated experimentally, but a symmetry constraint can be imposed on them: they must be equal at $x_F = 0$ (Fig. 18b). With this constraint, their shape could be deduced on the basis of π+p and π+Pb interactions: as a first approximation, appropriately scaled π+Pb curves could be used to subtract the target component.

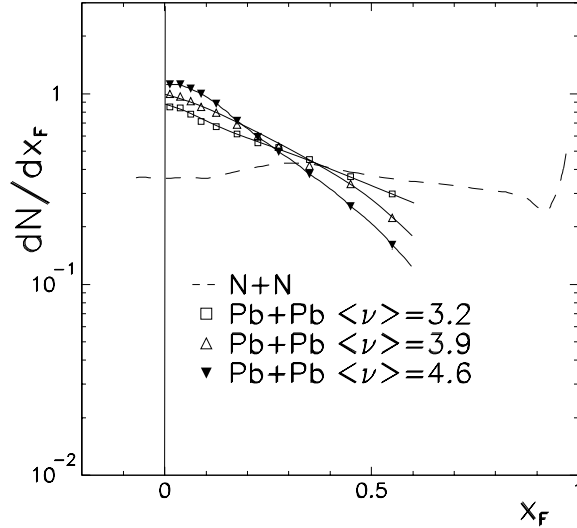[5]A demonstration can be found in Appendix B.

Figure 19: Net proton spectra in three centrality-selected Pb+Pb samples, together with the N+N reference curve. Note: the Pb+Pb spectra are scaled down by the number of participant pairs as described in the text.
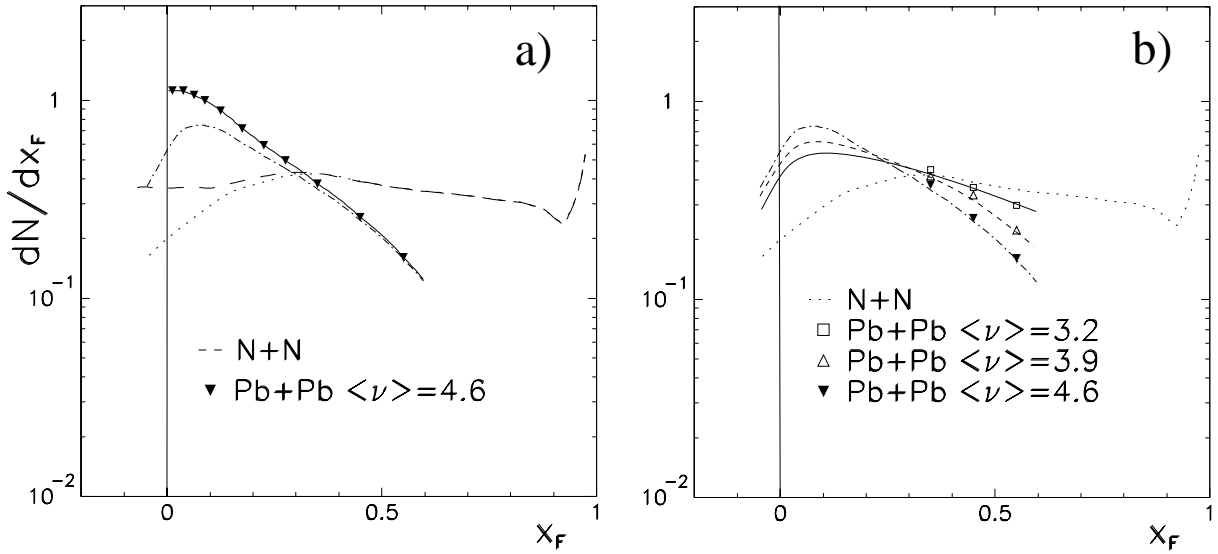

Figure 20: **a)** Target subtraction for the central Pb+Pb net proton spectrum and for the N+N curve. Solid, dashed: respective total $p - \bar{p}$ spectra, dash-dot, dotted: projectile components. **b)** The projectile component of net proton spectra in Pb+Pb reactions.

The answers **a)** and **b)** constitute the basis of the study presented below. In all this study, the presented Pb+Pb spectra are scaled down by the number of *participant pairs*, i.e. half the number of participants defined for a given centrality sample (Ch. 1). Thus they are directly comparable to N+N collisions.

Fig. 19 shows $p-\bar{p}$ distributions for three centrality-selected Pb+Pb samples and the N+N reference curve. The Pb+Pb samples are defined by $<\nu>$ values obtained from VENUS (Ch. 1). Note that $<\nu>\approx 4.6$ is the highest Pb+Pb centrality which is practically accessible. The subtraction of the target component is demonstrated in Fig. 20a. For all Pb+Pb distributions, the shape of the intermediate $\pi^{\pm}$+Pb spectrum is assumed for the target component. For the N+N curve, the projectile component is deduced on the basis of net proton spectra in p+p collisions. The result of the whole operation is shown in Fig. 20b.

The overall picture of projectile baryon number transfer in Pb+Pb collisions presented in Fig. 20b can be compared to that shown for p+Pb reactions (Fig. 17a). The two pictures are similar. With increasing centrality, the "flattish" elementary distribution steepens and gets "pushed" towards $x_F = 0$. A direct comparison of the two sets of curves is not straightforward, due to differences between the
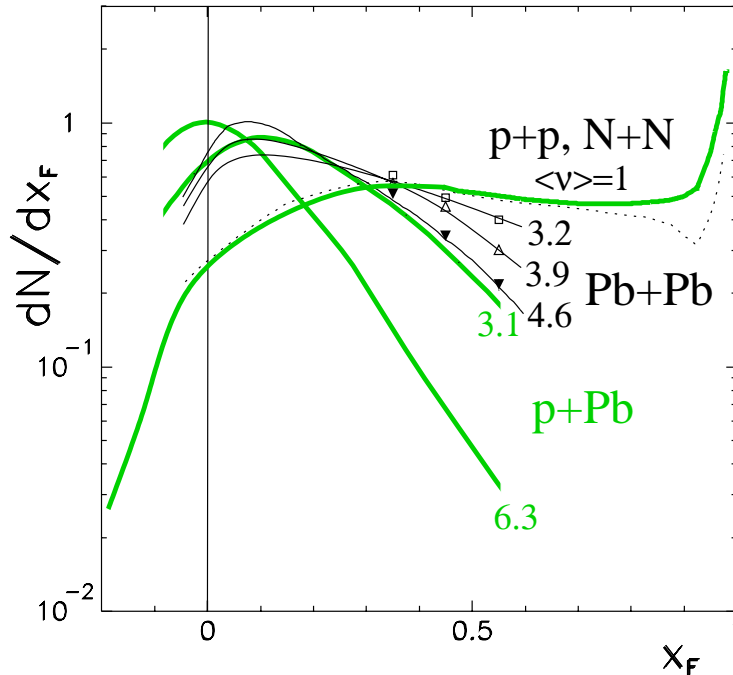
24

Figure 21: Comparison of projectile baryon number transfer in p+Pb and Pb+Pb reactions. The p+p/p+Pb results from Fig. 17a are represented by shaded curves. The N+N/Pb+Pb spectra from Fig. 20b (dotted, solid) are scaled up by 1.35. The $<\nu>$ values corresponding to the presented data samples are given in the plot.

reference p+p and N+N curves. An attempt for such a comparison is proposed in Fig. 21, where the N+N curve is arbitrarily scaled up by 1.35 to match the p+p curve "as well as possible". The same scaling factor is applied on Pb+Pb distributions.

The result of this comparison is clear. A *common picture of baryon number transfer* in p+p, p+Pb and Pb+Pb reactions emerges from the Figure. For both p+Pb and Pb+Pb interactions, baryon stopping smoothly increases with centrality. Central Pb+Pb collisions occupy a *medium position* between p+p and central p+Pb reactions.

This common picture naturally suggests a common or similar baryon stopping mechanism. The medium position of central Pb+Pb relative to p+p and central p+Pb could be at least partially understood from simple geometric considerations. If taken as superposition of nucleon+Pb reactions, a central Pb+Pb collision would be composed of both central and peripheral collisions. Thus, less stopping than in central p+Pb would be expected.

However, let us comment on the fact that the two sets of curves (p+Pb, Pb+Pb) do not show a unique dependence on $<\nu>$. It would seem that at the same $<\nu>$ value, more stopping is observed in p+Pb collisions. This is interesting but should be taken with caution. As has been said in Ch. 1, the VENUS values for $<\nu>$ in p+Pb and Pb+Pb reactions come from wide distributions. To what extent baryon stopping studies can rely uniquely on the first moments of these distributions is to be elucidated. What is more, the experimental access to centrality in p+Pb and Pb+Pb collisions is completely different. To what extent the VENUS model can be used to extract absolute ν values on this basis is unclear. Second-order p+Pb/Pb+Pb differences in the uniform picture presented above are certainly possible. However, the experimental evidence is not fully convincing yet.

The last question to be discussed is that of several *assumptions* made in this study. It is useful to know how much the above uniform picture depends on them. A study of this problem can be found in Appendix B. Here let us only state that the estimated sensitivity of our results is not large enough to cause a sizeable modification of this picture.

2.3   Summary and outlook

The two-component picture of net proton spectra has appeared consistent with presented data on elementary p+p and π+p collisions. It has been also applied to nuclear reactions. This has resulted in

a uniform picture of baryon number transfer in p+p, p+Pb, and Pb+Pb interactions. The projectile component of p+Pb net baryon spectra shows a strong dependence on centrality, indicating a "push" of the projectile baryon number towards the backward hemisphere. A very similar behaviour is observed for Pb+Pb collisions. In the magnitude of the common baryon stopping effect, central Pb+Pb reactions occupy a medium position between p+p and central p+Pb collisions. No basic difference in the behaviour of various final state baryons (protons, neutrons) is observed outside the diffractive region. Additional phenomena, like the steepening of net proton spectra in π^++Pb collisions, remain to be explored with a more complete dataset.

A similar behaviour of net proton spectra in the three collision types naturally suggests a similar mechanism for baryon number transfer. On the other hand, the bulk of baryon number transfer takes place *already in p+p collisions*, where the outcoming net proton has "lost" some 50% of the projectile longitudinal momentum and has a very broad x_F distribution (Fig. 21). This inspires questions. Isn't it possible that also other phenomena seen in proton+nucleus and nucleus+nucleus reactions originate from a common or similar mechanism, present already in proton+proton? Isn't it therefore possible to select some "subgroups" of p+p events which would reproduce what is being observed for p+A and A+A interactions? Couldn't the process of baryon number transfer be an onset of such a common mechanism, intimately related to other observables? These questions will constitute the starting point of the following Chapter.

It is worthwhile to add that the study of projectile components presented above is to a certain extent similar to that made by Busza and Goldhaber [26]. Although without experimental centrality control, the above authors have produced an extrapolation of centrality dependence of projectile baryon rapidity loss in a Pb target. It will be very interesting to compare this extrapolation to results presented here, obtained directly from experimental data.

Chapter 3. Charged Pion Production

This Chapter contains a study of charged pion production in p+p, p+Pb and Pb+Pb reactions. A semi-inclusive analysis of p+p events is made in order to investigate the dependence of pion behaviour on the longitudinal momentum of the final state proton. On this basis, expectations for nuclear collisions are formulated. These expectations are then verified by an analysis of centrality-selected p+Pb and Pb+Pb interactions. Conclusions are drawn.

The study contains comparisons of systems with different isospin content. This is why the analysis is limited to summed charged pions ($\pi^+ + \pi^-$). It concentrates on three main aspects: the forward hemisphere multiplicities, the longitudinal distributions, and the transverse momentum behaviour. Apart from results obtained within this thesis' framework (all presented p+p and p+Pb data), this Chapter additionally contains the results of an independent study of Pb+Pb reactions [19].

First, the motivation underlying this analysis is explained and the main details of the study are briefly discussed. Then, the experimental data analysis methods are presented. Finally, the results of the analysis are shown and discussed.
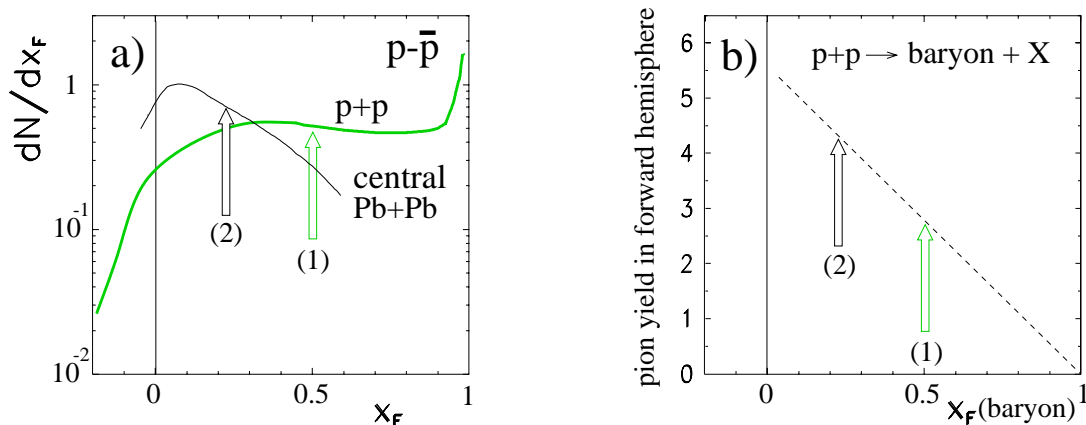
3.1 Motivation

Figure 22: Baryon number transfer in p+p and central Pb+Pb collisions, in relation to pion multiplicity. **a)** Projectile component of net proton spectra in both reactions. Curves come from Fig. 21. Arrows give rough estimates of averages of the p+p (1) and Pb+Pb (2) distributions. **b)** Hypothetical correlation between pion multiplicity and outcoming baryon x_F. Averages from panel a) are marked in the plot.

This analysis is inspired by a basic question formulated in Ch. 1: is the nuclear collision behaviour a direct consequence of what is observed already in elementary processes, or are "new", non-elementary phenomena taking place e.g. in A+A reactions? The smooth baryon stopping evolution in p+p, p+Pb and Pb+Pb collisions (Ch. 2) suggests similar baryon number transfer mechanisms in the three reaction types. For that reason, it gives a hope to shed some light on the problem. Let us demonstrate it on the example of pion multiplicities observed in p+p and A+A interactions.

It is known that at our energies, an enhancement of pion production (total yield per participant nucleon) is observed e.g. in central Pb+Pb relative to inclusive inelastic p+p collisions [19]. As we know from Ch. 2, these two reactions strongly differ by the degree of baryon number transfer (Fig. 22a). In p+p collisions, the average x_F of the outcoming proton is about 0.5. For central Pb+Pb, the corresponding value must be significantly lower (very roughly 0.2).

Let us now consider a possible dependence between the forward hemisphere pion multiplicity and the x_F of the outcoming baryon. This is illustrated in Fig. 22b. The forward hemisphere pion yield will be equal to zero for $x_F(baryon) = 1$. With decreasing baryon x_F, we pass from the diffractive to the non-diffractive region, so average multiplicity increases. Thus, the simplest assumption of a linear

correlation can be made as shown in the Figure. Such a correlation might also be suggested by simple considerations based on energy-momentum conservation.

Assuming the above correlation, a prediction can be formulated for pion yields observed in central Pb+Pb reactions. Due to a shift of average baryon x_F towards lower values, an increase of pion multiplicity relative to inclusive p+p interactions would be expected (Fig. 22b). Thus, the increase observed experimentally would not necessarily require any "new" mechanism of pion production in A+A. It could be nothing but a consequence of effects present *already in elementary events* (of the correlation between baryon x_F and pion multiplicity), and of a different average degree of baryon stopping, resulting from a larger "thickness" of the nuclear target.

Thus, the analysis of correlations between the outcoming baryon x_F and other observables in p+p events provides a way to formulate predictions about the nuclear collision behaviour. Phenomena following such predictions can be considered as *expected* on the basis of p+p events, and thus also *unexpected* phenomena can be isolated. Therefore, this type of study can provide more insight into the problem than a simple comparison between Pb+Pb and inclusive p+p collisions.

The study made in this Chapter follows the general idea described above. It is focussed on three principal points:

1. What is the internal correlation structure of p+p events? What is the exact relation between pion production and baryon number transfer from the projectile to the final state baryon?

2. What are the resulting expectations for nuclear reactions?

3. Does pion production in p+Pb and Pb+Pb collisions follow these expectations?

The analysis relies on three observables: **a)** the charged pion multiplicity in the projectile hemisphere, averaged over a given event sample ($<\pi>=<\pi^+>+<\pi^->$), **b)** the dN/dx_F distribution of charged pions, and **c)** the x_F dependence of charged pion mean transverse momentum (that is, pion $<p_T>$ vs. pion x_F). To simplify the subsequent discussion, these three observables are presented below, for the case of inclusive (minimum bias) inelastic p+p collisions. The corresponding $<\pi>$ value obtained in this analysis is 2.60 ± 0.21(syst). Its statistical error is negligible. The two distributions (dN/dx_F, $<p_T>$ vs. x_F) are shown in Fig. 23. Note the steepness of the pion dN/dx_F spectrum, which extends over two orders of magnitude in the x_F range of 0 to 0.4, and the well-known "sea-gull" shape of the pion $<p_T>$ vs. x_F dependence [4]. In the first part of the study (item 1), the above observables are analysed as function of x_F of the fastest (leading) proton found in the p+p event. In the subsequent parts (items 2-3), their centrality dependence in p+Pb and Pb+Pb reactions is considered.
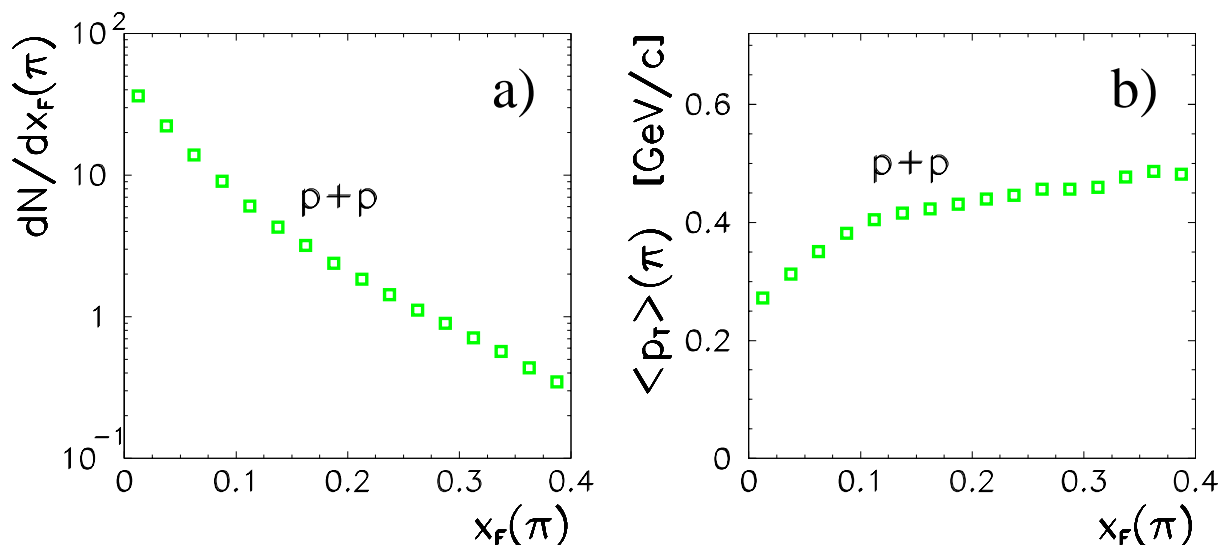

Figure 23: **a)** the dN/dx_F spectrum, and **b)** the $<p_T>$ vs. x_F dependence, obtained for charged pions ($\pi^+ + \pi^-$) in minimum bias p+p collisions. Note: statistical errors are smaller than the symbol size.
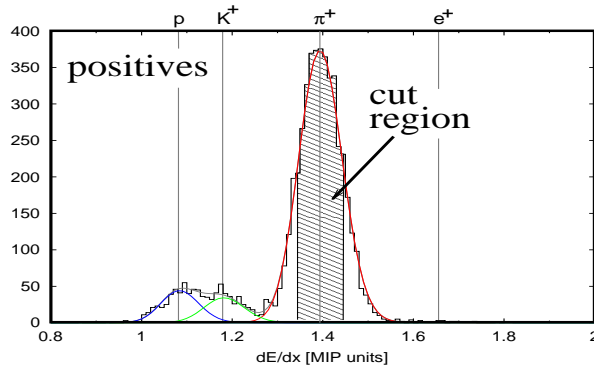
Figure 24: Simplified illustration of the dE/dx cut method. The contributions of different particles to the truncated mean dE/dx spectrum, and the positions of the four Bethe-Bloch functions, are also shown in the plot.

3.2 Data analysis

This Section focuses on methods applied to study pion production in p+p and p+Pb reactions. The Pb+Pb analysis is described in [19], where a preliminary estimate of its systematic errors is given. For the clarity of the discussion, this presentation of data analysis methods reverts the actual order in which the experimental results are shown in the following Sections. First, the relatively simpler studies of inclusive p+p and centrality-selected p+Pb interactions are discussed. Then, the more complicated analysis of the internal correlation structure of p+p events is explained.

3.2.1 Inclusive p+p and centrality-selected p+Pb data

The experimental methods applied in this part of the study are essentially the same as those described in Ch. 2. The centrality selection of p+Pb samples is made by requiring a given number of grey protons (n_{grey}) registered by the NA49 detection system. Forward hemisphere pion multiplicities $<\pi>$, pion dN/dx_F spectra and $<p_T>$ vs. x_F dependencies are obtained on the basis of highly enriched π^+ and π^- samples, identified by dE/dx cuts in the NA49 TPC system. The results are corrected for trigger and vertex losses, as well as for feed-down from weakly decaying particles.

dE/dx cuts. Both the π^+ and π^- samples are obtained by applying a symmetric $(-1\sigma, +1\sigma)$ cut around the pion Bethe-Bloch value on the truncated mean dE/dx spectrum. This is schematically illustrated in Fig. 24. Just as for net proton spectra in the previous Chapter, the number of thus selected "pion candidates" is multiplied up to compensate for pions remaining outside the cut.

The analysis is restricted to an azimuthal wedge of $|\phi| < 50°$ for π^+, and an identical wedge around $\phi = 180°$ for π^-. This insures a 100% acceptance with minimum 30 points on TPC track in the investigated pion x_F range. The obtained forward pion yields and longitudinal spectra are corrected for azimuthal cuts. Then, they are normalized to the number of events in the given data sample; the longitudinal spectra are additionally divided by the x_F bin width.

Just as for $p - \bar{p}$ spectra, the principal systematic error sources of this method are the contamination from other particles (electrons, kaons and protons), and the limited precision of adjustment of Bethe-Bloch functions. The sensitivity of the results to both problems has been estimated by applying a wide variety of dE/dx cuts. The resulting systematic error depends on pion x_F. It is about 6% for $<\pi>$ values. It is also 6% for dN/dx_F spectra below $x_F = 0.25$, and goes up to 15-20% at $x_F = 0.4$. It is typically 10-16 MeV/c for $<p_T>$ values. For the single case of the most central p+Pb sample (selected by requiring $10 \leq n_{grey} \leq 25$), the latter uncertainty can reach about 40 MeV/c at higher x_F.

Corrections. The same set of *vertex loss* correction factors that has been used for net proton spectra in Ch. 2 is also applied in this analysis. The induced systematic error depends on reaction type, centrality and pion x_F. For forward hemisphere multiplicities, it remains below 2%, with the exception of the very peripheral p+Pb sample, selected by an $n_{grey} = 0$ cut (no grey protons seen). For this very small sample[1], the correction procedure is less reliable and an 8% systematic error is

---

[1]Note: this specific sample contains ca. 9,000 events. All other p+Pb samples contain at least 50,000 events.

estimated. This is due to a sizeable contamination of background events, originating in the walls and gas of the Centrality Detector. Both estimates given above include a small (below 1%) normalisation uncertainty.

The systematic error induced by the vertex loss correction on pion dN/dx_F spectra remains below 2% (including normalisation uncertainties). It is below 2 MeV/c for $<p_T>$ values. Note that the $n_{grey}=0$ sample is not used for dN/dx_F and $<p_T>$ studies.

As has been said in Ch. 2, all the inclusive p+p results are subject to *trigger losses* which need to be corrected for. The correction results in an additional normalisation uncertainty of forward hemisphere multiplicities and dN/dx_F spectra. This uncertainty is estimated to 4-5%. As has been said, this problem does not apply to centrality-selected p+Pb reactions.

The last effect to be corrected for is that of *feed-down of weakly decaying particles*. These particles are the hyperons discussed in Ch. 2 ($\Lambda/\bar{\Lambda}$ and $\Sigma/\bar{\Sigma}$), and additionally the K_s^0. The products of their decays contaminate the experimentally selected pion samples. This contamination is relatively small (below 3%). The correction is made using the same Monte-Carlo method that has been applied in Ch. 2. The decay modes taken into account are $\Lambda^0 \to p\pi^-$, $\bar{\Lambda}^0 \to \bar{p}\pi^+$, $\Sigma^+ \to n\pi^+$, $\bar{\Sigma}^- \to \bar{n}\pi^-$, and $K_s^0 \to \pi^+\pi^-$. The systematic error induced by this correction depends on the accuracy to which hyperon and K_s^0 cross-sections and distributions are known in p+p and p+Pb reactions. According to rough estimates, it is below 1% for $<\pi>$ values and dN/dx_F spectra. Note that this correction is not applied in the transverse dimension - this would require further development of the Monte-Carlo method. The resulting $<p_T>$ uncertainty is small, mostly due to the small overall size of the effect. A rough estimate gives an upper limit between 2 and 5 MeV/c, depending on x_F.

Total systematic errors. The estimates of total systematic errors are given in Tables 4 and 5. They are obtained by adding in quadrature all error sources for all data samples included in the analysis. Note that the error may vary with the x_F of the pion - in Table 5 a few representative values are listed. The normalisation errors are included in the values given in Table 4, but listed separately in Table 5. The main ingredient in the presented values is usually the uncertainty of the dE/dx cut method.

reaction	centrality sample (n_{grey} selection)	error on $<\pi>$ [%]
p+p	-	8
p+Pb	$n_{grey}=0$	10
p+Pb	$n_{grey}=1$, $n_{grey}=3$, $0 \leq n_{grey} \leq 3$, $10 \leq n_{grey} \leq 25$	6

Table 4: Estimates of total systematic errors of forward hemisphere pion multiplicities.

reaction, centrality sample	error on dN/dx_F [%]			normalisation error [%]	error on $<p_T>$ [MeV/c]		
	$x_F \approx 0.05$	$x_F \approx 0.2$	$x_F \approx 0.35$		$x_F \approx 0.05$	$x_F \approx 0.2$	$x_F \approx 0.35$
p+p	6	6	15	5	12	12	12
p+Pb, $10 \leq n_{grey} \leq 25$	6	6	15	0.3	17	18	40
p+Pb, other samples	6	6	15	0.3-1	17	17	17

Table 5: Estimates of total systematic errors of pion dN/dx_F spectra and $<p_T>$ values. Note: the Table does not contain the most peripheral p+Pb sample ($n_{grey}=0$), which is not used for dN/dx_F and $<p_T>$ analysis.

3.2.2 Data analysis in correlation studies

The aim of this part of the analysis is to investigate the internal correlation structure of p+p events, that is, the relation between pion production and the transfer of baryon number from the projectile to the final state baryon. The study is limited to final state protons[2].

Schematically, the experimental method is shown in Fig. 25a. From the total minimum bias p+p sample, events with a proton in the forward hemisphere are selected. For these events, forward

---

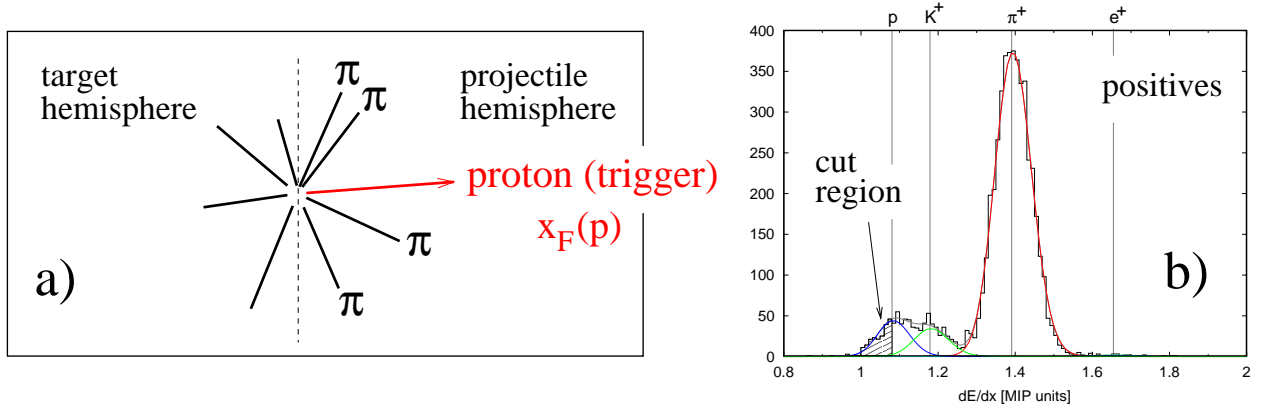[2]Its extension to final state neutrons could be considered.

Figure 25: **a)** General scheme of analysis of correlations in p+p events. **b)** Trigger proton identification.

hemisphere pion production is studied as function of the x_F of this "trigger" proton: $x_F(p)$. Note that this type of analysis goes a step further relative to inclusive or even centrality-dependent studies. It investigates the internal kinematic relations between various particles in the event.

On the practical side, this study encounters several difficulties. First, the analysis method has to insure that the selected proton indeed reflects baryon number transfer from the *projectile*. The proton must belong to the *projectile component* of the net proton spectrum (Ch. 2). Protons produced in $B\bar{B}$ pairs, and these belonging to the target component, have to be removed from the data sample. The second difficulty is the following: contrary to inclusive p+p studies, this analysis cannot be restricted to any wedge in azimuthal angle ϕ. Possible azimuthal correlations between the outcoming proton and the produced pions would bias the results of the study. Therefore, the analysis has to be made in *full* azimuthal angle, and *acceptance losses* cannot be avoided. On top of these new difficulties, various experimental problems discussed in Sec. 3.2.1 have also to be taken into account. Finally, fixing the momentum of the final state proton reduces the event sample by 1-2 orders of magnitude (Table 1, Ch. 1). This has immediate consequences for the necessary event sample size.

Various aspects of the analysis are discussed below. Note that the discussion is based on the description of NA49 acceptance and identification possibilities, which has been part of Ch. 1.

Selection of the leading proton. The projectile hemisphere proton from Fig. 25a is identified by means of a $(-3\sigma, +0)$ cut applied on the truncated mean dE/dx spectrum (see Fig. 25b). This differs from the $(-3\sigma, +0.5\sigma)$ cut applied in net proton spectra studies, due to the need of minimizing kaon contamination. The analysis is made in full azimuthal angle. It is restricted to particles with at least 30 points on TPC track.

The trigger proton identified by the above method can be pair produced, belong to the target component, or finally belong to the projectile component of the net proton spectrum. However, if the selected proton does *not* belong to the projectile component, then another faster baryon is likely to be also present in the forward hemisphere of the p+p event. Therefore, the following additional selection is made:

- if more than one proton is identified via dE/dx, then the fastest is selected.
- if in the event, a faster neutron or a faster proton is observed in the Ring Hadron Calorimeter, the event is removed from the sample.

Protons which survive the above selection will be referred to as *leading protons*. This selection method is obviously not ideal, especially close to $x_F(p) = 0$. The contamination of the final leading proton sample by wrongly tagged protons will be negligible for $x_F(p) > 0.3$ (both $B\bar{B}$ pair production and the target component vanish close to $x_F(p) = 0.3$). However, it is expected to increase with decreasing $x_F(p)$. Very rough, preliminary estimates give a contamination of the order of 15% at $x_F(p) = 0.1$. For that reason, only leading protons above this $x_F(p)$ value are used in this study. Due to TPC acceptance losses, the study stops at $x_F(p) = 0.6$.

Pion identification. The π^+ and π^- samples are obtained by means of the same dE/dx cut that has been applied in Sec. 3.2.1, i.e. $(-1\sigma, +1\sigma)$ around the pion Bethe-Bloch value. The analysis is

made in full azimuthal angle, and restricted to particles with at least 30 points on TPC track. The uncertainties of this method have been estimated in the same way as for inclusive studies. The resulting systematic error is about 6% for $<\pi>$ values. It is 6% for pion dN/dx_F spectra below $x_F = 0.25$, and goes up to 15-20% at $x_F = 0.4$. It is between 12 and 20 MeV/c for $<p_T>$ values.

Acceptance losses. In the present study, the problem of TPC acceptance losses is untrivial. These losses may depend on correlations between produced pions and the trigger proton. In principle, this difficulty could be cured by very detailed and extensive Monte-Carlo studies. In absence of such studies, this analysis relies on rough estimates of acceptance losses and of the induced systematic error. This approach is reasonably secure, because the NA49 TPC system has high full-azimuth acceptance in the lower p_T region were most of the pions are found (Ch. 1).

A first-order estimate of acceptance losses has been deduced on the basis of minimum bias p+p collisions. These have been analysed in two ways: **1)** in full azimuthal angle, and **2)** applying the ϕ restriction from Sec. 3.2.1 and correcting for azimuthal cuts. The results have been compared. The resulting acceptance loss estimate is about 8% for forward hemisphere pion multiplicities. For pion dN/dx_F values, it is about 15% at $x_F \approx 0$, but does not exceed 7% for $x_F > 0.05$. The corresponding shift of pion $<p_T>$ values is typically 10-20 MeV/c.

On the basis of the above study, a multiplicative acceptance correction is applied on $<\pi>$ values, which are scaled up by 8%. Note that this is an *ad hoc* correction, which neglects possible correlation effects. For that reason, the corresponding systematic error is assumed to be also 8%. No correction is applied on pion dN/dx_F and $<p_T>$ values. Note that the dN/dx_F data points in Fig. 23a would move very little, if shifted by the minimum bias estimates given above. The corresponding dN/dx_F systematic errors are assumed equal to the above estimates. Similarly, a systematic error of 10-20 MeV/c is assumed for $<p_T>$ values.

Other problems. A *vertex loss correction* in proton-triggered events would require a complicated study, following the changes of vertex finding efficiency and resolution as function of $x_F(p)$ and charged particle multiplicity. Such a correction should be small: the vertex finding performance would be strongly improved by requiring a proton (a well-defined charged track) in the TPC system. According to rough estimates, the systematic error resulting from the absence of this correction is negligible.

Just as for centrality-triggered p+Pb data (Ch. 2), the problem of *trigger losses* does not apply to proton-triggered p+p events.

No correction is available for *feed-down from weakly decaying particles*. This is caused by the lack of knowledge about the dependence of hyperon and K_s^0 production on leading proton x_F. For the present study, the resulting systematic error is estimated to twice the size of the corresponding correction in inclusive p+p analysis. This gives 4% for forward pion multiplicities, 2-6% for dN/dx_F spectra, and 4-10 MeV/c for $<p_T>$ values.

Total systematic errors. Rough overall estimates of systematic errors are given in Table 6. They are obtained by adding in quadrature all error sources discussed above. Errors may vary with the x_F of the pion, therefore representative values are listed in the Table. Normalisation errors are negligible. The main ingredient in the values below are the acceptance losses and the dE/dx uncertainty.

Note that the estimates given below neglect more subtle sources of systematic error, like e.g. remnant contamination of the leading proton sample by pair produced protons.

The results of the data analysis will be presented in the following Section.

error on $<\pi>$[%]	error on dN/dx_F [%]			error on $<p_T>$ [MeV/c]		
	$x_F \approx 0.05$	$x_F \approx 0.2$	$x_F \approx 0.35$	$x_F \approx 0.05$	$x_F \approx 0.2$	$x_F \approx 0.35$
11	12	9	15	20	20	23

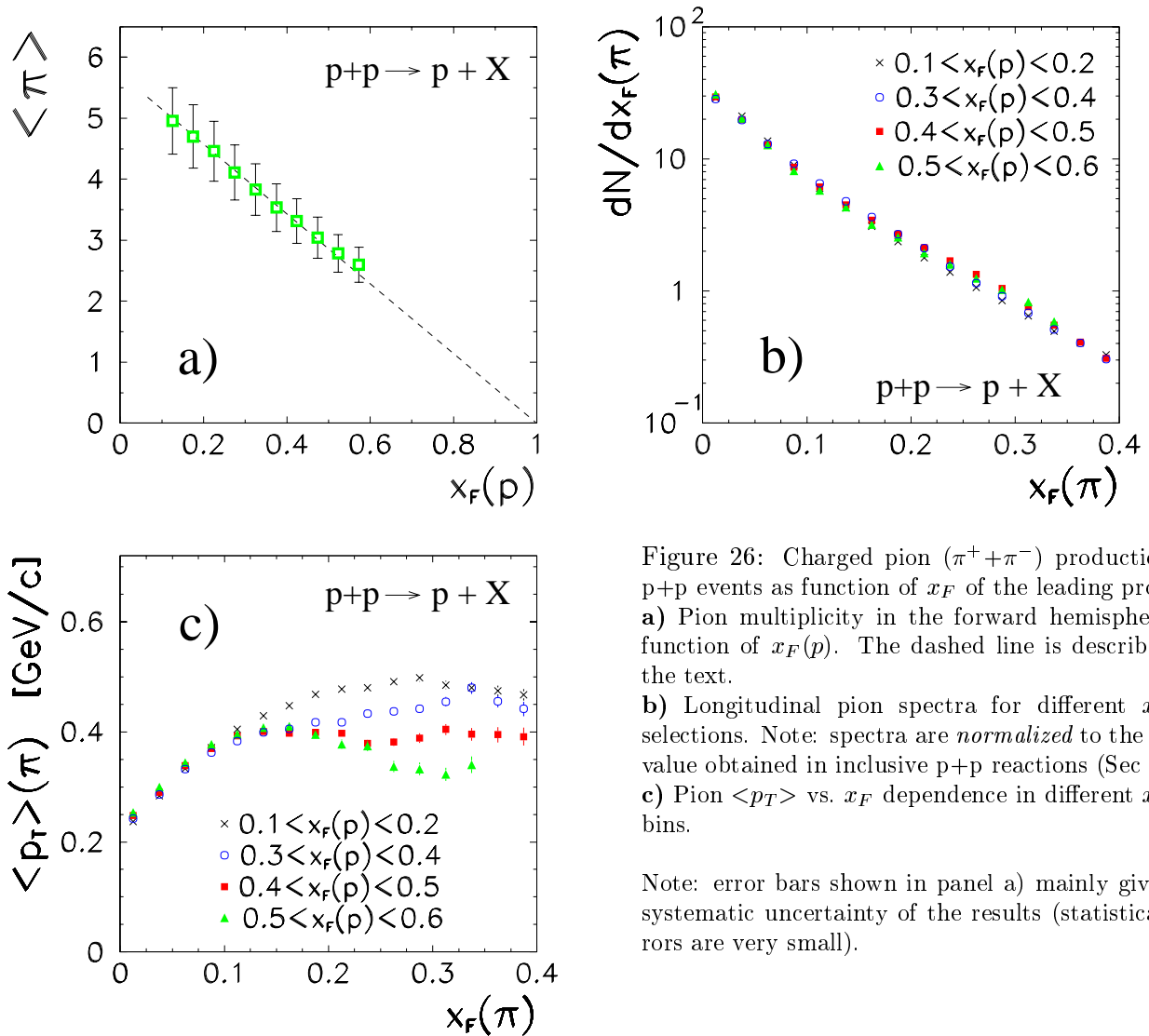Table 6: Estimates of total systematic errors in the correlation analysis.

Figure 26: Charged pion $(\pi^+ + \pi^-)$ production in p+p events as function of x_F of the leading proton. **a)** Pion multiplicity in the forward hemisphere as function of $x_F(p)$. The dashed line is described in the text. **b)** Longitudinal pion spectra for different $x_F(p)$ selections. Note: spectra are *normalized* to the $<\pi>$ value obtained in inclusive p+p reactions (Sec 3.1). **c)** Pion $<p_T>$ vs. x_F dependence in different $x_F(p)$ bins.

Note: error bars shown in panel a) mainly give the systematic uncertainty of the results (statistical errors are very small).

3.3 Internal correlation structure of p+p events

Our discussion starts with the internal structure of p+p events, i.e. the relation between charged pion production and baryon number transfer from the projectile to the final state proton. The baryon number transfer is characterized by the x_F of the leading proton. The experimental results are shown in Fig. 26. The forward hemisphere pion multiplicity shown in panel **a)** depends very strongly on $x_F(p)$. The data indicate a smooth change by roughly a factor of two in the experimentally accessible $x_F(p)$ range. Note that within this range, the data confirm the simple conjecture made in Sec. 3.1. This is illustrated by the dashed line[3].

The pion dN/dx_F distributions are presented in panel **b)**. Note that the distributions are normalized. Only data points satisfying the approximate condition $x_F(\pi) + x_F(p) < 0.9$ are shown in the plot. This is done in order not to include the (trivial) damping of the pion spectrum, occuring at the limit of the available phase-space.

A surprisingly uniform behaviour emerges from the data. Within two orders of magnitude, the four distributions stay very close. While the number of produced pions changes strongly with $x_F(p)$, the *shape* of the pion spectrum remains to first order independent of leading proton momentum.

The transverse momentum behaviour is shown in panel **c)**. The same $x_F(\pi) + x_F(p) < 0.9$ restriction is applied. Again, a definite pattern emerges from the data. Above $x_F(\pi) \approx 0.1$, the pion $<p_T>$ taken at fixed $x_F(\pi)$ values increases with decreasing x_F of the leading proton.

---

[3]A similar result has been obtained for forward associated charged multiplicities at 19 GeV/c [27].

The study presented above confirms the hypothesis formulated in Sec. 3.1. The baryon number transfer from the projectile to the final state proton appears a "significant variable" as far as pion production is concerned. Definite patterns emerge for pion multiplicities, longitudinal spectra and transverse momenta. As elementary and nuclear collisions differ strongly by the degree of baryon stopping, these patterns may serve as a basis for predictions of phenomena occuring in p+A and A+A reactions. Thus, the question of possible consequences which internal features of p+p events may have for nuclear interactions is now experimentally motivated, and will be discussed in the following Section.

3.4   Expectations for nuclear reactions

This Section uses the p+p results presented above as a basis for a prediction of pion behaviour in p+A and A+A reactions.

As a first point, let us summarize that up to a good accuracy, the data on elementary p+p collisions indicate the following trends:

1) $<\pi>$ smoothly increases with decreasing $x_F(p)$.

2) the shape of the pion dN/dx_F spectrum is independent of $x_F(p)$.

3) at least for $x_F(\pi) > 0.1$, the pion $<p_T>$ increases with decreasing $x_F(p)$.

As a second point, let us consider how the presence of several projectile and target nucleons in p+A and A+A reactions may affect such observables as forward pion multiplicities or dN/dx_F spectra. Let us follow an approach inspired by the concept of "wounded" nucleons [28]. Similarly to the quoted reference, let us assume that p+A and A+A reactions can be described in terms of the number of "wounded" nucleons, which have undergone at least one inelastic subcollision. Independently of collision type and centrality, the contribution of each wounded nucleon to the average multiplicity is assumed always equal to half the mean multiplicity in inelastic nucleon+nucleon reactions.

In order to formulate our predictions, this approach has to be extended first to inclusive spectra, and then to the internal correlations observed in p+p events. This can be done in the way proposed in Fig. 27a. The Figure shows the pion dN/dx_F spectrum in inclusive inelastic p+p collisions as a sum of two wounded nucleon contributions, labeled T (target) and P (projectile). We expect that in the forward and backward region, the inclusive pion spectrum will be dominated respectively by its projectile and target contribution.

Now the internal correlation structure of p+p events has to be taken into account. Let us connect the projectile baryon number transfer with the behaviour of the P contribution. Outside of the very low $x_F(\pi)$ region, the behaviour of the P curve is directly constrained by items 1) and 2) given above. It must go up if the leading proton is becoming more central ($x_F(p)$ decreases), and its shape must remain invariant, as indicated by the dashed curve. Let us assume that the *entire* P curve follows this scaling behaviour[4]. Additionally, item 3) indicates that with decreasing $x_F(p)$, pion $<p_T>$ values in the P contribution increase. We assume that all the above behaviour is not exclusive to leading *protons*, but valid for any leading baryon.

Let us generalize this picture to nuclear reactions. Our basic assumption will be that pion production per wounded nucleon is not modified by the fact that the reaction is nuclear and not elementary. The *only* factor which can modify the contribution of each wounded nucleon to the total pion spectrum is the x_F of the corresponding final state baryon. The dependence on baryon x_F is identically the same as for p+p collisions.

Under this assumption, the generalization to A+A collisions is fairly straightforward. This is illustrated in Fig. 27b. Let us first consider a situation where A+A reactions would not differ from p+p by the degree of baryon stopping - respective net baryon spectra would be identical. Then, the P and T contributions would simply pile up with the number of projectile and target wounded nucleons. The total pion spectrum in A+A, scaled down by the number of wounded nucleon (participant) pairs,

---

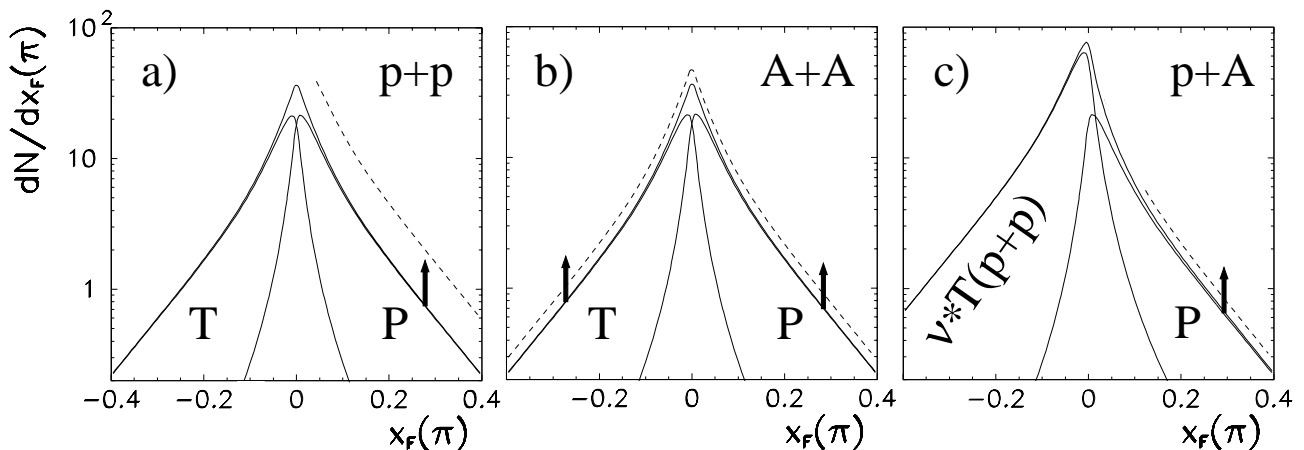[4]This assumption is the simplest possible, and provides a reasonable description of the data.

Figure 27: **a)** Solid: the pion dN/dx_F spectrum in inclusive p+p collisions, presented as sum of two wounded nucleon contributions, T (target), and P (projectile). Arrow: change of P curve with decreasing $x_F(p)$, resulting in the dashed curve (note: the effect is exaggerated). **b)** The pion dN/dx_F distribution in A+A reactions, scaled down by the number of participant pairs. Solid: assuming no differences in baryon stopping between A+A and p+p, dashed: taken account of differences in baryon stopping (the arrows indicate the direction of the change). **c)** The pion dN/dx_F distribution in p+A at $\nu = 3$ elementary subcollisions. The T contribution from p+p reactions piles up linearly with ν. The P contribution increases due to baryon stopping.

would be identical to that in p+p collisions. However, in reality A+A reactions *do* differ by the degree of baryon stopping, in both hemispheres. Thus the P and T contributions in A+A will additionally go up, because corresponding leading baryons are more central than in p+p. The total distribution per participant pair will go up. Its shape will be preserved, but its integral will increase. At the same time, an increase of $<p_T>$ values will take place.

Let us consider several centrality-selected A+A samples. Each will be characterised by a different degree of baryon stopping: with increasing centrality, the average $x_F(p)$ will smoothly decrease (Ch. 2). Thus, the following prediction can be made for the centrality dependence of pion production:

- with increasing centrality, a smooth increase of total pion multiplicity per participant pair will be observed.

- the shape of total pion dN/dx_F spectra will be independent of centrality.
  If normalized, these spectra will be identical to the inclusive p+p distribution.

- pion $<p_T>$ values will smoothly increase with increasing centrality.

The problem of p+A collisions is more complicated, due to the asymmetry between the projectile and the target. In Fig. 27c, the simplest possible assumption is made about the behaviour of the target contribution - due to ν subcollisions of the projectile with target nucleons, it piles up linearly with ν. This results in an increase of forward hemisphere pion multiplicity, and in a steepening of the pion dN/dx_F spectrum at lower positive x_F values. Now, the correlation between the P contribution and baryon number transfer has to be taken into account. Due to projectile baryon stopping the P curve will go up, resulting in a further increase of $<\pi>$. Simultaneously, the forward hemisphere pion $<p_T>$ values will increase. Thus, the overall prediction is the following:

- a smooth increase of $<\pi>$ with increasing centrality.

- a steepening of the pion dN/dx_F spectrum in the central region, caused by the target pile-up. A smooth increase of forward dN/dx_F values with increasing ν, due to baryon stopping. An invariance of shape of the pion spectrum in the forward x_F region.

- an increase of projectile hemisphere pion $<p_T>$ values with increasing centrality.

The main aim of this Chapter being to demonstrate the importance of elementary reactions for our understanding of nuclear collisions, our predictions will remain qualitative as formulated above. While this limits the range of conclusions made in Sec. 3.6, quantitative predictions would require more detailed experimental information, or more assumptions. This problem will be rediscussed in Sec. 3.6.
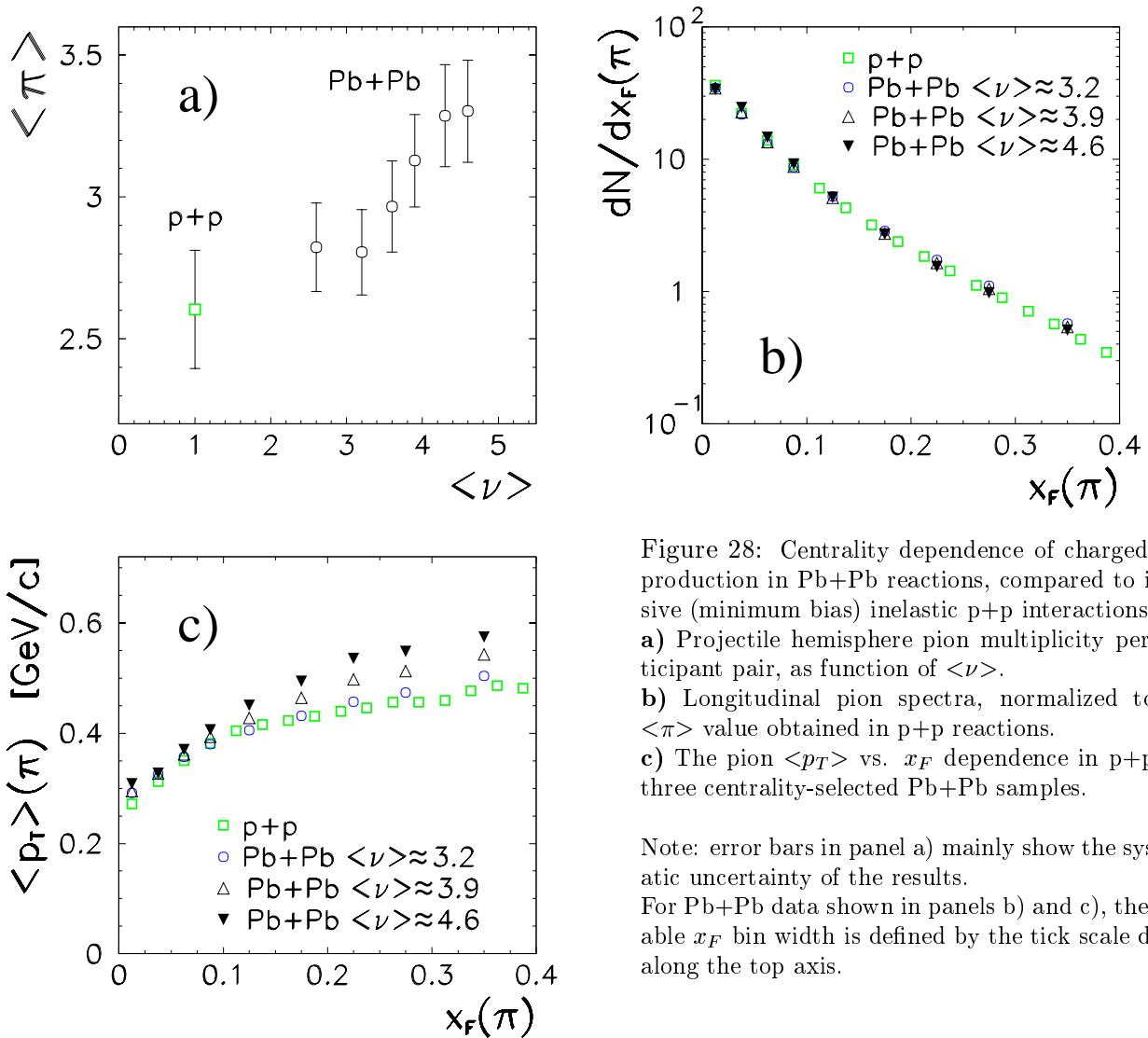
Figure 28: Centrality dependence of charged pion production in Pb+Pb reactions, compared to inclusive (minimum bias) inelastic p+p interactions.
a) Projectile hemisphere pion multiplicity per participant pair, as function of $<\nu>$.
b) Longitudinal pion spectra, normalized to the $<\pi>$ value obtained in p+p reactions.
c) The pion $<p_T>$ vs. x_F dependence in p+p and three centrality-selected Pb+Pb samples.

Note: error bars in panel a) mainly show the systematic uncertainty of the results.
For Pb+Pb data shown in panels b) and c), the variable x_F bin width is defined by the tick scale drawn along the top axis.

3.5 Centrality dependence in nuclear collisions

This Section contains an experimental study of charged pion production in centrality-selected p+Pb and Pb+Pb reactions. The study focuses on verification of predictions formulated in Sec. 3.4. The presentation of the data follows the natural order established by the baryon stopping effect in Ch. 2. First Pb+Pb collisions are presented. Then intermediate p+Pb data, more comparable to Pb+Pb in terms of baryon stopping and centrality, are shown. Finally central p+Pb collisions are discussed.

3.5.1 Pb+Pb collisions

The centrality dependence of pion production in Pb+Pb reactions is shown in Fig. 28, and compared to results on inclusive p+p collisions. The Pb+Pb centrality samples are defined by the mean number of elementary subcollisions $<\nu>$, obtained from the VENUS event generator (Ch. 1). From the six samples given in panel **a)**, three are presented in panels **b)** and **c)**. Note that $<\nu> \approx 4.6$ is the highest Pb+Pb centrality which is practically accessible.

As can be seen in the Figure, each of the considered observables displays a characteristic pattern as function of $<\nu>$. Within large error bars, the forward hemisphere pion multiplicity (panel **a**) shows a smooth increase with centrality. The normalised dN/dx_F distributions (**b**) are closely independent of $<\nu>$, and almost equal to the p+p spectrum. The pion $<p_T>$ values (**c**) increase with $<\nu>$, in a way similar to what has been observed for proton-triggered p+p events - the spread between data points is small at lower pion x_F, and increases in the forward direction. The above trends follow the
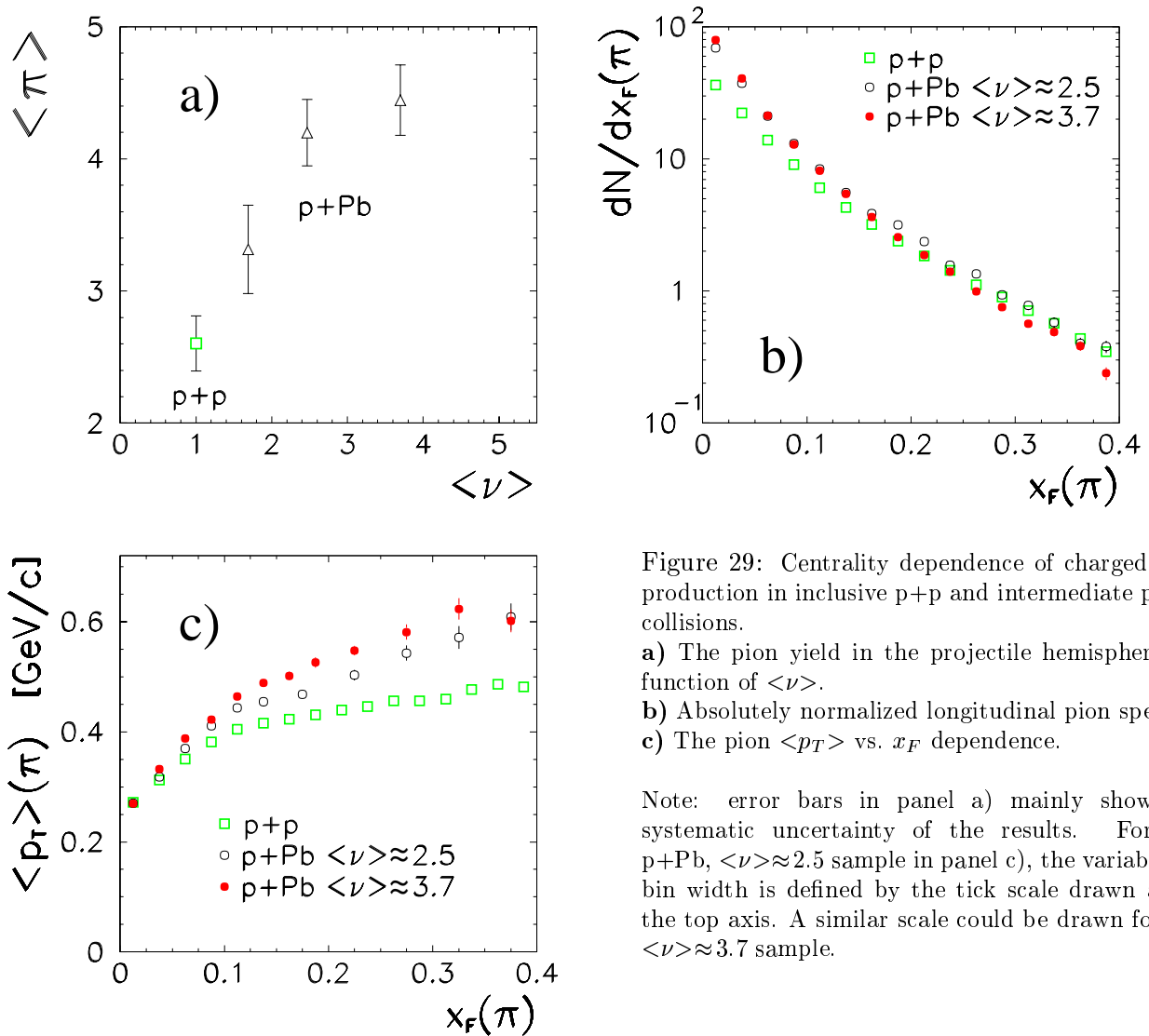
Figure 29: Centrality dependence of charged pion production in inclusive p+p and intermediate p+Pb collisions.
a) The pion yield in the projectile hemisphere, as function of $<\nu>$.
b) Absolutely normalized longitudinal pion spectra.
c) The pion $<p_T>$ vs. x_F dependence.

Note: error bars in panel a) mainly show the systematic uncertainty of the results. For the p+Pb, $<\nu>\approx 2.5$ sample in panel c), the variable x_F bin width is defined by the tick scale drawn along the top axis. A similar scale could be drawn for the $<\nu>\approx 3.7$ sample.

prediction formulated in Sec. 3.4. This means that such trends are *expected* as direct consequence of correlations between pion production and baryon number transfer, observed already in p+p events.

3.5.2 Intermediate p+Pb reactions

The study of intermediate p+Pb data includes three centrality samples, obtained by requesting a given number of grey protons n_{grey} seen in each selected event. The selections are $n_{grey} = 0$, 1 and 3 grey protons. According to the VENUS event generator, they respectively correspond to $<\nu>\approx 1.7$, 2.5, and 3.7 elementary subcollisions suffered by the projectile.

The experimental results are shown in Fig. 29. The general behaviour of the data follows the prediction made in Sec. 3.4. The forward hemisphere pion multiplicities (panel **a**) follow a smooth increase with centrality. This increase is faster than in Pb+Pb collisions (Fig. 28a). This can be attributed to the target pile-up effect discussed in Sec. 3.4. The same pile-up effect is apparent in the low x_F region of longitudinal pion spectra (panel **b**). As expected, the shape of these spectra in the forward region changes little. Finally, a smooth increase of $<p_T>$ values with centrality is apparent in panel **c**). Similarly to Pb+Pb reactions, the basic features of pion production in intermediate p+Pb collisions are *expected* from the simple picture proposed in Sec. 3.4.

It is worthwhile to note that the maximal value of $<\nu>\approx 3.7$ considered here corresponds also to minimum bias p+Pb reactions. Thus, any analysis *without* p+A centrality control would have to stop at this $<\nu>$ value. The question is whether the possibility of selecting extremely central p+A collisions can provide us with further insight.

3.5.3 Central p+Pb reactions

In addition to the data samples used in Sec. 3.5.2, this study includes a subset of central p+Pb collisions, obtained by the $10 \leq n_{grey} \leq 25$ selection. This corresponds to $<\nu> \approx 6.3$ elementary subcollisions. Note that this p+Pb sample has been analyzed in Ch. 2. It is characterized by an extreme degree of baryon stopping. The study includes also a summed intermediate sample, obtained by the $0 \leq n_{grey} \leq 3$ cut, and corresponding to $<\nu> \approx 3.1$.

Fig. 30 shows the results of comparison between intermediate and central p+Pb data. The three panels are discussed below.

a) The centrality dependence of projectile hemisphere pion yield displays a saturation, if not a decrease, at higher p+Pb centralities. This behaviour does not follow the prediction made in Sec. 3.4 - a smooth increase with centrality was anticipated.

b) The prediction anticipates a constant shape of the pion dN/dx_F distribution in the forward x_F region. Moreover, the distribution is expected to go up, due to baryon stopping. Instead, a steepening of the absolutely normalized dN/dx_F spectrum is observed for central p+Pb reactions. At $x_F \approx 0.4$, this steepening results in a decrease of the dN/dx_F value by a factor of three, if compared to inclusive p+p collisions.

c) An increase with centrality is observed for pion $<p_T>$ values. This trend is in basic agreement with the prediction. The effect is large. For central p+Pb reactions, it exceeds by a factor of two the corresponding effect observed in central Pb+Pb data[5].

As can be seen from items **a)** and **b)**, the results on most central p+Pb collisions do not agree with the prediction presented in Sec. 3.4. At least for pion dN/dx_F spectra and forward hemisphere multiplicities, significant deviations appear.

Thus, the overall centrality dependence of p+Pb collisions displays the following pattern: up to some centrality, the main trends in the data follow the prediction. Then deviations appear. This suggests that in fact a mixture of two ingredients is observed: **1)** the predicted behaviour, dominating at low $<\nu>$ values, and **2)** an unpredicted effect, dominating at higher centralities, and manifesting itself by a saturation of forward hemisphere pion multiplicities and a depletion of forward dN/dx_F values. It is difficult to judge at which centrality this second effect takes over. At $<\nu> \approx 3.1$ elementary subcollisions, a very small depletion of the forward part of the dN/dx_F spectrum could already be present in the data. Note that the $<\nu> \approx 3.7$ sample in Fig. 29b seems to display a similar behaviour. However, both depletions are comparable to the inherent uncertainties of this study. Moreover, both $<\nu>$ values come from broad ν distributions (Ch. 1), with sizeable contributions of higher centralities.

3.6 Discussion

This Section contains an attempt to understand the information presented in Sec. 3.5. First, a few conjectures about the behaviour of p+Pb collisions at high centralities are made. Then, the general behaviour of both Pb+Pb and p+Pb reactions is discussed.

3.6.1 What is happening in central p+Pb collisions?

The results shown in Fig. 30 suggest that a simple extrapolation of correlations observed in elementary p+p events is not sufficient to fully describe the data on high-centrality p+Pb reactions. Thus, it can be

---

[5]This phenomenon is not described by the VENUS 4.12 event generator. The model predicts a greater increase for central Pb+Pb than for central p+Pb reactions [29].
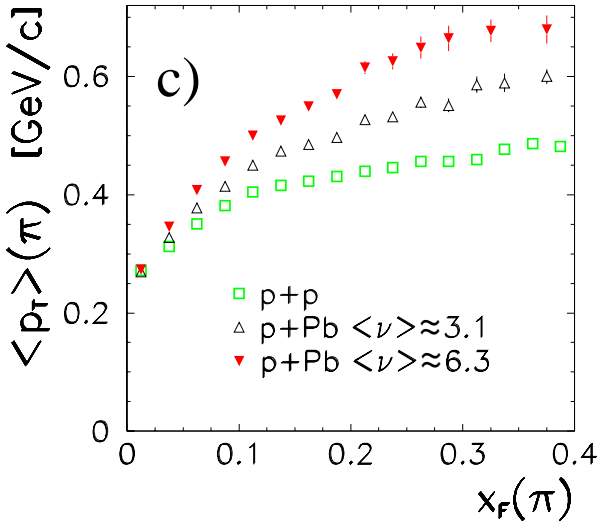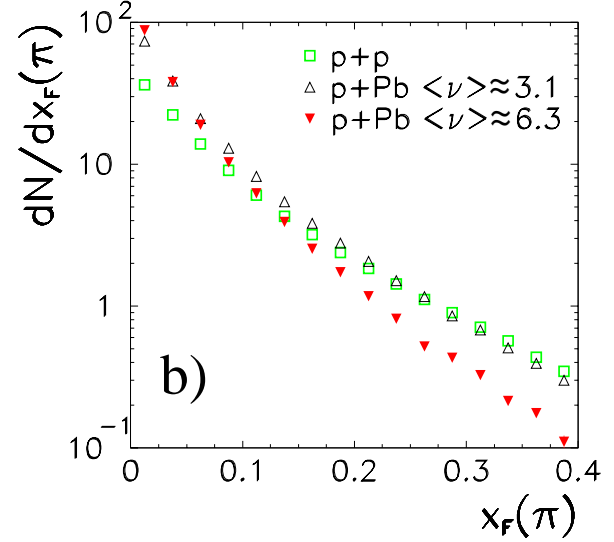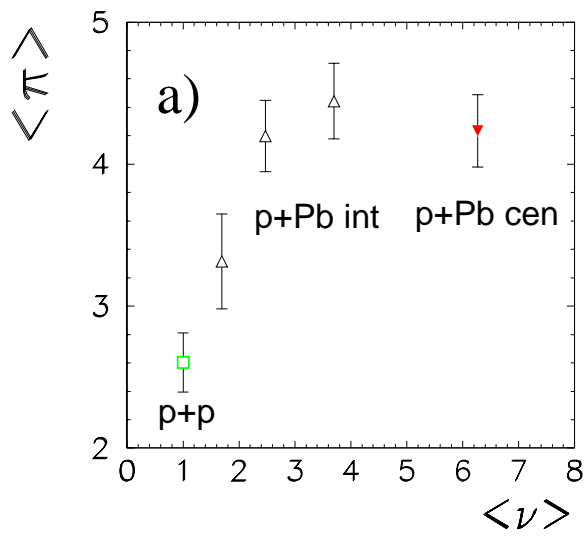
Figure 30: Centrality dependence of charged pion production in p+p, intermediate p+Pb, and central p+Pb collisions.
a) The pion yield in the projectile hemisphere, as function of $<\nu>$. The p+p and p+Pb int (intermediate) data points have been shown before.
b) Absolutely normalized longitudinal pion spectra in p+p, summed intermediate p+Pb ($<\nu>\approx3.1$) and central p+Pb ($<\nu>\approx6.3$) collisions.
c) The pion $<p_T>$ vs. x_F dependence.

Note: error bars in panel a) mainly show the systematic uncertainties.

tentatively assumed that the additional, unpredicted effect postulated in Sec. 3.5.3 is non-elementary, i.e. characteristic to *multiple* collisions of the projectile inside the nuclear target.

A candidate for such an additional effect could be a possible energy loss of the projectile in each subcollision. In a picture in which the p+Pb interaction is composed of subsequent elementary collisions of the projectile with the target nucleons, the *first* interaction would be similar to a p+p collision at 158 GeV beam energy ($\sqrt{s}\approx17.3$ GeV). However, if in this interaction the projectile lost energy (or momentum), the *second* interaction would be described by a different c.m. system and a different $\sqrt{s}$ value. Such a c.m.s. modification could result in a deformation ("pushing back", "changing the scale") of pion dN/dx_F spectra, and thus also in lowering of forward hemisphere multiplicities. Due to this c.m.s. modification, the pion dN/dx_F spectra would not anymore be exclusively defined by the final state baryon x_F position and simple superposition effects. Thus, the prediction made in Sec. 3.4 would be too simplified to fully describe the data.

It is somewhat intriguing that the steepening of pion dN/dx_F spectra is not visible in Pb+Pb collisions. One evident reason for this would be their lower effective centrality. As has been said in Ch. 2, a central Pb+Pb reaction can be imagined as composed from both central and peripheral p+Pb interactions. The extreme centrality p+Pb sample, for which the effect is very clearly seen, is beyond reach in Pb+Pb data. Thus, if at all, the effect should be less visible in Pb+Pb reactions. Further conjectures could be made, but the whole problem needs further studies at a more quantitative level.

3.6.2 A tentative interpretation of the data

The effects observed in central p+Pb reactions demonstrate the importance of p+A centrality control in comparative studies of p+p, p+A and A+A collisions. However, they should not overshadow the main result emerging from Sec. 3.5. Over the whole centrality range in Pb+Pb, and a sizeable centrality range in p+Pb reactions, the main trends observed in pion production follow the prediction made in Sec. 3.4. This means that such trends are expected as direct consequence of internal correlations observed in p+p events, account taken of differences in baryon stopping discussed in Ch. 2. This requires a conscientious discussion, which is the aim of this Section.

First, the purely *qualitative* success of the above prediction cannot be treated as direct proof that pion production in intermediate p+Pb and Pb+Pb collisions brings no new elements relative to elementary reactions. Such a statement would require a different, more advanced study. Similarly to the qualitative expectations formulated in Sec. 3.4, exact *quantitative* predictions for the behaviour of pion production in p+Pb and Pb+Pb interactions would have to be produced. Attempts in that direction have been made but the problem is very difficult. Most of all, it requires a more extended knowledge of the correlation between pion production and baryon number transfer. Let us list two among many problems. First, the study would have to be extended to leading neutrons. Second, it would have to be extended to the negative leading baryon x_F region, as the projectile component of net baryon spectra extends into the backward hemisphere (Ch. 2). Apart from such experimental difficulties, the conceptual problem how the extrapolation from p+p to p+Pb and Pb+Pb reactions should exactly be made would have to be further clarified.

Therefore, a slightly more complex interpretation is indicated. The basic importance of the presented results lies in the fact that elementary events show characteristics which are closely connected with phenomena observed in nuclear reactions. The mere fact that extrapolations from Sec. 3.4 anticipate the right *directions and trends* in centrality dependence of pion production indicates that effects seen in p+Pb and Pb+Pb reactions have a significant "elementary ingredient" - at least a part of them can be explained on the basis of p+p events. This conclusion may seem not spectacular, but it has very important consequences. A measured change of a given quantity relative to *inclusive* p+p collisions does not automatically indicate any "new" mechanism of pion production. The understanding of such an experimental observation may change, once internal correlations in p+p events and baryon stopping effects are properly taken into account. Instead of a new feature of pion production, characteristic to nuclear collisions, it may as well appear just a consequence of phenomena present already in p+p reactions - of the correlation between pion production and baryon number transfer. The measured effect may also be a mixture of "old" (elementary) and "new" (non-elementary) phenomena. Clearly, a careful analysis of baryon stopping effects and of internal correlations in p+p events is required in order to disentangle these two ingredients.

This problem has another important aspect: the qualitative success of the prediction suggests that various features of pion production are similar in the three reaction types: p+p, p+Pb and Pb+Pb. For instance, the smooth evolution of the three considered observables with centrality, presented for Pb+Pb data in Fig. 28, suggests that the correlation between pion production and leading baryon x_F resembles that observed in p+p reactions (Fig. 26). Thus, a further study of baryon number transfer and pion production in p+p reactions will provide insight into nuclear collisions as well.

Finally, the deviation of data on central p+Pb reactions from the predicted behaviour also has consequences. It suggests that once elementary effects are taken into account, non-elementary phenomena characteristic to multiple subcollisions can be isolated. Results on central p+Pb collisions suggest the presence of such phenomena. In other terms, the overall centrality dependence of pion production in p+Pb reactions would not be uniquely a consequence of internal correlations observed in p+p events. Logically, this should also have repercussions on A+A collisions, although more studies are required. What is clear is that centrality control in p+A provides a possibility of studying such phenomena in extreme ($<\nu> \approx 6$) centrality conditions. Experimentally, this possibility is not available for A+A reactions.

3.7 Summary

While Ch. 2 presented a common picture of baryon number transfer in elementary and nuclear collisions, the main subject of Ch. 3 was the correlation between baryon number transfer and charged pion production in p+p collisions, and its consequences for p+Pb and Pb+Pb reactions. It appeared that a simple extrapolation of correlations observed in p+p events, taking baryon stopping phenomena into account, qualitatively reproduces the main trends in pion production in Pb+Pb and intermediate p+Pb interactions. This leads to the conclusion that already in p+p collisions, dynamical features exist which could at least partially explain the phenomena observed in nuclear reactions. Therefore, changes observed relative to inclusive p+p collisions do not automatically indicate new mechanisms of pion production.

The same extrapolation has proven insufficient to predict the trends observed in central p+Pb interactions. This suggests the presence of additional phenomena, characteristic to multiple collisions of the projectile inside the nuclear target. Possible consequences of this observation for A+A reactions remain to be elucidated.

The strategy of the following Chapter will be to concentrate on the elementary p+p collisions, trying to reach additional understanding of such phenomena as baryon number transfer and pion production. Specifically, the role of hadronic resonance production in these phenomena will be investigated.

Chapter 4. Consequences of Resonance Production

This Chapter contains a study of the role of hadronic resonance production in phenomena observed so far. This study is limited to p+p collisions. The effects considered are baryon number transfer, positive pion production, and some of the observed correlations. The analysis includes the following set of hadronic excited states: $\Delta^{++}(1232)$, $\rho^0(770)$, and $\rho^+(770)$.

First, the motivation underlying this study is explained. Then the experimental data analysis and Monte-Carlo methods are discussed. Finally, the results of the study are shown.

4.1 Motivation

The study made in Chapters 2 and 3 brought two main findings: **1)** the phenomenon of baryon number transfer follows a common behaviour in p+p, p+Pb and Pb+Pb collisions, and **2)** the process of pion production in p+p interactions displays characteristic features which can at least partially explain the effects observed in p+Pb and Pb+Pb reactions. These findings suggest that various features of baryon number transfer and pion production will be similar in the three reaction types: p+p, p+Pb and Pb+Pb. Furthermore, the analysis of correlations in p+p events provides a way to identify the above similarities, and thus also to isolate differences between elementary and nuclear collisions. Therefore, a further study of baryon number transfer and pion production effects in the (relatively simplest) p+p interactions is highly indicated, and will provide insight also into nuclear reactions.

Seen in this context, the analysis of the role of resonance production in these effects appears simply as a necessity. This is due to the "resonance dominance" observed for hadron+hadron reactions: it is known that most particles produced in these reactions originate from resonance decays[1]. Let us quote two estimates. In π^++p reactions at $p_{beam} = 16$ GeV/c ($\sqrt{s} \approx 5.6$ GeV), already the contribution of ρ^0 and ω states gives 44% of the total produced π^- yield [30]. Another estimate, made for inelastic p+p collisions at $\sqrt{s} = 53$ GeV, gives 10.3 ± 1.2 charged secondaries originating per event from ρ, ω and $K^*(890)$ decays. Comparing this to the average multiplicity of 10.1 ± 1.5 charged pions and kaons produced per event, the authors conclude that more than 60% (at 95% confidence level) pions and kaons result from vector meson decay [31]. The two numbers quoted above are obviously very large, account taken that additional contributions from other excited states (like baryonic resonances) should also be taken into account. What is more, it is known that the presence of resonance excitations influences the internal correlations observed in hadron+hadron events [32]. It seems therefore that for any effect observed in hadron+hadron collisions, the role played by resonance production is to be clarified.

The aim of the analysis presented in this Chapter is to estimate this role in phenomena studied in Chapters 2 and 3. The analysis is limited to p+p reactions. It is focussed on three main aspects:

1. What is the role of resonance decays in the process of baryon number transfer? To what extent can they be held responsible for the final shape of, e.g., net proton dN/dx_F spectra?

2. How do they contribute to charged pion production? How does this contribution distribute over phase-space?

3. Do they have any influence on the correlations between pion production and the x_F of the leading proton, discussed in Ch. 3?

The study is made by means of a Monte-Carlo simulation, based on existing data on baryonic and mesonic resonance production in inclusive p+p collisions. It concentrates on simulated distributions of resonance products: protons and positive pions. The dN/dx_F spectra, invariant p_T distributions, and $<p_T>$ vs. x_F dependencies are considered. These simulated results are compared to experimental

---

[1]The term "resonance dominance" is used in review [4] and applies also to e^+e^- and lepton+hadron interactions. The discussion made in the above paragraph is to a large extent based on this review. A much more detailed discussion can be found therein.

data on inclusively produced protons and π^+.

As pointed out in [4] (see [33] for a more technical discussion), the extraction of hadronic resonance cross-sections in inelastic p+p reactions at our energies is very difficult. This is due to the presence of many particles in the final state, resulting in a large combinatorial background. Nevertheless, the inclusive production of some low-lying excited states like $\Delta(1232)$ and $\rho(770)$ is known in terms of e.g. $d\sigma/dx_F$ distributions. The $\Delta^{++}(1232)$ state has been measured in the $\Delta \rightarrow p\pi$ channel in the $\sqrt{s}$ range of 27.5 to 62 GeV [34, 35]. The $\rho^{0,\pm}(770)$ states have been studied at $\sqrt{s} = 27.5$ GeV in the $\rho \rightarrow \pi\pi$ channel [34]. For this reason, in this Chapter we shall discuss the role played by the following resonance decays: $\Delta^{++}(1232) \rightarrow p\pi^+$, $\rho^0(770) \rightarrow \pi^+\pi^-$, and $\rho^+(770) \rightarrow \pi^+\pi^0$.

4.2   Data analysis

This Chapter contains several experimental results which were not shown in Chapters 2-3. These are the dN/dx_F spectrum, invariant p_T distribution and $<p_T>$ vs. x_F dependence of positive pions, and additionally the net proton invariant p_T distribution and the proton $<p_T>$ vs. x_F dependence. All these results have been obtained in inclusive inelastic p+p reactions.

For positive pions, all the results are obtained by an analysis identical to that presented in Ch. 3 for inclusive p+p data. The systematic errors of the dN/dx_F spectrum and of the $<p_T>$ values will be similar to those obtained therein for summed charged pions ($\pi^+ + \pi^-$).

The results on protons (and net protons) are obtained by an analysis similar to that presented in Sec. 2.2.1 for p+Pb collisions. The only difference is that the *trigger loss correction* is additionally applied on appropriate distributions (see Sec. 2.1.1 for discussion). As a precise estimate of systematic errors of proton $<p_T>$ values is still to be worked out, a pessimistic assumption of 40 MeV/c has been made. Such an accuracy is sufficient for the present relatively rough study.

A comment should be made about the pion and proton invariant p_T distributions. These are $\frac{E}{p_T}\frac{d^2N}{dx_F dp_T}$ spectra, normalized per inelastic p+p event. As follows from Sec. 3.2.1, these spectra are not corrected for *feed-down from weakly decaying particles*. They are preliminary, and presented only for the purpose of rough comparisons.

4.3   The Monte-Carlo

The Monte-Carlo procedure presented in this Section simulates the production and decay of Δ^{++}, ρ^0 and ρ^+ resonances in inclusive inelastic p+p collisions. It is based on existing data [34, 35], and consists of two steps. First, a given parent particle (Δ^{++}, ρ^0, or ρ^+) is emitted, with a given mass, according to a given inclusive distribution, and with a given normalisation weight corresponding to its average multiplicity per p+p event. Then the hadronic decay of this parent particle is simulated. Below main details of the Monte-Carlo are described, and a few exemplary results are presented.

4.3.1   Resonance mass

The problem of mass distribution according to which the parent particle should be generated is quite difficult. A *resonance formation* process (like $\pi^+ + \pi^- \rightarrow \rho^0 \rightarrow \pi^+ + \pi^-$) could be described by the suitable relativistic Breit-Wigner function [36], at least close to the central mass of the resonance. However, what to do with *resonance production* processes considered here?

This problem is discussed in a published study of ρ^0 production in $\pi^+ + $p reactions at lower energies, made in the $\rho \rightarrow \pi\pi$ channel [37]. The authors of the quoted paper report that the ρ^0 contribution to the effective mass spectrum of combined $\pi^+\pi^-$ pairs *cannot* be described uniquely by a Breit-Wigner function. Therefore they propose to describe the total effective mass spectrum by the following formula:

$$\frac{d\sigma}{dM} = BG(M) + BW(M) \cdot PS(M) \tag{4.1}$$

Here, $BG(M)$ stands for the combinatorial background, and $BW(M)$ is the P-wave Breit-Wigner function corresponding to the $\rho^0 \rightarrow \pi^+\pi^-$ decay. $PS(M)$ is a phenomenological factor decreasing

with M. Applying this factor results in an effective damping of the Breit-Wigner function at higher M values. The formula (4.1) provides a far better description of effective mass spectra[2]. A similar phenomenological approach is used in other studies of ρ^0 and Δ^{++} production [38, 39].

Our Monte-Carlo follows a similar philosophy. The mass M of the parent resonance is generated according to the probability distribution:

$$\frac{dP}{dM} \sim BW(M) \cdot PS(M) \tag{4.2}$$

Here, $BW(M)$ is the relativistic Breit-Wigner function [36] corresponding to a given decay: $\Delta^{++} \to p\pi^+$, $\rho^0 \to \pi^+\pi^-$, or $\rho^+ \to \pi^+\pi^0$. The central mass and width of the resonances are taken from [16]. The following simple form is assumed for the $PS(M)$ factor:

$$PS(M) = \begin{cases} 1, & \text{if} \quad M < 1.2M_R \\ \frac{M_D - M}{M_D - 1.2M_R}, & \text{if} \quad 1.2M_R \leq M \leq M_D \\ 0, & \text{if} \quad M > M_D \end{cases}$$

Here, M_R is the central mass of the resonance. The damping parameter M_D is assumed 2 GeV/c^2 for all considered resonances. It is important to underline that similarly to [37], the need of applying the $PS(M)$ factor has been checked. A tentative simulation has been performed assuming $PS(M) \equiv 1$ up to 5 GeV/c^2, separately for Δ^{++} and ρ resonances. The result is unacceptable: in both cases the yield of daughter positive pions at $p_T \approx 2$ GeV/c exceeds the total inclusive yield of experimentally observed π^+.

Let us make an additional remark. As can be seen from the above discussion, assumptions made about the resonance mass distribution may influence certain spectra of resonance products. This problem is particularly important for p_T distributions of pions originating from Δ^{++} decay. For instance, the drastic assumption that this resonance decays *only* at its central mass ($M \equiv M_R$), i.e. that its width and Breit-Wigner tail can be neglected, results in π^+ distributions which are visibly more concentrated at low p_T values. The above problem introduces some uncertainties in the study presented in this Chapter. Most important among these uncertainties will be followed in the discussion of results, made in Sections 4.4-4.6.

4.3.2 Kinematic distributions

Once the parent resonance mass M has been obtained from (4.2), its kinematic variables are generated according to a factorized inclusive distribution:

$$\frac{d^2N}{dy_r dp_T} = norm \cdot f(y_r) \cdot g(p_T) \tag{4.3}$$

where y_r is the reduced rapidity of the resonance, $y_r = y/y_{\max}$, $y_{\max}$ being its maximum allowed rapidity:

$$y_{\max}(p_T) = \ln\left(\frac{E_{\max} + p_{L_{\max}}}{m_T}\right), \qquad \text{where}$$

$$p_{L_{\max}} = \sqrt{E_{\max}^2 - m_T^2}, \qquad m_T = \sqrt{M^2 + p_T^2},$$

and the maximum energy $E_{\max}$ is assumed equal to $\sqrt{s}/2$. The normalisation weight factor $norm$ corresponds to the average resonance multiplicity per inelastic p+p event, while $f(y_r)$ and $g(p_T)$ are appropriate probability density distributions. The relatively simple formula (4.3) insures that the emission of the parent particle does not violate kinematical limits. It has been checked that when appropriately adjusted to experimental data, this formula roughly describes pion and proton production in inclusive p+p reactions, within NA49 acceptance. Finally, as the normalisation factor $norm$ is adjusted to experimental data on Δ^{++} and ρ production, all distributions resulting from

---

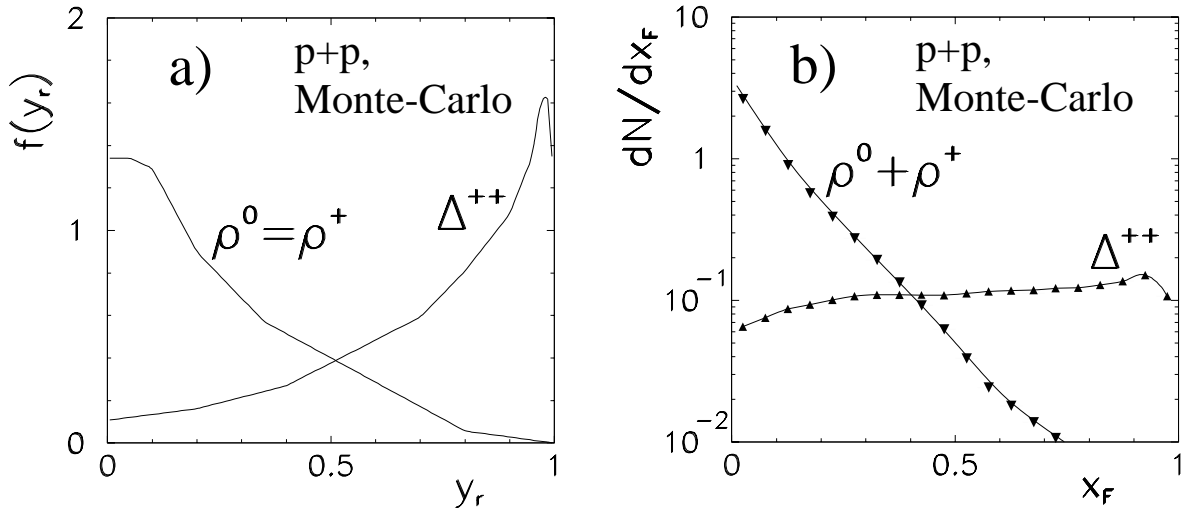[2]The above description is somewhat simplified, see [37] for full description.

Figure 31: **a)** Adjusted $f(y_r)$ probability density functions for the ρ^0, ρ^+ mesons, and for the Δ^{++} baryon. Note that the functions are symmetric around $y_r = 0$. **b)** Simulated longitudinal spectrum of summed ρ^0 and ρ^+ mesons, and of the Δ^{++} baryon. Both dN/dx_F spectra are absolutely normalized. Their statistical errors are smaller than the symbol size. The solid curves serve merely to guide the eye.

the simulation are *absolutely normalised*. Therefore they can be directly compared to appropriate experimental spectra, as it is done in the next Sections.

The transverse distribution of the ρ^0 meson is assumed in the form $g(p_T) \sim p_T \cdot e^{-4p_T}$, where p_T is measured in GeV/c. This form is suggested by the shape of pion p_T spectra. The ρ^0 longitudinal distribution $f(y_r)$ is adjusted to its experimental dN/dx_F spectrum at $\sqrt{s} = 27.5$ GeV, obtained from the measured $d\sigma/dx_F$ spectrum [34] assuming $\sigma_{inel} \approx 32.8$ mb [40]. The adjusted $f(y_r)$ function is shown in Fig. 31a. The normalisation factor *norm* is also adjusted on the basis of the dN/dx_F spectrum. It is scaled down by 12% in order to take account of energy dependence of the total cross-section for ρ^0 production [41]. This gives a final normalisation of about 0.35 ρ^0 mesons per inelastic p+p event.

An identical procedure is applied for the ρ^+ meson. The same $g(p_T) \sim p_T \cdot e^{-4p_T}$ form is assumed for its transverse distribution. As the experimental $d\sigma/dx_F$ spectra of the ρ^+ and ρ^0 are roughly similar [34], the same $f(y_r)$ functions are used. As the adjusted ρ^+ normalisation factor is also scaled down by 12%, it also comes close to 0.35 per event.

Being characterised by identical $g(p_T)$ and $f(y_r)$ functions, the ρ^0 and ρ^+ resonances will be taken together in this study. Fig. 31b shows their summed dN/dx_F spectrum, resulting from the simulation.

For the Δ^{++} baryon, the transverse distribution is assumed in the form $g(p_T) \sim p_T \cdot e^{-3p_T^2}$. This is inspired by the shape of proton p_T spectra. Similarly to ρ mesons, the $f(y_r)$ function and the normalisation factor are adjusted to describe the measured longitudinal Δ^{++} spectra [34, 35]. The $f(y_r)$ function is shown in Fig. 31a. The description of the quoted data that it provides is rough, and the agreement does not extend below $|x_F(\Delta^{++})| = 0.1$. In this central region, the experimental Δ^{++} spectrum is expected to contain a sizeable contribution from baryon-antibaryon pair production. As the $\Delta^{++} \to p\pi^+$ decay is considered here mainly in view of baryon number transfer studies (made by means of *net* baryon distributions), it is undesirable to include this contribution. The quoted data do not indicate a need of changing the adjusted normalisation factor with energy. This gives us a final normalisation of 0.22 Δ^{++} baryons per inelastic p+p event. The dN/dx_F spectrum of the Δ^{++} resulting from the simulation is presented in Fig. 31b.

4.3.3 The decay

After the emission of the parent resonance, its hadronic two-body decay is simulated. For each of the three considered decays, a 100% branching fraction is assumed, in good agreement with [16]. The simulation altogether neglects any polarization effects. Thus, an isotropic angular distribution is
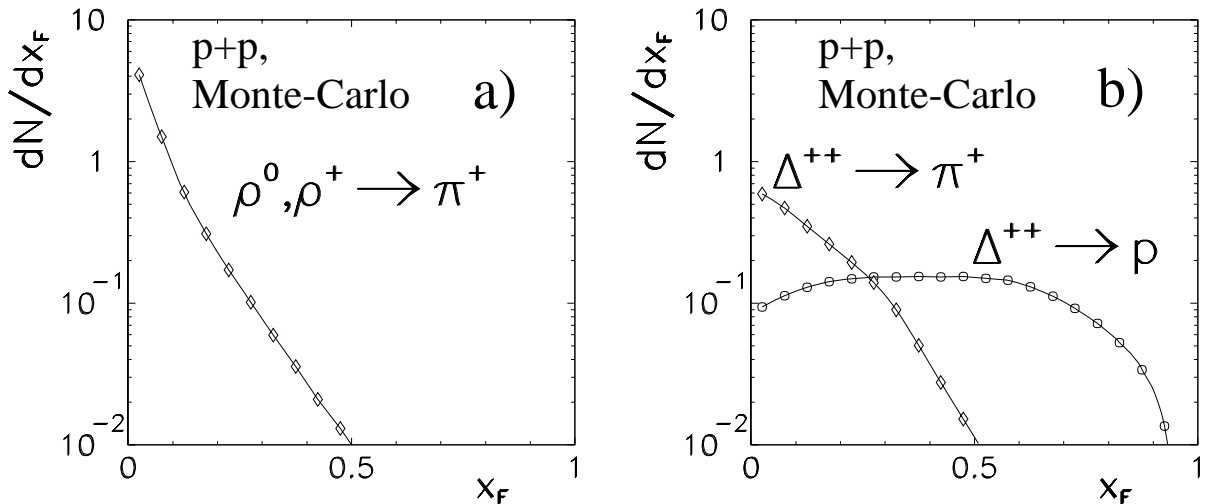
Figure 32: Simulated distributions of resonance products. **a)** Positive pions originating from $\rho^0 \to \pi^+\pi^-$ and $\rho^+ \to \pi^+\pi^0$ decays. **b)** Positive pions and protons resulting from $\Delta^{++} \to p\pi^+$ decays. All distributions are absolutely normalized. Statistical errors are smaller than the symbol size. Solid curves serve merely to guide the eye.

assumed for decay products.

All spectra of decay products presented in this Chapter refer to the collision c.m.s. Figure 32 shows the simulated dN/dx_F distributions of protons and π^+ originating from decays of ρ^0, ρ^+ mesons (taken together in panel **a**) and of the Δ^{++} baryon (panel **b**). The ρ decay results in a steep pion spectrum, which extends over more than two orders of magnitude in the x_F range of 0 to 0.5. As could be expected in the Δ^{++} case, the proton and π^+ distributions are very different. The proton inherits the larger part of longitudinal momentum of its parent Δ^{++}.

After this presentation of Monte-Carlo methods, the results of the study can be discussed. This discussion starts with the role of the Δ^{++} resonance in the process of baryon number transfer.

4.4 Baryon number transfer

The transfer of baryon number from the projectile to the final state proton has been studied in Ch. 2 by means of net proton $(p - \bar{p})$ longitudinal spectra. These spectra are also studied in this Section. Additionally, main features of net proton transverse momentum behaviour are investigated.

The first point of this discussion is a simple but important observation, illustrated by Fig. 33a. The Figure compares the longitudinal spectrum of the Δ^{++} resonance to that of protons originating from the $\Delta^{++} \to p\pi^+$ decay. The proton spectrum is visibly more central than that of its parent Δ^{++}. The mean values of the two distributions (shown in the Figure), are 0.54 for the Δ^{++} and 0.41 for the proton. Thus, even if the proton inherits the majority of Δ^{++} momentum, the decay of this resonance provides an *evident mechanism for baryon number transfer* down to lower x_F values. On the basis of the discussion made in Chapters 1 and 2, one could say the following. Whenever it is present in the p+p event, the $\Delta^{++} \to p\pi^+$ decay constitutes a *last stage* of an overall process of transfer of baryon number from the incoming to the final state proton. Its contribution to the total effect is sizeable: it accounts for some 25% of the total "loss" of longitudinal momentum, typically observed between the projectile and the final state proton.

Fig. 33b shows the inclusive net proton spectrum in p+p reactions, compared to the corresponding distribution of Δ^{++} decay products. As both distributions are absolutely normalised, the Figure illustrates the contribution of Δ^{++} daughters to the total inclusive spectrum. Everywhere outside the diffractive region, this contribution is very sizeable. The *relative* contribution is quite uniform in x_F: it remains between 20 and 30% everywhere below $x_F = 0.7$.

A view at the transverse momentum behaviour is given in Fig. 33c. The inclusive proton $<p_T>$ vs. x_F dependence in p+p reactions is very different from that shown for pions in Ch. 3. The proton $<p_T>$ appears roughly constant between $x_F = 0$ and 0.5. Qualitatively, this behaviour is very similar to that
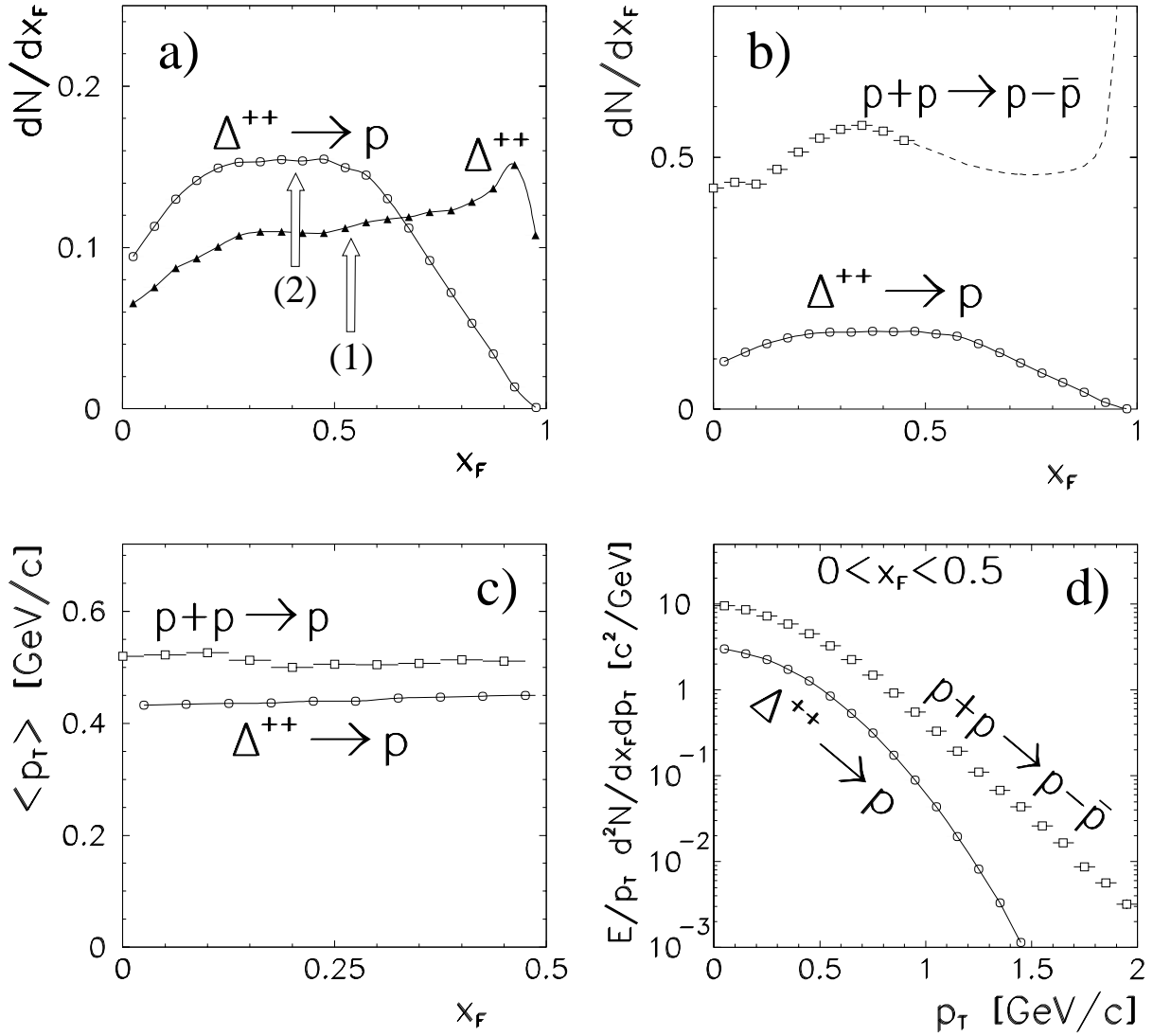
Figure 33: **a)** Simulated longitudinal spectra of Δ^{++} baryons and of their daughter protons. Both spectra have been shown before. Arrows give mean values of the two distributions, calculated in the region $0 < x_F < 1$, and marked (1) and (2) for Δ^{++} and protons, respectively. **b)** Comparison between the experimental net proton spectrum in inclusive p+p reactions (shown in Ch. 2), and the simulated distribution of protons coming from Δ^{++} decay. **c)** Experimental $<p_T>$ vs. x_F dependence of inclusive protons in p+p reactions, compared to that of Δ^{++} daughters. **d)** Invariant p_T spectrum of inclusive net protons in p+p reactions, compared to that of Δ^{++} daughters. Both p_T spectra are obtained in the region $0 < x_F < 0.5$.

displayed by Δ^{++} resonance products, even if the quantitative $<p_T>$ values differ by 50-100 MeV/c. The results shown in the Figure being limited to the first moment of the p_T distribution, the invariant net proton p_T spectrum is shown in Fig. 33d. It is compared to the corresponding spectrum obtained for Δ^{++} products. The shapes of the two distributions display general similarities, although the simulated spectrum is steeper. The quantitative Monte-Carlo results shown in Figs 33c and 33d should be taken with some caution. The exact $<p_T>$ values and the detailed shape of the p_T spectrum will depend on details of the Monte-Carlo, like the exact functional shape of the $PS(M)$ factor, or that of the p_T spectrum assumed for the Δ^{++} resonance. One can nevertheless conclude that a set of reasonable assumptions made about the Δ^{++} behaviour results in a weak $<p_T>$ vs. x_F dependence of daughter protons, similar to that observed in inclusive p+p events. Moreover, the overall shape of the daughter proton p_T distribution is not very different from the total inclusive p_T spectrum[3].

Altogether, the $\Delta^{++} \to p\pi^+$ decay appears to play a significant role in the process of baryon

---

[3]The fact that Fig. 33c shows experimental $<p_T>$ values of *all* inclusive protons instead of *net* protons can be neglected. Rough estimates of antiproton $<p_T>$ indicate that net proton $<p_T>$ values are similar to what is shown in the Figure.
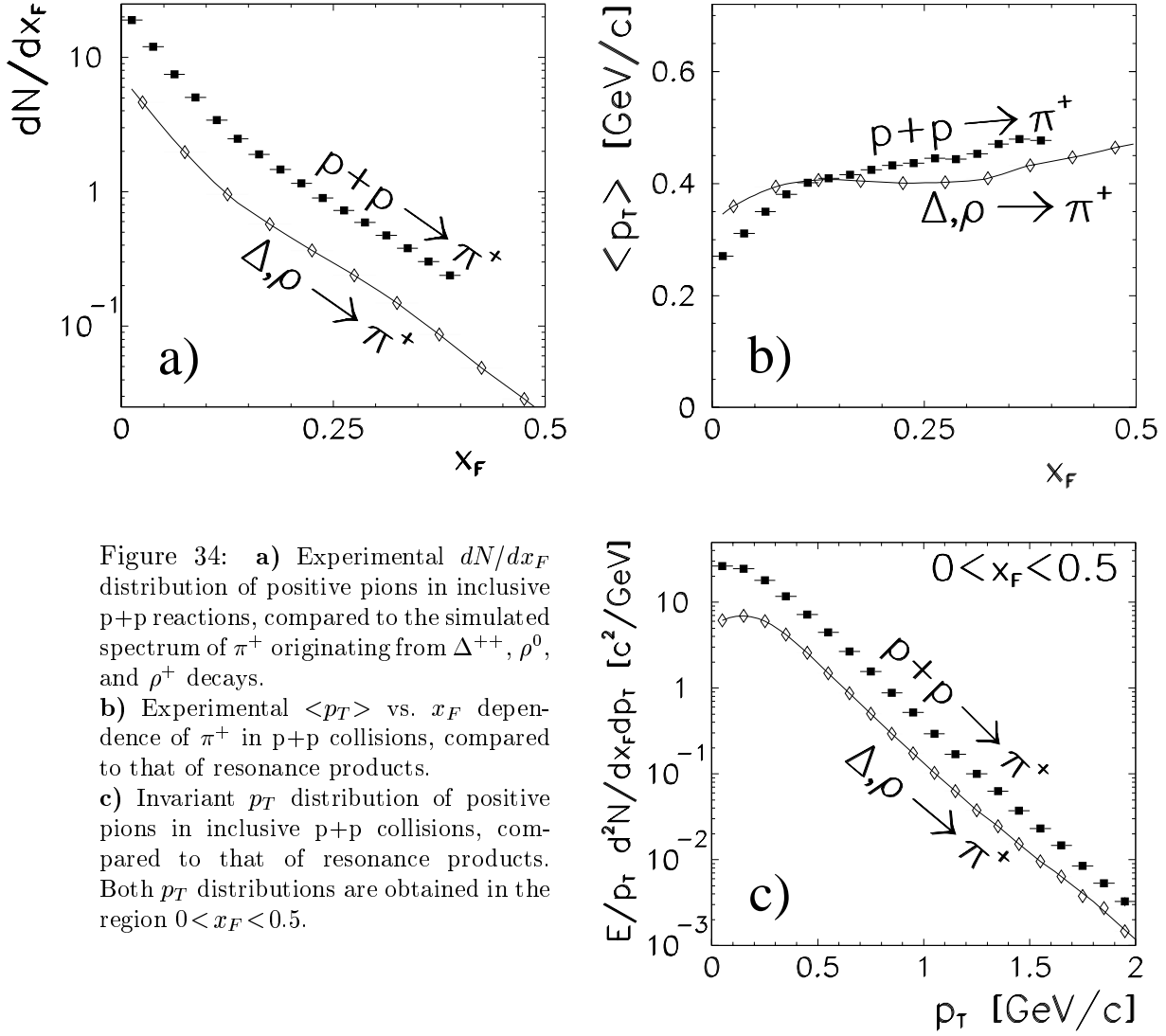
Figure 34: **a)** Experimental dN/dx_F distribution of positive pions in inclusive p+p reactions, compared to the simulated spectrum of π^+ originating from Δ^{++}, ρ^0, and ρ^+ decays.
b) Experimental $<p_T>$ vs. x_F dependence of π^+ in p+p collisions, compared to that of resonance products.
c) Invariant p_T distribution of positive pions in inclusive p+p collisions, compared to that of resonance products. Both p_T distributions are obtained in the region $0 < x_F < 0.5$.

number transfer in p+p reactions: it provides a mechanism for baryon number transfer. Outside the diffractive region, the contribution of Δ^{++} products to the inclusive net proton spectrum is large and roughly uniform in x_F. Thus, a large part of leading protons selected in Ch. 3 originates from Δ^{++} decays. All of the above suggests that baryonic resonances exert a non-negligible influence on phenomena discussed in Chapters 2 and 3.

Additionally, basic features of inclusive proton transverse momentum behaviour (like a weak $<p_T>$ vs. x_F dependence) are reproduced by protons originating from Δ^{++} decays.

4.5   Inclusive pion production

The second step of this study is to estimate the contribution of Δ^{++}, ρ^0, and ρ^+ resonances to inclusive π^+ production. With this aim, the simulated distributions of positive pions originating from decays of these three excited states are compared to inclusive spectra of π^+ produced in p+p reactions. The three resonances are taken together. Note that in the presented plots, the resulting summed resonance contribution is referred to as "$\Delta, \rho \rightarrow \pi^+$".

Fig. 34a shows the inclusive longitudinal π^+ spectrum in p+p reactions, compared to the corresponding distribution obtained for products of Δ^{++} and ρ decays. The two distributions are strikingly similar. The steepness of the experimental pion spectrum is very well reproduced by decays of the three resonances. Thus, the relative contribution of Δ^{++} and ρ decays is practically flat in the considered x_F range. These decays can be held responsible for about one third of all produced π^+.
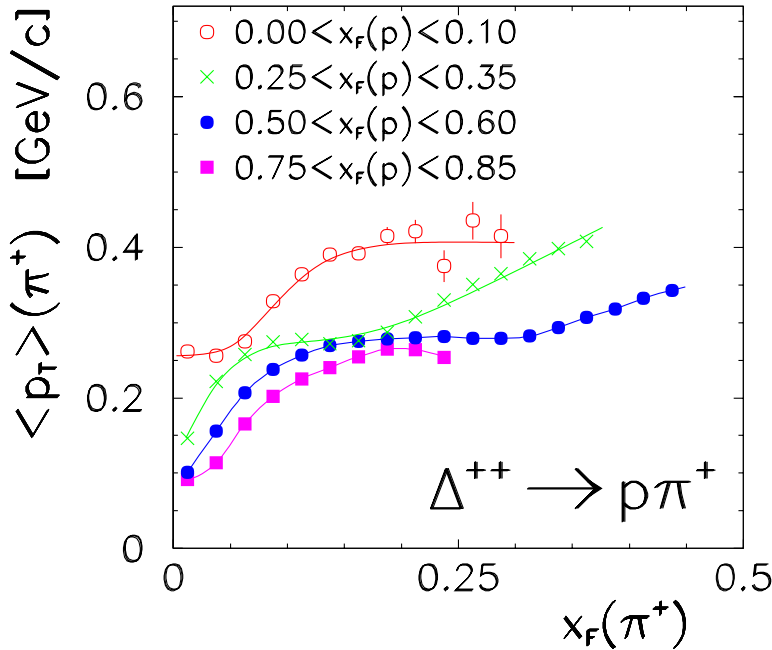
Figure 35: Simulated positive pion $<p_T>$ vs. x_F dependence, taken for different $x_F(p)$ selections. The triggered proton and the pion originate from the decay of the same parent Δ^{++} resonance.
Note the large statistical errors of the simulation at $x_F(\pi^+) \approx 0.25$, for the most central $x_F(p)$ sample.

The experimental $<p_T>$ vs. x_F dependence of positive pions is shown in Fig. 34b. Similarly to what has been shown in Ch. 3 for $\pi^+ + \pi^-$, the $<p_T>$ values display a characteristic increase with x_F. A similar increase is apparent for products of Δ^{++} and ρ decays, although the effect is visibly smaller.

Invariant p_T spectra are presented in Fig. 34c. The p_T distribution of inclusive pions, integrated over $0 < x_F < 0.5$, is similar to that of resonance products. Thus, the relative resonance contribution is not confined to any specific p_T region. On the contrary, it remains sizeable in the whole considered p_T range. As it follows from discussions made in Sections 4.3 and 4.4, results shown in Figs 34b-c are to some extent assumption-dependent. More precise experimental information is needed to provide fully solid estimates. On the other hand, the result shown in Fig. 34c is similar to what was obtained in studies of π^- production from mesonic resonances, in $\pi^+ + p$ collisions at 16 GeV/c [30]. Note that the study presented therein was made using completely different methods.

Thus, the simulated contribution of Δ^{++} and ρ decays to inclusive π^+ spectra in p+p reactions is not confined to any specific region of phase-space. Their relative contribution is flat in x_F. It appears sizeable in the whole considered p_T range. It seems therefore clear that resonance decays play a key role in building up the shape of inclusive pion spectra.

Additionally, the increase of $<p_T>$ with x_F observed for inclusive pions is qualitatively reproduced by pions originating from resonance decays.

4.6   Correlations

The last step of this study is to analyse the role played by resonance decays in the internal correlations observed in p+p events (Ch. 3). Specifically, one of the three observed patterns is considered: the dependence of pion $<p_T>$ values on x_F of the leading proton, denoted $x_F(p)$. The experimental results were shown in Fig. 26c.

The present analysis is made in a simple way, roughly analogous to what was made for the experimental p+p sample. From the full Monte-Carlo sample of $\Delta^{++} \to p\pi^+$ decays generated as described in Sec. 4.3, sub-samples are selected. These sub-samples are characterised by the x_F of the daughter proton. In each of these sub-samples, the $<p_T>$ vs. x_F dependence of the daughter pion is studied. This procedure is obviously not *fully* analogous to the *leading* (projectile component) proton selection applied for real p+p events in Ch. 3. It just provides a way to verify whether the observed behaviour of p+p data may be connected with the presence of the Δ^{++} resonance.

The results of the study are given in Fig. 35. The simulated $<p_T>$ vs. x_F dependence of the daughter π^+ shows a set of complex patterns as function of $x_F(p)$. However, the main trend is an

increase of pion $<p_T>$ values with decreasing x_F of the proton. A similar overall trend was observed for real p+p events. This indicates that the $\Delta^{++} \to p\pi^+$ decay indeed plays a role in the effect seen in the data.

The analysis presented here has obvious limitations. Our simple Monte-Carlo procedure can be used to investigate correlations resulting from the presence of the single $\Delta^{++} \to p\pi^+$ decay, but not to reproduce a whole p+p event. This makes more quantitative correlation studies quite intricate. However, already the result shown in Fig. 35 suggests that resonance decays have their part in the observed dependencies between charged pion production and baryon number transfer.

4.7   Summary

A study of connections between resonance production and phenomena described in Chapters 2 and 3 has been made for p+p reactions. The effects of baryon number transfer, positive pion production, and their mutual dependencies have been considered. The role played by $\Delta^{++}(1232)$, $\rho^0(770)$, and $\rho^+(770)$ resonances has been investigated.

The Δ^{++} and ρ decays appear as an important source of positive pion production. They can be held responsible for about one third of all produced π^+. The simulated x_F and p_T spectra of resonance products are similar to these of inclusively produced pions. Thus, the relative resonance contribution to inclusive spectra is not confined to any specific phase-space region, but remains sizeable in all the considered x_F and p_T range. Similarly to inclusive pions, the products of Δ^{++} and ρ decays display a characteristic increase of $<p_T>$ with x_F. Although to some extent dependent on the details of the applied Monte-Carlo method (Sec. 4.3), the above results are not surprising in the context of earlier studies [30].

What is more, a roughly similar result is obtained for net proton production. The $\Delta^{++} \to p\pi^+$ decay appears to give a sizeable contribution to longitudinal net proton spectra. Outside the diffractive region, this contribution is roughly uniform in x_F. The Δ^{++} decay provides a natural baryon number transfer mechanism, which gives an important contribution to the total "momentum loss" observed in p+p reactions between the projectile and the final state proton. Additionally, the main features of inclusive proton transverse momentum behaviour (weak $<p_T>$ vs. x_F dependence) are reproduced by simulated Δ^{++} daughters. Finally, the Δ^{++} decay appears to play a role in at least some of the observed correlations between charged pion production and baryon number transfer.

Due to limited experimental information, the analysis made in this Chapter has been constrained to *low-lying* hadronic excitations. A possible influence of higher excited states has to be considered. For instance, the review [4] points at a possible production of higher baryonic states. At the same time, preliminary NA49 results suggest the presence of N^{*+} peaks in the three-body $p\pi^+\pi^-$ invariant mass spectrum [42]. It can be expected that three- or multibody decays of such higher states will provide an even more efficient baryon number transfer mechanism than that observed for the Δ^{++} decay. To quote one among many possibilities, cascading decays of the type $N^* \to \Delta\pi \to p\pi\pi$ are possible [16], giving a higher "momentum loss" than the $\Delta \to p\pi$ decay alone. Thus, the role played by higher baryonic resonances in the overall process of transfer of baryon number from the projectile to the final state proton may be important. It requires further investigation. The same is obviously valid for their role in charged pion production, and in its dependence on baryon number transfer.

The results presented in this Chapter suggest that hadronic resonances play an important role in the considered effects. It seems difficult to understand the mechanisms underlying the phenomena observed in p+p reactions without studying this role in detail. In the context of comparative studies made in this thesis, this should have consequences not only for p+p, but also for p+A and A+A collisions. We will come back to this problem in the following Chapter.

Chapter 5. Summary, Remarks, and Questions

This Chapter contains a short summary of main results obtained in this thesis. A few remarks are made and a few general conclusions are proposed. Finally, some additional speculations are made.

5.1   Summary

A comparative study of p+p, p+Pb, and Pb+Pb reactions has been presented. It has been focussed on phenomena of baryon number transfer and charged pion production. The three collision types have been studied using the same experimental apparatus. Data on identified particles have been shown in a wide region of available phase-space. Inclusive p+p interactions, internal correlations in p+p events, and the centrality dependence of p+Pb and Pb+Pb collisions have been analyzed. Additionally, the role of resonance production in some of the observed phenomena has been investigated.

   The main results of this study can be summarized as follows.

(1) A two-component picture of net proton spectra appears consistent with the data on several elementary reactions: p+p, π^++p, and π^-+p. These spectra can be separated into two components, attributed to the projectile and target. Thus, the projectile component of net proton spectrum in p+p collisions can be isolated using pion beams. For π^++p and π^-+p reactions, non-zero projectile components of net proton spectra are present. They can be attributed to projectile-dependent, asymmetric $B\bar{B}$ pair production.

(2) Applied to p+Pb and Pb+Pb collisions, the two-component picture results in a common scheme of baryon number transfer in elementary and nuclear reactions. With increasing number of elementary subcollisions suffered by the projectile, the projectile baryon number is strongly "pushed" towards the backward hemisphere. In this common pattern, most central Pb+Pb collisions occupy a medium position between p+p and central p+Pb reactions. Outside the diffractive region, the above baryon stopping effect is similar for final state protons and neutrons.

(3) Charged pion production in p+p events is correlated to baryon number transfer. The forward hemisphere pion multiplicity increases with decreasing x_F of the final state proton, similarly to [27]. The shape of pion dN/dx_F spectra is roughly invariant on $x_F(p)$. Pion $<p_T>$ values increase with decreasing $x_F(p)$.

(4) The common baryon stopping scheme (2) and the correlation (3) can be used to formulate a prediction for the centrality dependence of p+A and A+A reactions. Qualitatively, this prediction is fulfilled by charged pion production in Pb+Pb and intermediate p+Pb collisions. This indicates that already in elementary p+p events, dynamical features exist which can at least partially explain phenomena observed in nuclear reactions. Therefore, a change observed relative to *inclusive* p+p collisions does not automatically indicate any "new" mechanism of pion production.

(5) The same prediction is not sufficient to describe the most central p+Pb reactions. The experimental data show an unpredicted saturation of forward hemisphere pion multiplicities and a depletion of pion dN/dx_F spectra.

(6) Hadronic resonances play a very important role in charged pion production in p+p collisions. Monte-Carlo studies of Δ^{++}, ρ^0, and ρ^+ decays indicate that their contribution to inclusive π^+ spectra is not confined to any specific region of phase-space. This is similar to results shown in [30].

(7) Resonance production influences also the behaviour of final state protons. Outside the diffractive region in p+p reactions, the $\Delta^{++} \to p\pi^+$ decay gives a large, flattish contribution to longitudinal net proton spectra. It plays a significant role in the overall baryon number transfer process, and in at least some of the correlations listed in (3).

5.2 Remarks

Here, a few remarks are made, which aim to point out some general aspects of the results listed in items (1)-(7).

Primo, item (1) provides insight into the role played by the valence structure of incoming hadrons in some observed phenomena. The valence structures of projectile and target are clearly reflected by the process of baryon number transfer: they define the projectile and target components of net proton spectra. Following the discussion made in Ch. 2, they also find their reflection in the production of baryon-antibaryon pairs.

Secundo, items (2)-(5) provide information about similarities and differences between elementary and nuclear reactions. In the phenomena of baryon number transfer and pion production in p+p, p+A and A+A collisions, a number of common points can be identified. The common baryon stopping scheme (2) suggests a similar mechanism of baryon number transfer in the three collision types. The success of prediction (4) suggests that effects observed in p+A and A+A reactions contain a significant "elementary ingredient". More generally, it also indicates that several features of pion production, like the dependence of various observables on $x_F(p)$, are similar in elementary and nuclear collisions.

However, differences are visible on top of similarities. Data on central p+Pb reactions suggest the presence of additional phenomena, characteristic to multiple collisions of the projectile inside the nuclear target. Following the speculations made in Ch. 3, the projectile energy loss in subsequent subcollisions could be held responsible for the observed effects. The consequences of the above observations for A+A reactions need further clarification.

The analysis of internal correlations in p+p events plays a key role in the above problems. It constitutes a starting point to isolate similarities and differences between p+p, p+A and A+A reactions. Moreover, impact parameter control in p+A collisions gives a way to study the above differences in extreme centrality conditions. Experimentally, this possibility is not available in other reactions.

Tertio, items (6) and (7) demonstrate the importance of resonance decays in the observed phenomena. Their importance in pion production in elementary collisions has been known [30, 31]. However, it appears that they also play a significant role in baryon number transfer effects, and in at least some of the observed correlations. In the context of the above similarities between elementary and nuclear reactions, it can be expected that their role in phenomena occuring in p+A and A+A collisions will also be important. It should not be forgotten that the two quoted references and the present study give only "lower limit estimates" of their importance. These studies are restricted to a finite number of low-lying excited states, and other excitations can always be considered [4]. As has been said, the presence of higher baryonic states suggested by preliminary NA49 data [42] will further increase their importance in baryon number transfer processes. Their role in pion production is already known to be dominant. Thus, the question to which other phenomena does their influence extend seems more than indicated.

Following the above remarks, let us propose three more general conclusions to complete the summary made in the previous Section, and to provide partial answers to the questions formulated in Sec. 1.2:

a) The valence quark content of incoming hadrons defines the two-component structure of the baryon number transfer process. Also, it is reflected in the production of $B\bar{B}$ pairs.

b) Baryon number transfer and pion production display a number of similarities between elementary and nuclear collisions. These similarities may remain "hidden" if the usual comparison between centrality-selected nuclear and inclusive elementary reactions is made. They can be isolated by studies of internal correlations in elementary events. Differences are also observed. They are clearly visible in central p+A data. Possible implications for A+A reactions need to be clarified.

c) Hadronic resonance decays play an important role in the observed processes. Their full influence on the hadronic collision dynamics needs to be further investigated.

5.3 Questions

In principle, the above Section closes the study of baryon number transfer and charged pion production made in this thesis. However, both phenomena cannot be analyzed in isolation from other effects observed in hadronic collisions. Confronted with these effects, the information presented above inspires many further speculations. Furthermore, additional speculations could be made about the subjects presented in the previous Chapters. Thus, many questions can be asked. The first three which come to mind are presented below:

- The common baryon stopping scheme from Ch. 2 gives a picture of the projectile baryon number being "pushed backwards" with increasing centrality of the p+A/A+A collision. As can be seen from Fig. 21, this results in an increase of baryon densities at $x_F = 0$. It has been shown that the overall baryon stopping effect is similar for final state protons and neutrons. It could therefore be expected that a similar effect will also be observed e.g. for Λ baryons. One can therefore ask the question: what is the connection between the phenomena studied in this thesis, and the enhancement of strange baryon mid-rapidity production, observed both in A+A and p+A reactions [43]? Are these two independent problems, or is baryon stopping one of the elements building up the above enhancement?

- Results on charged particle densities $(dN_{ch}/d\eta)$ at pseudorapidity $\eta = 0$ have recently become available for Au+Au collisions at $\sqrt{s_{N+N}} = 130$ GeV [44]. A smooth increase of charged particle density per participant pair is observed with increasing centrality of the collision. At the same time, the quoted paper reports $\bar{p}/p$ ratios well below unity. This indicates that the central region is not baryon-free, i.e. that a transfer of baryon number down to $x_F = 0$ still occurs at these much higher energies. Altogether, this situation shows similarities to that presented in Chapters 2 and 3, where a smooth increase of forward hemisphere pion yield and a baryon stopping effect were observed. The obvious questions are: to what extent are these two situations similar? To what extent can the observed increase of $dN_{ch}/d\eta$ be regarded as direct consequence of correlations between charged particle production and baryon number transfer, present already in p+p events?

- Finally, a general question should be asked about the meaning of results presented in Ch. 4. Resonance excitations play an important role in baryon number transfer and pion production in p+p collisions. What is their role in the smooth evolution of baryon stopping, observed in Ch. 2 for p+p, p+A and A+A reactions? What is their role in the increase of pion production, seen in Ch. 3 for nuclear collisions? Could it be that multiple collisions of the projectile will result in enhanced production of higher baryonic excitations which, as has been said, will give higher "momentum loss" of the final state proton? What is the evolution of baryonic/mesonic resonance production with centrality? How will it affect pion yields and spectra? Altogether, is the problem of differences observed between p+p and p+A/A+A reactions independent or connected with that of resonance production?

The above questions have been formulated with two aims: in order to inspire possible further subjects of experimental investigation, and to demonstrate how "cross-connected" various phenomena in hadronic reactions may be. This cross-connected character of soft hadronic physics has been the inspiration for the comparative analysis made in this thesis. It is the sincere hope of the author that this analysis might give some help in further studies of this so difficult and therefore so exciting subject.

Appendix A. Study of the NA49 TPC's Using Radioactive Krypton

This Appendix contains a summary of the study of NA49 Time Projection Chambers (TPC) using the radiative decay of the ^{83}Kr isotope. First the motivation underlying this study is explained. Then the idea of the method, the data analysis, and the study of achieved precision are described. Finally, principal results are presented.

Our results are important for any existing or future TPC experiment. For that reason, their description is not limited to the performance of the krypton calibration method (Ch. 1). It also extends to such problems as systematics of TPC response over the chamber, comparisons to other calibration methods, etc.

It should be underlined that this Appendix summarizes the contribution of this thesis to the overall performance of the NA49 detector. Thus, it is focussed on complicated technical problems. The description presented here is a continuation of the general discussion of NA49 particle identification performance (Ch. 1). However, it is also largely based on several references. The most important is the detailed description of operation and design of the NA49 detector [13]. Moreover, the main parameters of NA49 TPC chambers are summarized in [45]. The differentiation between High Resolution and Standard Resolution (HR/SR) sectors of the MTPC chambers can be found therein. Finally, a short summary of NA49 TPC numbering conventions can be found in [46].

With the exception of the Monte-Carlo spectrum shown in Fig. 38b, all the results presented here have been obtained within the framework of this thesis. The above Monte-Carlo spectrum comes from [13]. The experimental results are based on krypton data taken during the 1996 SPS running period.

A.1   Motivation

One of the principal functions of the NA49 Time Projection Chambers is particle identification via dE/dx. In order to allow a precise dE/dx measurement, a very precise knowledge of the detector response (gain) is needed. This detector gain is subject to local variations, consisting of both gas gain and electronics response fluctuations. The aim of using radioactive krypton is to study the behaviour of detector gain in the various TPC's.

The method has been developed by the ALEPH collaboration [47] and has been used by the DELPHI experiment [48] for applications similar to the ones described here. It consists in injection of the radioactive ^{83}Kr isotope into the detector gas. The isotope decay spectrum being known very well, it is possible to investigate the TPC response by comparing the charge spectra seen by the readout electronics in various parts of the chamber. With sufficient statistics of krypton data (a sufficient number of radiative decays registered by the TPC system), a high-granularity "map" of TPC gain becomes available. This has several applications, three of which will be discussed here. These are:

1. a detailed study of electronics and gas gain variations over a given TPC chamber.
2. a precise calibration of the above gain variations, resulting in 1% accuracy in knowledge of detector response.
3. an efficient cross-check of other calibration methods.

The total NA49 TPC system comprises 182,000 pads, each connected to an electronics channel. The above method allows a study at a single chip level, one chip being connected to 16 neighbouring pads belonging to the same pad row. Additionally, the main systematics of gain variations inside the chips can be analysed. All these possibilities will be exploited in the following Sections.
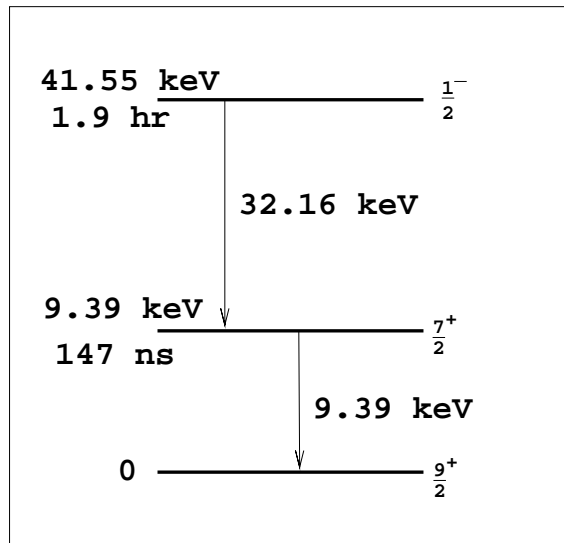
Figure 36: Diagram of deexcitation of the $^{83}_{36}$Kr isotope.

A.2   The method

This Section contains a description of the physics basis of the method and of its application to NA49. An estimate of accuracy of the calibration is included.

A.2.1   General remarks

The method consists in placing a radioactive $^{83}_{37}$Rb source[1] in a small volume by-pass of the gas recirculation system of the NA49 TPC's. The radioactive krypton gas emanating from the source is injected into the sensitive volume of the chamber, where it decays down from its unstable excited state. The decay gives a specific spectrum of energy deposit in the chamber, which results in a given charge deposit spectrum. The charge deposit is then registered by the readout system in a given part of the TPC (data are taken with a clock trigger). Due to differences in local detector gain, the charge spectra registered in different TPC regions have different x scales. If the local gain is higher, the registered charge spectrum is wider, and vice-versa. Thus, the relative local gain can be measured by comparing these spectra.

A.2.2   Physics of krypton decay in a gas chamber environment

The description made in this Section is to a large extent based on [49, 50].

The radioactive krypton gas $^{83}_{36}$Kr, obtained from the $^{83}_{37}$Rb source by electron capture (EC), finds itself mostly in an unstable isomeric state of 41.6 keV excitation energy (half life of 1.9 hr). The diagram of deexcitation of the $^{83}_{36}$Kr isotope is shown in Fig. 36. As illustrated in the Figure, the isomeric state decays down to the ground state through an intermediate excited state of 9.4 keV energy (half life of 147 ns). We have therefore in fact *two* nuclear decays (with 32.2 and 9.4 keV transition energy). These are quite complex processes (Fig. 37) which we will discuss in more detail.

---

[1]Source produced at ISOLDE Isotope Separator, CERN.
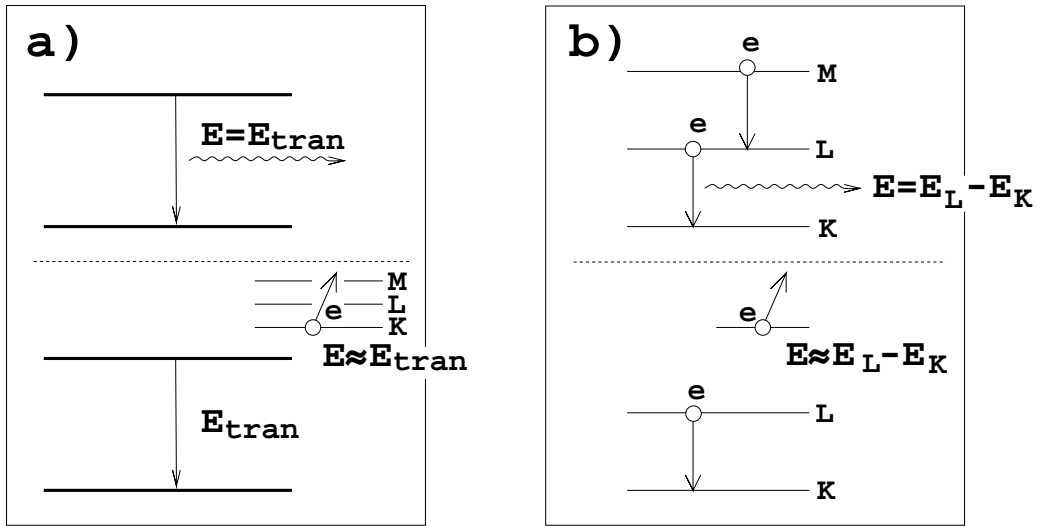
Figure 37: Schematic illustration of the subsequent phases taking place in the two nuclear decays: **a)** the *nuclear transition*: proceeds either through "direct" gamma emission from the nucleus (upper panel), or through internal conversion - nuclear transition energy E_{tran} is transmitted to an electron belonging to one of lower atomic shells: K,L,M... (lower panel).
b) the *atomic deexcitations:* atomic shells emptied by internal conversion are filled by electrons from higher levels. These higher levels are then filled as well, and so on. The energy difference is emitted through fluorescence, i.e. X-ray emission (upper panel), and by Auger transition, i.e. electron emission from an external orbit (lower panel). Practically, fluorescence fills only the K shell. Auger transitions fill all the shells.

The 32.2 keV transition is almost entirely dominated by internal conversion (IC), which is then followed by atomic deexcitations (photon X-ray emission and Auger transitions). The outcome of this process is a number of electrons (with well defined energies not exceeding 32.2 keV), plus possibly one X-ray photon (energy between 12.6 and 14.3 keV).

The 9.4 keV transition is also dominated by internal conversion, but a 9.4 keV gamma emission is also observed with a relative probability of 4.9%. The subsequent atomic deexcitations are Auger transitions. Again, the final outcome of the process are electrons with given energies, and possibly one 9.4 keV photon.

As far as the method described here is concerned, the basic feature of this two-step nuclear decay is the resulting energy deposit in a gas chamber environment. In order to understand the way it comes out, the following facts are to be remembered:

1. the photons possibly emitted in both transitions (energy below 15 keV) interact with the gas molecules via the photo-electric effect. The radiation length being of an order of 30 cm, this gives free electrons in the TPC gas volume.

2. all the free electrons which have appeared in the gas (by IC, Auger transitions, or photo-electric effect), ionise its molecules. The electron energy being relatively low (below 32.2 keV), the resulting "ionization tracks" are short (below 2 cm).

3. what is registered by the TPC readout system are electron clusters coming from the ionization. As electrons coming from IC an Auger transitions appear directly at the decay site, the short ionization tracks will give in fact a single electron cluster. A separate cluster, though, will appear as a result of each of the photon emissions.

4. finally, the half life of the intermediate nuclear state (147 ns) is so short that the two electron clusters appearing at the decay site as result of the two nuclear transitions can in fact be regarded as a single cluster.

Summing up what has been said in items 1-4, the result of a single deexcitation of the unstable 41.6 keV state down to the ground state of the $^{83}_{36}$Kr isotope will be the following:
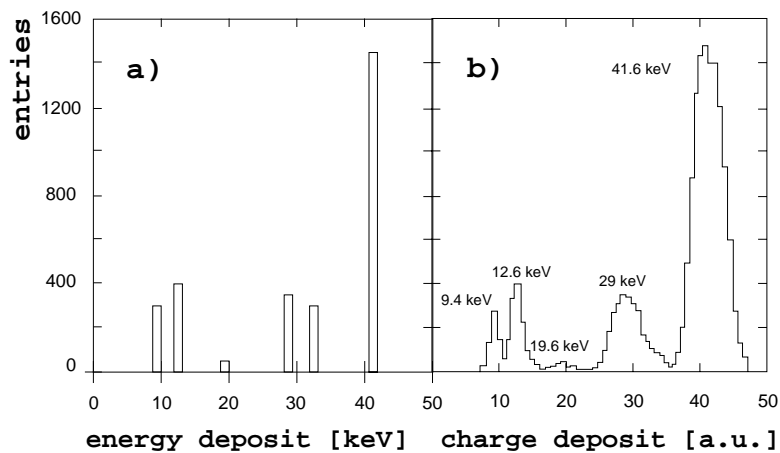
Figure 38: **a)** Energy deposit spectrum resulting from $^{83}_{36}$Kr decay. The plot is a simplified illustration; all X-ray peaks in the region 12.6-14.3 keV are shown as one single peak. **b)** Corresponding charge deposit spectrum after the inclusion of basic detector effects. Distinguishable peaks are marked in the plot.
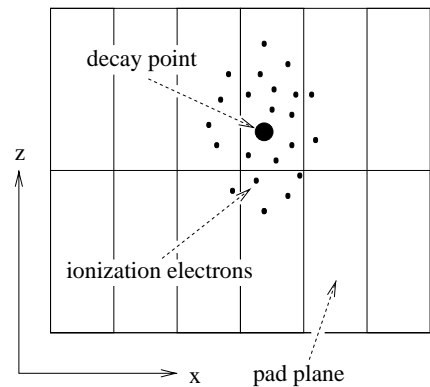
Figure 39: Schematic picture of a krypton cluster over the TPC pad plane.

- a single electron cluster at the decay site, corresponding to an energy deposit of up to 41.6 keV;

- possibly, one or two more electron clusters resulting from photon emission, located at a large distance (of an order of 30 cm) from the decay site. The corresponding energy deposit varies between 9.4 and 14.3 keV.

What we get therefore is a characteristic spectrum of energy deposit, illustrated in Fig. 38a. After taking account of basic detector effects (drift, diffusion, and others [51]), we come to the smeared charge spectrum seen by the TPC readout system. This spectrum is shown in Fig. 38b, as obtained from a simple Monte-Carlo. Although the various peaks have now a sizeable width, most of them are well distinguishable. Note that the main peak of the charge spectrum corresponds to the energy deposit of 41.6 keV.

A.2.3 Data analysis and calibration procedure

This Section contains a short description of how the krypton data are analyzed and how the calibration procedure looks like. The various kinds of calibration constants are defined here, and the purposes of their calculation are presented.

Raw Data Analysis

The first step of the analysis of krypton data is *cluster-finding*, i.e. the reconstruction of electron clusters coming from krypton decays, called "krypton clusters" from now on. There is one principal difference between krypton clusters and clusters coming from physics data (i.e. from charged particles passing through the gas volume of the chamber). Particle clusters are always defined as collected on a given pad row: a track passing over n pad rows is supposed to give n electron clusters. The krypton clusters have to be defined in a different way: the electrons forming a given cluster can be found not on a single pad row, but also on neighbouring rows (a schematic example of a krypton cluster is shown in Fig. 39).

Therefore, a special cluster-finder algorithm is used in order to reconstruct the electron clusters in raw krypton data. Instead of looking for electrons on a single pad row, it also looks for them on the neighbouring rows. For every cluster found, several parameters are recorded, including the total charge, the spatial extent, the position on the x-z plane[2], the value of the maximum ADC count, and

---

[2]Note that the data do not contain a determination of the y coordinate (time direction), because the decays are not in time with the data acquisition trigger.

others.

After cluster reconstruction, the krypton cluster charge spectra are available for analysis. An example of such a spectrum is shown in Fig. 40. The Figure presents a total charge spectrum from a single MTPC sector. As one can easily see, this spectrum is much more distorted than the one coming from the Monte-Carlo (Fig. 38b). This is to be expected, as in addition to some complicated detector effects not included in the Monte-Carlo, a very important contribution to the distortion comes from gain variations within the sector. To correct for these gain variations is the main aim of this study.

Calibration Procedure

The krypton calibration is performed for each TPC separately. The procedure consists of two steps:

1) Chip calibration: for every readout chip in the chamber, a separate charge spectrum histogram is produced. Examples of such spectra are shown in Fig. 41. These histograms are fitted *versus* a given reference spectrum. The fitting algorithm works as follows: the fit parameter is the multiplicative variable k_i^{raw}, by which the x-axis of the spectrum should be shrunk or stretched in order to match the reference (i.e. to give a minimum χ^2 value). The value of k_i^{raw} will be called below the *raw calibration constant*. It is inversely proportional to the gain of a given chip.

The aim of the calibration procedure is to take out the relative gain variations *inside* TPC sectors, but not to correct for inter-sector gain differences[3]. This is why after the calculation described above, all the raw calibration constants belonging to a given sector are *rescaled* to give an average equal to 1. This gives us the final *chip calibration constants* k_i. Thus, when the measured raw data pad charge is multiplied by the corresponding chip calibration constant, i.e.:

$$q_i^{\mathrm{corrected}} = k_i \cdot q_i^{\mathrm{measured}}$$

the obtained charge value ($q_i^{\mathrm{corrected}}$) is corrected for relative gain differences between the chips of a given sector.

2) Linear chip correction: after the raw data are calibrated as described above, another problem comes in. As will be discussed in detail in Sec. A.3.2, a systematic change in gain is present for the 16 pads *belonging to the same chip*. This problem requires a dedicated analysis, which is performed in the following way: the surface of the sector pad plane is divided into "linear slices" as shown in Fig. 42, and for each "slice" a charge histogram is produced. Then calibration constants are calculated in the same way as described in step **1)**. These constants will be referred to as *slice constants*.

Fig. 43 presents the behaviour of slice constants in a single MTPC sector. As it is visible in the Figure, the constants (and thus, also the gain) show a systematic dependence on pad position inside the chip. This dependence can be roughly approximated by a linear slope. Therefore an appropriate linear correction is applied to the raw pad charge, on top of the chip calibration. The mechanism of this *linear chip correction* will be discussed in more detail in Sec. A.3.2. Here we shall only state that it is based on the slopes shown in Fig. 43, averaged over many sectors.

It should be underlined that the calibration procedure presented in **1)** and **2)** takes care of relative gain variations between chips of a given TPC sector, and of the *systematic* gain variations inside the chips. What remains uncalibrated are the non-systematic gain fluctuations that can be expected inside the chips. The magnitude of these variations will be estimated in Sec. A.3.2.

---

[3]In principle, the above raw calibration constants could be used to establish also gain differences *between* sectors. However, we allow for a possibility of changes of sector gain with time. Such changes cannot be precisely monitored with krypton calibration runs (taken typically before and after each SPS running period of 6-8 weeks). Therefore, an independent method, based on physics data, is used to calibrate gain differences between sectors and between TPC's. The same method is used to follow their time evolution.
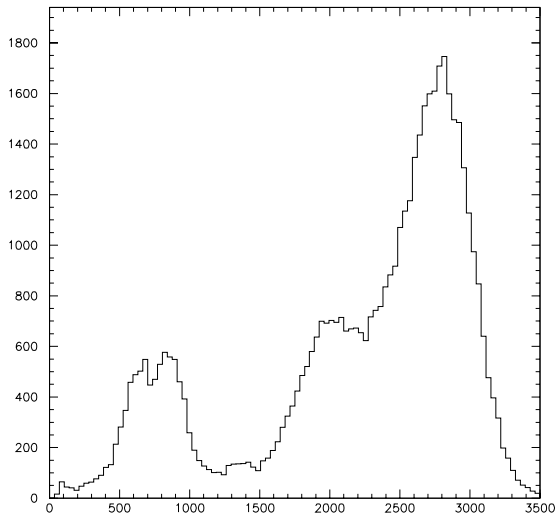
Figure 40: Uncalibrated cluster charge spectrum from one MTPC-L sector. The charge is measured in ADC units.
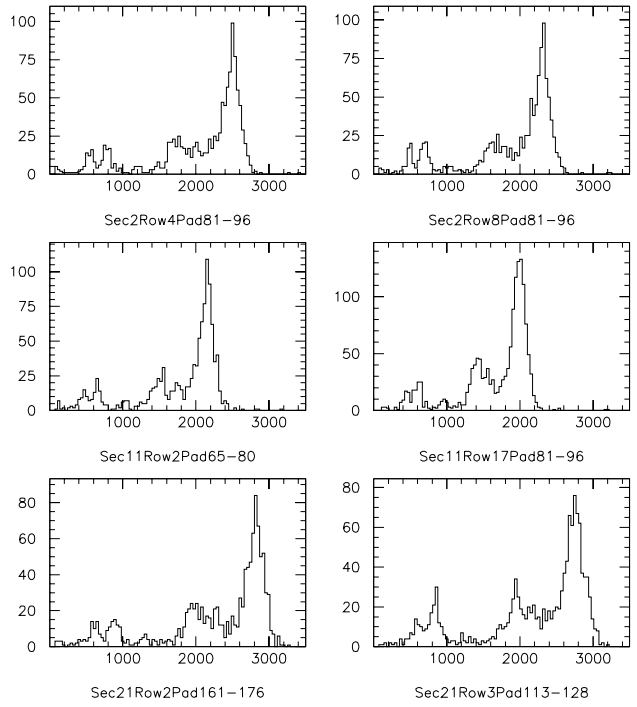

Figure 41: Krypton cluster charge spectra produced for single MTPC-L readout chips. The charge is measured in ADC units.
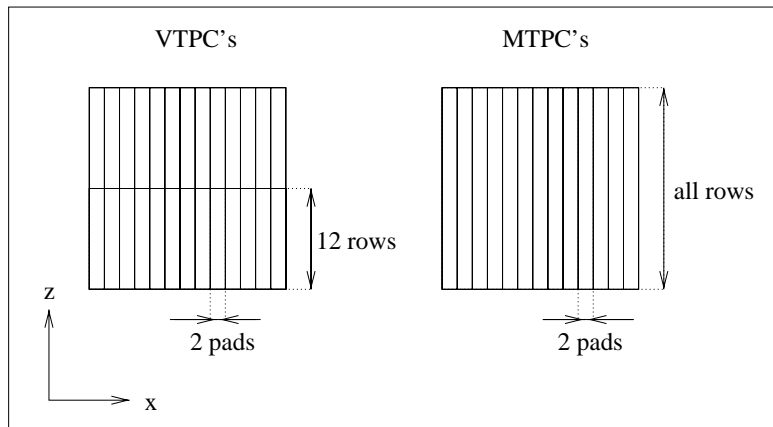

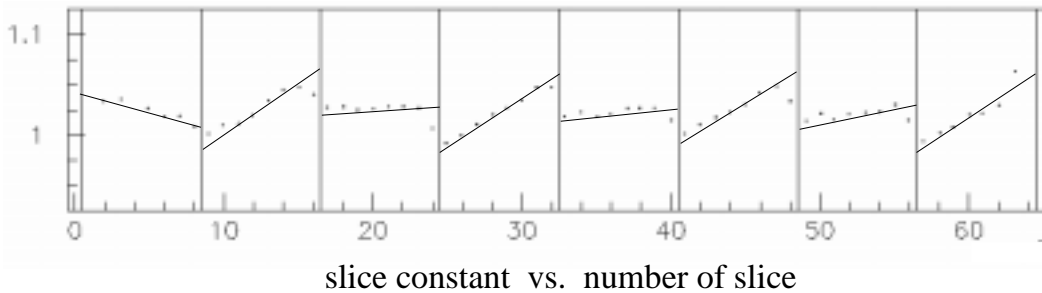Figure 42: "Slicing" of sector pad planes for the two kinds of TPC's.

slice constant vs. number of slice

Figure 43: Dependence of slice constants on their position along the pad row for a single sector of MTPC-L. The constants are plotted *versus* the number of the constant in the row, each constant corresponding to two pads. Chip limits (vertical lines) and roughly evaluated linear slopes are also shown in the plot.

59
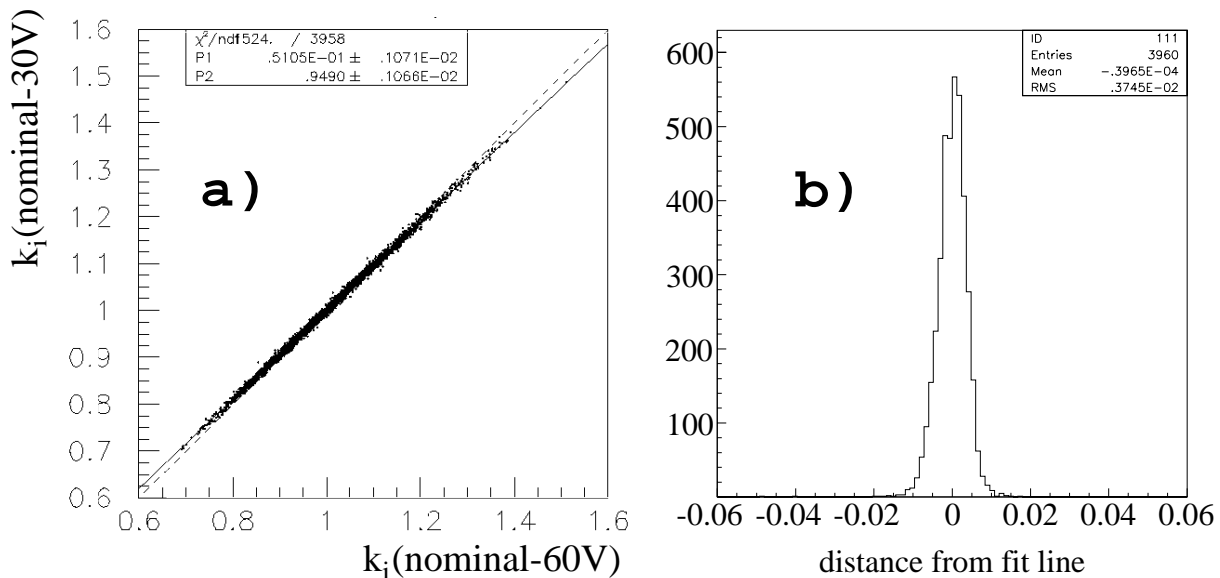
Figure 44: Comparison of two sets of MTPC-L chip calibration constants: **a)** constants obtained at nominal HV setting lowered by 30 V, plotted *versus* the ones obtained at nominal HV setting lowered by 60 V, together with the linear fit result (solid) and the $y = x$ line (dashed), and **b)** the distribution of distance of the data points from the fit line.

Sector Constants

In order to complete the description of krypton data analysis, we should still mention the *sector calibration constants*. As has been stated above, the aim of the krypton calibration procedure is to take out only gain fluctuations inside sectors of a given TPC, and not to perform any correction of inter-sector gain variations. In spite of this, some study of gain differences between sectors has been accomplished and will be presented in this Appendix. The quantity used for this study are sector calibration constants, obtained by averaging the raw chip constants over the sector:

$$k_{\text{sector}} = < k_i^{\text{raw}} > |_{\text{sector}}$$

A.2.4 Precision of the method

As has been said, a precise knowledge of detector gain is crucial for the overall particle identification performance of the NA49 TPC system. For that reason, it is very important to know the accuracy of measurement of the calibration constants defined in Sec. A.2.3. A dedicated study has been made in order to estimate this accuracy. The results of this study are presented in this Section.

As a first step of the study, two MTPC-L krypton runs (so: two independent data samples) have been processed, and two sets of chip calibration constants have been obtained. The two runs were taken at different High Voltage (HV) settings: at nominal voltage[4] lowered by 30 and by 60 V. This way, a comparison between the two sets of constants will provide us with information about **1)** the statistical precision of chip constants and **2)** their possible systematic dependence on HV setting. Specifically, if the precision is *ideal*, corresponding chip constants will be exactly *equal*.

Fig. 44a shows a comparison of the two sets of constants. Note that a linear fit is made through the data points. A very strong correlation is apparent in the Figure, and the obtained data points lie close to the $y = x$ line corresponding to an ideal precision. Nevertheless, two effects are visible:

- the data points show a certain dispersion around fit line;
- the fit line deviates from $y = x$.

The first effect can be attributed to statistical fluctuations of the constants. It can be estimated from the distribution of the data points around the fit line, shown in Fig. 44b. This distribution has

---

[4]The nominal High Voltage settings in different chambers are of the order of 1 kV.
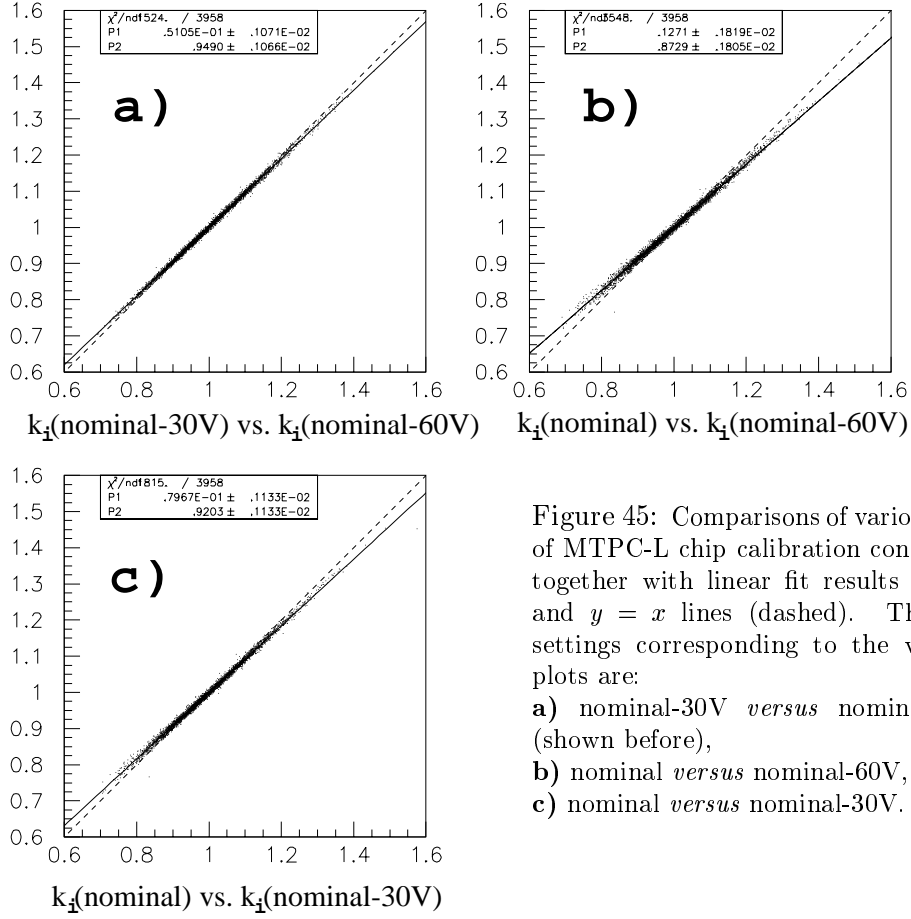
Figure 45: Comparisons of various sets of MTPC-L chip calibration constants, together with linear fit results (solid) and $y = x$ lines (dashed). The HV settings corresponding to the various plots are:
a) nominal-30V *versus* nominal-60V (shown before),
b) nominal *versus* nominal-60V,
c) nominal *versus* nominal-30V.

an RMS of about 0.4%. This value can be taken as a rough estimate of the statistical accuracy of the method.

The second effect has a systematic character. It could be explained by saturation of TPC readout electronics. This problem can be described as follows. The NA49 TPC readout is calibrated in a way to produce a maximum signal of 60 ADC counts for a minimum ionizing particle. Such a particle gives an energy deposit of about 6 keV per pad row in the MTPC chambers. On the other hand, a krypton cluster coming from a decay of 41.6 keV total energy will give a much bigger deposit, which will result in a maximum ADC signal far beyond the allowed range of 255 ADC counts. Signals beyond the allowed range being assigned a value of 255 ADC, the total charge of the cluster will be attenuated[5]. As this effect is more important for higher-charge clusters, it will result in a deformation of the charge spectrum, and in shifting the main peak position to the left. This leads to a larger value of the raw calibration constant k_i^{raw}, relative to an unsaturated sample; this effect is more important for higher gain spectra (lower k_i^{raw}). As the final constants k_i are rescaled to give an average equal to 1 over sector, what we expect is:

- for higher chip gain (lower k_i): k_i(saturated)$>$ k_i(unsaturated)

- for lower chip gain (higher k_i): k_i(saturated)$<$ k_i(unsaturated)

For two saturated samples, we expect the relative shift of the constants to increase with increasing difference in the fraction of saturated clusters. Our expectations are verified in Fig. 45. The Figure shows three comparisons of sets of k_i constants obtained from data samples coming from three MTPC-L krypton runs taken at three different HV settings: nominal voltage, nominal voltage lowered by 30 V, and lowered by 60 V. This gives three data samples, each containing a different fraction of saturated clusters (increasing with increasing voltage). The behaviour of the fitted linear slopes agrees with

---

[5]A quantitative evaluation of this effect requires taking the cluster size into account. Krypton clusters are bigger than charged particle clusters, so the magnitude of the effect will be diminished. Nevertheless, the effect is significant.
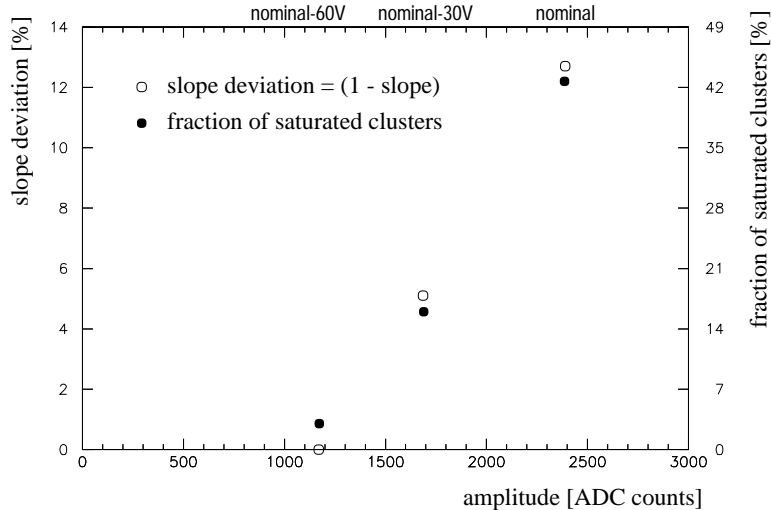
Figure 46: **Open symbols:** deviation of fitted slope from 1, shown as function of HV setting and of the corresponding amplitude. The amplitude is defined as average measured position of the main peak of the charge spectrum. For each of the three samples, the slope is fitted in relation to the lowest (nominal-60V) HV setting sample. **Full symbols:** fraction of saturated samples for a given HV setting, shown as function of the corresponding amplitude. Note: left and right scales are arbitrarily adjusted.

all the above expectations. This proves that the systematic effect discussed here is indeed caused by electronics saturation.

In order to follow this effect more quantitatively, the behaviour of the slopes fitted in Fig. 45 has been compared to that of the fraction of saturated clusters. This is shown in Fig. 46. As it is visible in the Figure, the deviation of the slope from 1 follows quite well the percentage of saturated clusters. We can deduce from the plot that the influence of saturation will be reasonably small for runs taken at lowest HV setting (i.e. at nominal voltage lowered by 60 V)[6].

We can therefore conclude that the systematic effect seen for different HV settings can be explained by saturation of the TPC readout electronics. The overall magnitude of this effect is relatively small and it will not have a serious influence on the calibration constants produced at lowest HV setting. For this reason, the calibration procedure described in Sec. A.2.3 will be based on krypton data taken at lowest HV setting.

A.3 The results

This Section presents the principal results of the study. First, the usefulness of the krypton method in verifying the quality of other calibration methods is demonstrated. Then, results of the analysis of gain variations in the NA49 TPC's are shown. Finally, the effects of applying the krypton calibration procedure are presented.

A.3.1 Cross-check of electronics pulser calibration

We present here the results of a study of consistency between the NA49 electronics pulser calibration and the krypton calibration methods. Krypton calibration provides here a unique possibility of cross-checking the pulser calibration quality. This is especially valuable as krypton decays constitute quite a similar "input" for the NA49 electronics as the charged particle tracks (in both cases, electron clusters are formed). This is not the case for pulser calibration, which on the other hand is practically much easier than the use of radioactive krypton.

---

[6]One should note that this influence will be different for MTPC's and VTPC's. For lowest HV setting runs, about 3% of the clusters are saturated in MTPC's, and about 13% in VTPC's. Even for VTPC's, however, the influence of saturation on the value of the constants is expected to be reasonably small.
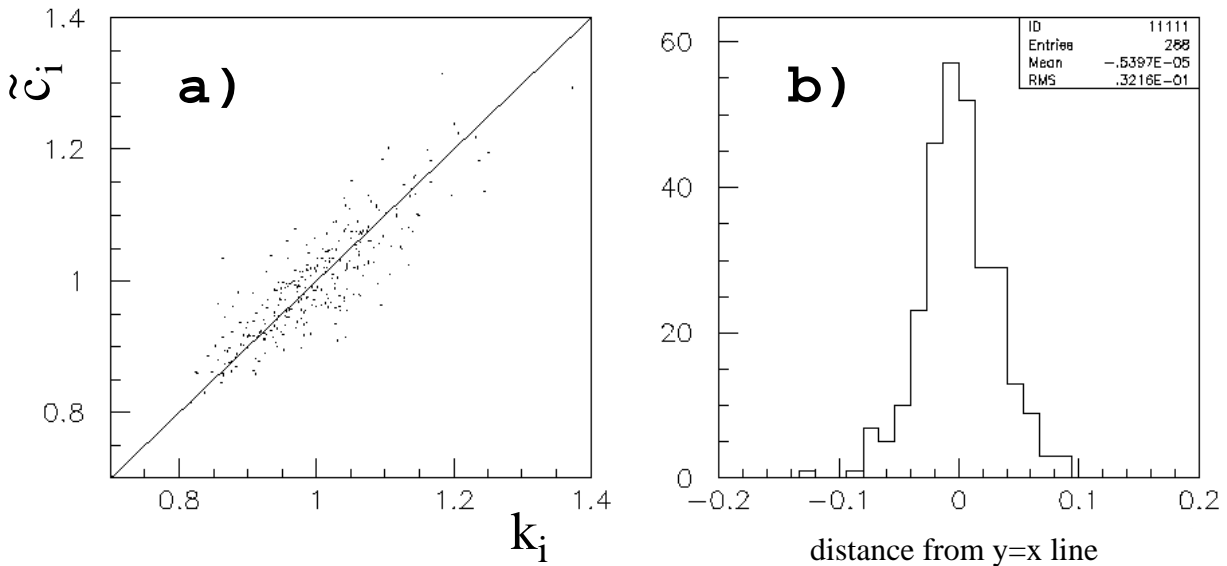
Figure 47: Comparison of VTPC-2 krypton calibration chip constants to corresponding pulser constants: **a)** pulser constants *versus* krypton constants (solid line: $y = x$), and **b)** the distribution of distance of the data points from the $y = x$ line.

Pulser Calibration: the Method

The pulser calibration is a specific NA49 method devised to proceed to a pad-per-pad calibration of the TPC electronics. Roughly, the procedure is the following: all the field wires in the TPC are given the same calibrated pulse. This induces a pad charge q_n (n being the pad no.), proportional to the pad gain. Consequently, we obtain a multiplicative calibration constant $c_n = <q>/q_n$, where $<q>$ is the average charge induced on a single pad. We expect the calibrated pad charge

$$q_n^{\text{corrected}} = c_n \cdot q_n^{\text{measured}}$$

to be corrected for electronics gain variations.

An important feature of the electronics pulser calibration is that giving the same pulse to the wires constitutes a different electronics load than the one from electron clusters coming from charged particle tracks. Instead of a local load of a few pad channels during some finite time, one gets a uniform load of all the pads and of all the time buckets. This difference in load conditions may appear important for the calibration, and its possible influence has to be cross-checked. This is where the krypton method comes in.

Comparison to Krypton Calibration Constants

Pulser calibration pad constants c_n and krypton chip constants k_i being not directly comparable, a simple recalculation has been performed on VTPC-2 pulser constants and a set of "chip pulser constants, averaged to 1 over sector" has been produced. These constants will be referred to as $\tilde{c}_i$. This new set has been compared to a corresponding set of krypton chip constants. Fig. 47 shows a comparison similar to the one presented in Fig. 44. Though a correlation is visible between the data points and the $y = x$ line, the distribution of the points around the line has an RMS of an order of 3%. This is an order of magnitude above the internal statistical consistency of the krypton method (about 0.4%), presented in Section A.2.4.

In principle, a difference between results of the pulser and krypton calibration, as the one shown in Fig. 47, could be explained by gas gain variations: the krypton constants are supposed to take care of both gas gain and electronics response fluctuations, and the pulser constants of the electronics

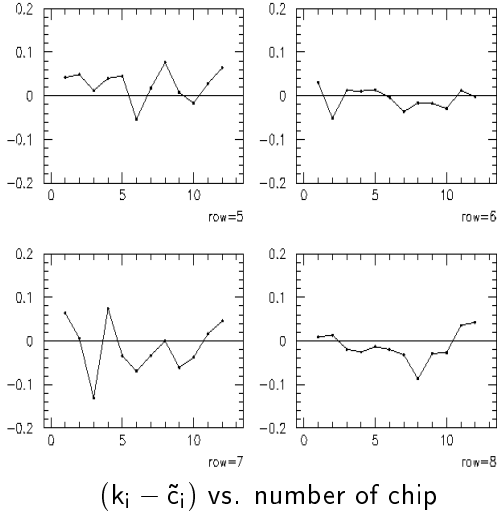$(k_i - \tilde{c}_i)$ vs. number of chip

Figure 48: Deviation of krypton chip calibration constants from corresponding pulser constants, plotted *versus* the chip position along the pad row (VTPC-2, sector no. 1).
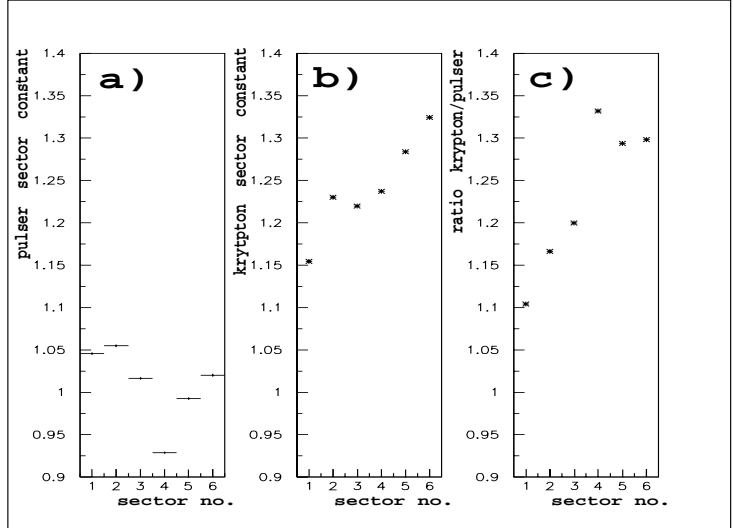
Figure 49: Comparison of pulser and krypton calibration at sector level: **a)** VTPC-2 pulser sector constants, **b)** corresponding krypton sector constants, and **c)** the ratio of krypton constants over pulser constants.

variations only. This is why a more detailed comparison has been performed and is presented in Fig. 48. As shown in the Figure, the difference between krypton and pulser constants can show "jumps" from one chip to another, their magnitude going up to 20%. This is far too much for what one would expect from gas gain variations. One has to conclude that either there is no good consistency between the two methods, or the pulser electronics calibration constants have very large statistical fluctuations.

In order to complete the picture, an additional study has been accomplished at the sector level. This time, average "pulser sector constants" have been computed and compared to krypton sector constants (Sec. A.2.3). The result (for VTPC-2) is presented in Fig. 49. As one can see from the Figure, the two sets of constants show a very different behaviour. Thus, also at sector level, the two methods give large discrepancies.

The analysis presented above leads to the following conclusion: assuming a reasonable statistical accuracy of the pulser calibration, the two methods show large discrepancies both at the chip and at the sector level. This cannot be explained uniquely by gas gain variations. The problem can be understood as consequence of different conditions in electronics load, described above. Here the krypton calibration comes closer to true experimental conditions, as it is based on electron cluster charge and not on a uniform pulser load.

The above study has lead to the decision of performing the gain calibration of the NA49 TPC system only on the basis of the krypton method, without including the pulser method in the procedure.

A.3.2 Investigation and calibration of gain variations

This Section describes the behaviour of gain variations in the NA49 TPC's, together with exemplary results of krypton calibration, which has been performed on all four chambers. The gain fluctuations will be described in three steps: at sector level, chip level and inside the chips. The results obtained will be mostly presented on the example of VTPC-2 and MTPC-R.

Sector Level

Although the gain differences between sectors are not supposed to be taken out by krypton calibration, their magnitude has been investigated. Fig. 50 shows the sector constants computed from MTPC-R
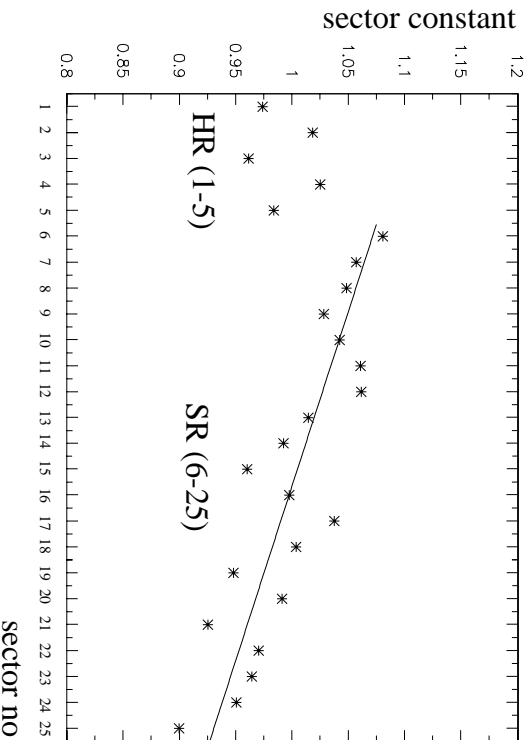
64

Figure 50: Krypton sector constants for the MTPC-R, plotted *versus* sector number. The constants are rescaled to give an average 1 over the entire chamber. Constants corresponding to High Resolution and Standard Resolution (HR/SR) sectors are indicated. A tentative linear slope is drawn through SR sector constants.
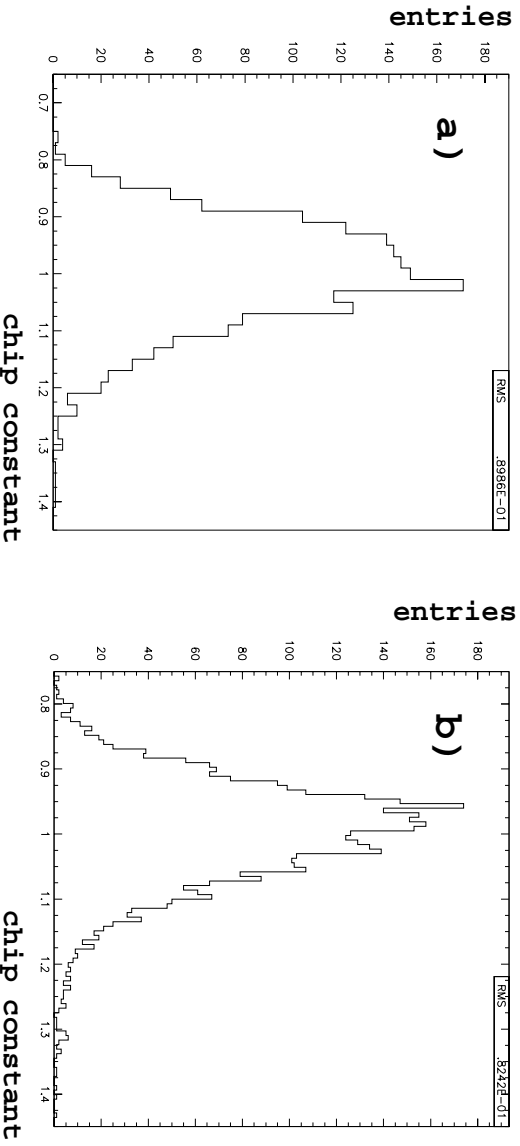

Figure 51: Distributions of chip calibration constants for **a)** VTPC-2 and **b)** MTPC-R.

krypton data. The two types of sectors: High Resolution and Standard Resolution, are indicated in the plot. Due to differences between HR and SR sectors, these two groups of constants are not directly comparable (note that HR and SR sectors differ by nominal HV settings, as well as by other parameters [45]). On the other hand, the comparison of sector constants *within* the SR group indicates a systematic trend which might be tentatively described by a linear slope giving an overall gain difference of about 15%. The relative SR sector gain decreases when approaching to the beam. On top of this systematics we see local sector to sector gain fluctuations of an order of a few percent.

Chip Level

Overall magnitude of variations. Fig. 51 shows distributions of two sets of chip calibration constants. The constants being averaged to 1 over sector (Sec. A.2.3), the width of the distributions gives an estimate of gain fluctuations between chips in a single sector. For both distributions the RMS is of an order of 10%. Note that the fluctuations shown in the Figure come from both gas gain and electronics response variations.
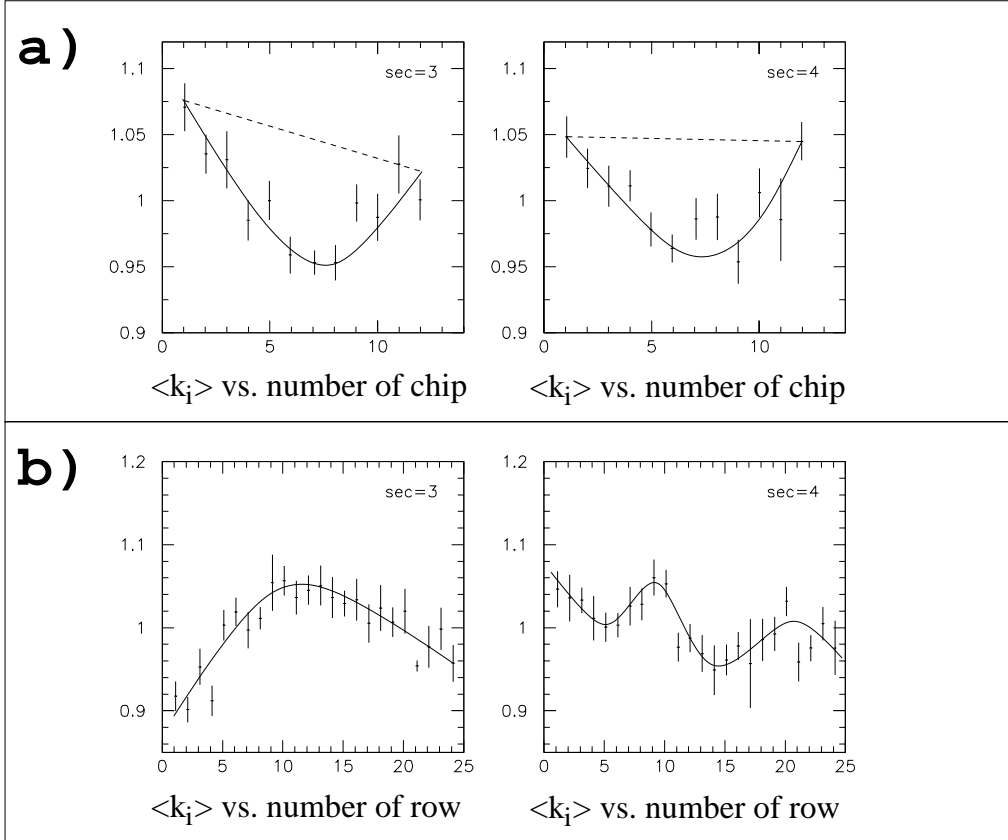
Figure 52: **a)** Pad direction systematics for two sectors of the VTPC-2: chip constants averaged over all rows *versus* the chip position along the row. **b)** Beam direction systematics for the same two sectors: chip constants averaged over an entire row *versus* the row number. Note: "eye-guiding" lines and curves are discussed in the text. The error bars reflect the variation of gain in the direction of averaging.

Pad and beam direction systematics. The investigation of systematic trends in TPC gain allows one to look for various mechanical distortions and imperfections in construction of the detector. Such studies are particularly interesting as there is a possibility that gravitational or electrostatic forces in the readout chambers of the NA49 TPC's may be strong enough to distort the position of the sense wires, and therefore to change the gas gain.

Fig. 52a shows the calibration constants systematics in the pad direction (i.e., followed along the pad rows) for two exemplary VTPC-2 sectors. The shape of the dependence of the constants on the chip position in the row can be described by a superposition of a straight line and a "parabola-like" curve. This means that the gain is going up in the centre of the row, and that on top of this, it presents some linear-like dependence on chip position. Both effects may be sizable, of an order of 5-10%.

A possible explanation for the linear inclination would be an imperfection in parallelism between the Frisch wires and the sense wires of the TPC, or between the sense wires and the pad plane. The parabola-like curve might be explained by sagging of the sense wires, forming a catenary line inclined either up or down[7]. Both the parallelism imperfection and the wire sagging would need to have a magnitude varying from sector to sector. This is possible.

Apart from pad direction systematics, the beam direction systematics of the constants has been studied. An example of the obtained results is shown in Fig. 52b. Here significant effects of an order of 10-15% gain variation are also visible, but the shape of the systematics varies from sector to sector. Sometimes the observed effects can be explained quite simply. For example, the effect seen in sector no. 3 can be explained by an imperfection in parallelism of the two halves of the pad plane, glued together in the centre of the sector.

One should remember that mechanical imperfections are not the only possible explanation for

---

[7]Note that both directions are possible, due to the presence of both gravitational and electrostatic forces.
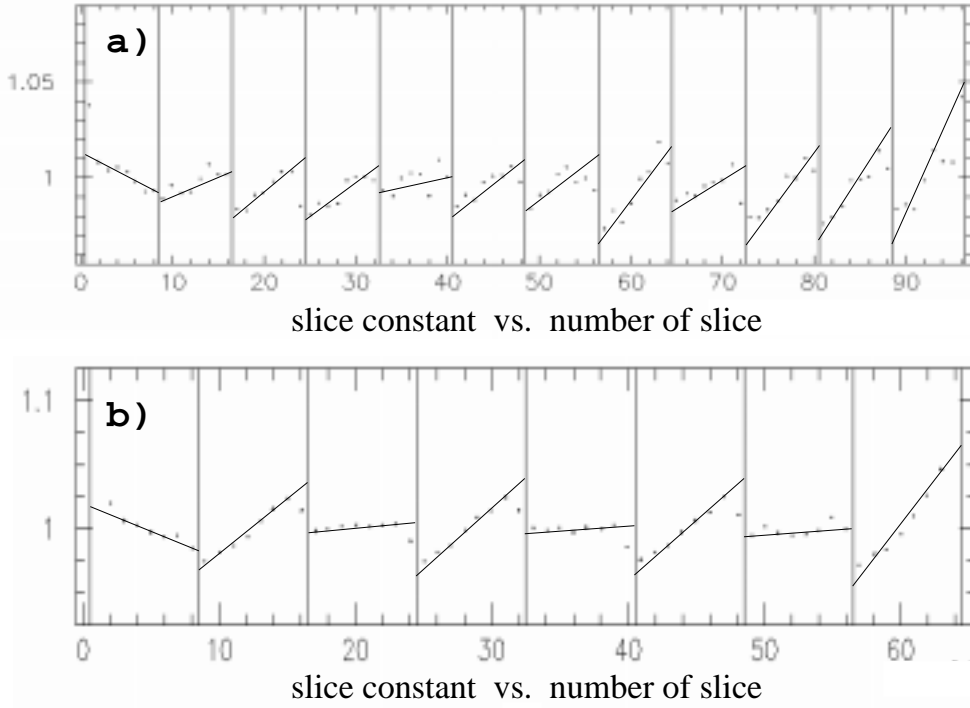
Figure 53: Dependence of slice constants on their position along the pad row, for **a)** the 2nd half of a VTPC-2 sector and **b)** a MTPC-R sector. The constants are plotted *versus* the number of the constant in the row, each constant corresponding to two pads. Chip limits (vertical lines) and roughly evaluated linear slopes are also shown in the plot.

the effects presented above. Another explanation would be some systematics in the TPC readout electronics.

Gain Variations Inside Chip

As has been stated in Sec. A.2.3, noticeable gain variations are present for pads belonging to the same TPC chip. This is common to all the four chambers. A dedicated study has been accomplished in order to investigate the behaviour of these variations and to find a reasonable way of appropriate calibration. Here we show the results of this study.

In order to explore the fluctuations *inside* chips, the gain differences *between* chips had to be taken out. This is why the analysis has been performed on krypton data calibrated for chip to chip variations. Slice constants (see Sec. A.2.3 and Fig. 42) have been produced in order to study the inside-chip gain systematics.

Fig. 53 shows the dependence of the slice constants on their position along the pad row, for two exemplary sectors. This dependence has several important features:

- the overall magnitude of the inside-chip systematics is significant, of an order of several percent;
- the slice constants dependence (and therefore the gain dependence) on pad position in the chip can be roughly approximated by a linear slope;
- the slopes very often show a "1-2 structure", that is, we observe a regular succession of flatter and steeper slope;
- an overall "left-right" increase of slope value is sometimes visible (VTPC-2);
- "edge effects", i.e., a negative and a large positive slope value are visible for the first and the last chip.

It should be pointed out that the behaviour described above cannot be explained by gas gain variations, but only by some systematics in the readout electronics. In particular, it is not possible to describe the mentioned "edge effects" by geometrical effects (that is, by an attenuation of the measured charge
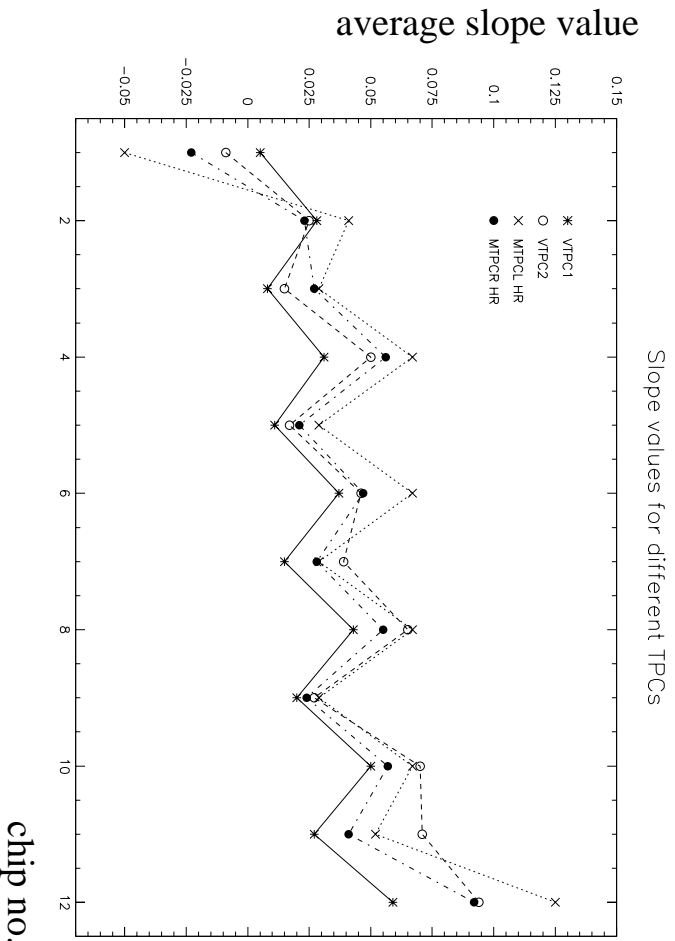
average slope value

chip no.

Figure 54: Average slope values *versus* the chip position in the pad row. For MTPC's, slope values from High Resolution sectors are shown.

of krypton clusters on the edge of the pad row), the cluster spatial extent being much too small for this. The only explanation seen for now is some "electronics edge effect".

Now comes the problem of how similar is the systematic behaviour for the various TPC's. In order to investigate this, average slope values have been calculated for the four chambers. The averaging went in the following way: for VTPC's, all the slopes from chips with a given position in the row from all the sectors have been averaged[8]. For MTPC's, slopes from the HR and SR sectors have been averaged separately. A comparison of these average slope values is presented in Fig. 54 (for MTPC's, HR sectors are shown). As one can see in the Figure, the overall systematics presents a very similar behaviour and the slope values stay relatively close to each other. This proves that the effects shown in Fig. 53 are common to all the four TPC's.

Now the procedure of calibration of the above inside-chip gain variations (the "linear chip correction" from Sec. A.2.3) can be discussed. As has been already stated, this procedure is limited to the elimination of systematic effects, leaving the statistical fluctuations uncalibrated. It consists in applying a linear gain correction to the raw data, each pad signal being multiplied by an appropriate correction factor which depends linearly on the pad position in the chip. This linear correction is directly given by the average slopes from Fig. 54.

Here a comment should be made why the calibration procedure has to resort to the above average linear slopes, and not, for instance, to appropriately averaged slice constants. There is one important reason for which a calibration based on slice constants will not be completely reliable. It can be presented as follows: imagine a slice constant situated at the right edge of a chip. It is calculated from a charge spectrum coming from krypton clusters with their centre of gravity on a pad belonging to the appropriate slice. The problem is that the cluster size being on the average about four pads, certain pads in the clusters may belong to the neighbouring chip. With the supposed linear behaviour of gain inside chips, this will result in an increase of the measured total cluster charge, and consequently in a shift of the value of the slice constant (down from the linear slope). Likewise, a shift upwards from the linear slope may take place for a constant at the left edge of the chip. Such effects are visible in Fig. 53.

---

[8]I.e., the averaging went over all chips no. 1 in all the rows in all the sectors, over all chips no. 2, etc. Note that we define the numerical value of each slope from Fig. 53 as "increase over chip", i.e. as the increase observed between the left and right chip border.
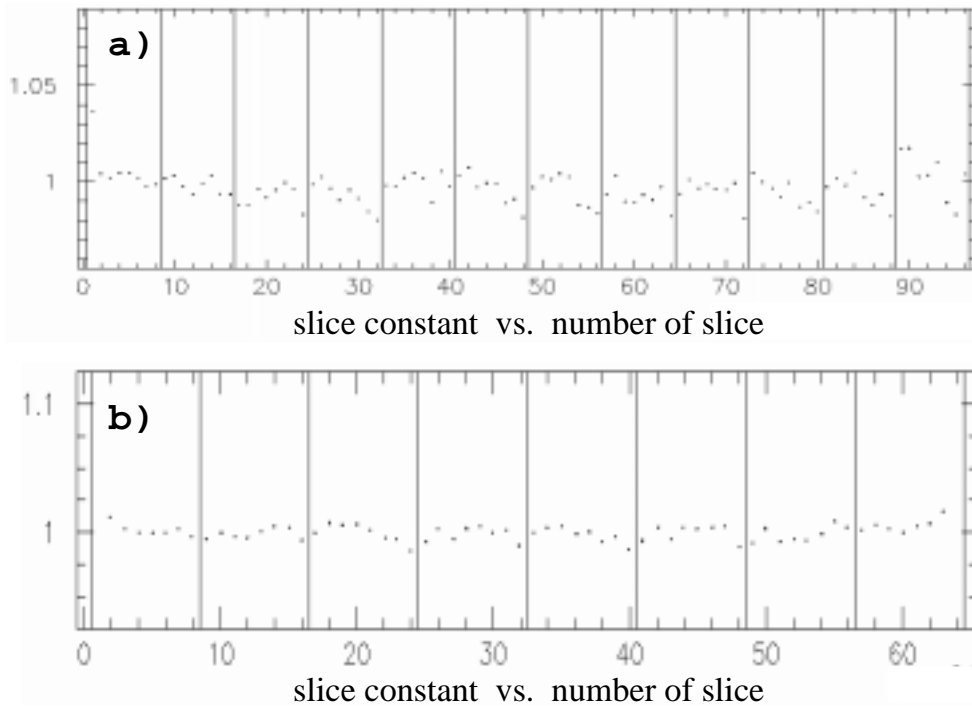
Figure 55: Slice constants obtained from fully calibrated krypton data, plotted *versus* their position along the pad row. The Figure illustrates **a)** the 2nd half of a VTPC-2 sector and **b)** a MTPC-R sector. Note: the same two sectors as in Fig. 53 are presented. Chip limits (vertical lines) are also shown in the plot.

Results of Calibration

Here a few exemplary results of the overall krypton gain calibration of the four NA49 TPC's are presented. All of them come from standard cross-check studies performed on calibrated krypton data in order to investigate the consistency of the method. These krypton data were calibrated using the full two-step procedure described in Sec. A.2.3; the same procedure is applied to NA49 physics data.

Remnant fluctuations inside chips. In order to study the efficiency of the linear chip correction, slice constants have been computed from krypton data calibrated for both gain fluctuations between chips and systematic inside-chip gain variations. Fig. 55 shows the dependence of these constants on their position in the pad row. Clearly, some remnant fluctuations are left at this inside-chip level. An over-calibration (i.e. a change in the slope sign) is also sometimes visible. All of this is to be expected, the linear correction being supposed to remove only the systematic variations. On the other hand, comparing this with Fig. 53, we observe a significant improvement and a general "flattening" of the gain.

Overall resolution improvement. Fig. 56 shows the distributions of chip constants used in the calibration procedure, together with distributions of the slice constants discussed above. The chip constants are an estimate of gain variations between chips for a single sector; the width of the distribution is probably a good approximation of the size of overall gain fluctuations[9]. On the other hand, the slice constants are obtained from fully calibrated data. Thus, they are an estimate of the remnant gain variations inside chips, which are the only fluctuations left after the calibration has been applied.

What can be concluded from the Figure is that, generally, the full krypton calibration gives an improvement of very roughly a factor of 8.5 (the dispersion ratio) for gain variations inside sectors. The magnitude of the remnant fluctuations can be estimated at about 1%.

---

[9]Gain differences between chips are obviously not the only gain fluctuation in the sector, but the analysis presented in the preceding paragraphs indicates that the magnitude of variations inside the chips is much smaller than between the chips.
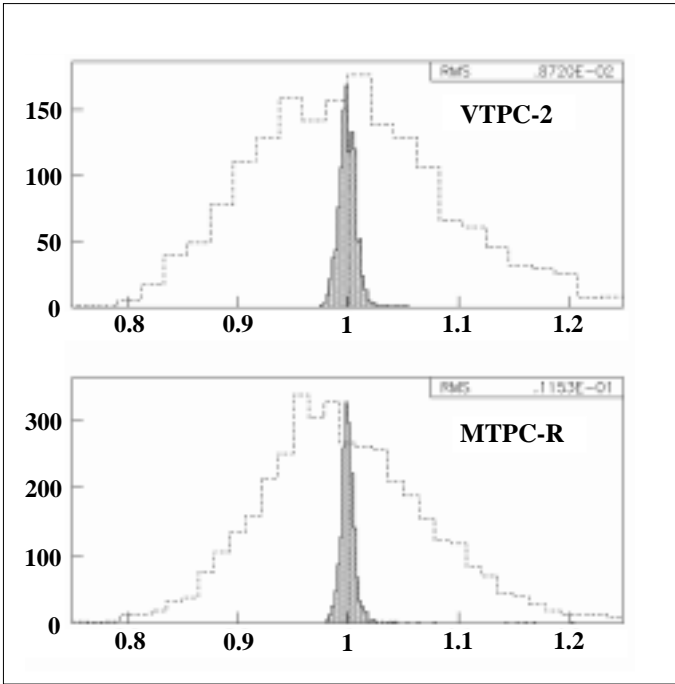
Figure 56: Distributions of slice constants obtained from fully calibrated data (solid) together with chip calibration constants (dashed). Note the different binning of the two distributions.
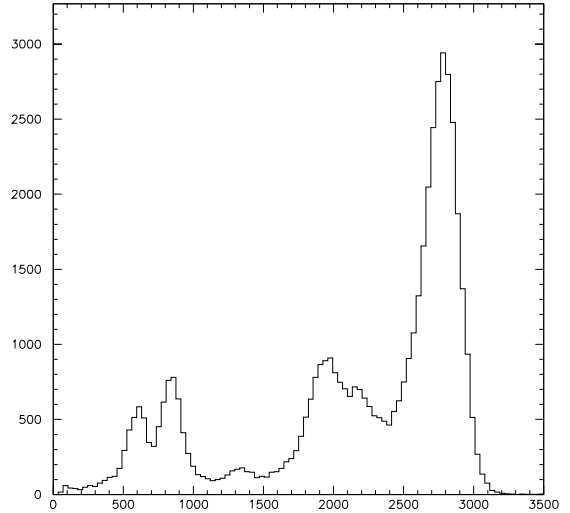

Figure 57: Fully calibrated cluster charge spectrum from one MTPC-L sector. The charge is measured in ADC units. The same sector as in Fig. 40 is shown.

Calibrated krypton spectrum. Fig. 57 shows a single-sector cluster charge spectrum produced from fully calibrated MTPC-L krypton data. Comparing it to Fig. 40, we see a considerable improvement in the spectrum quality: the distribution is much less distorted and the various peaks are far better distinguishable. While the obtained resolution is still worse than what comes from the Monte-Carlo shown in Fig. 38b, this is to be expected. The Monte-Carlo does not include all the detector effects present in the TPC's, and we know that after calibration, we are still left with some remnant fluctuations of the TPC gain.

Obviously, the results shown in Figs. 55-57 constitute only a partial test of efficiency of the krypton calibration method. The ultimate proof of efficiency and correctness of all the ingredients of the dE/dx calibration procedure is the resulting PID performance of the detector, described in Ch. 1.

A.4 Summary

The usage of the radioactive ^{83}Kr isotope provides a high-granularity calibration of gain variations in the NA49 TPC system. The calibration is performed at a single chip level. Additionally, the main systematics of gain variations inside the chips is taken out. The original gain variations are reduced by roughly a factor of 8.5, leaving remnant fluctuations of about 1%.

The procedure takes care of both electronics response and gas gain variations. The comparison with the pulser calibration method indicates that electronics load conditions are important for the calibration. The advantage of the krypton method is that it is based on electron cluster charge, which is close to true experimental conditions.

The high granularity of the method allows for a detailed study of gain systematics in the chamber. This allows one to look for various mechanical imperfections and distortions in the construction of the detector, and for systematic effects in the TPC readout electronics.

Due to space limitations, only a part of applications of the krypton method has been presented in this Appendix. Among other applications, the most important is the analysis of TPC gain over extended time periods, which has provided a detailed control of the NA49 detector stability over many years of data taking.

Appendix B. Specific Problems in Baryon Number Transfer Studies

In this Appendix, two problems are discussed which have not been included in Ch. 2. These are: the construction of the N+N elementary reference curve for net proton spectra in Pb+Pb collisions, and the sensitivity of the presented results to the assumptions made in the baryon number transfer study.

B.1   The N+N curve

In order to provide a correct elementary reference for the Pb+Pb collision, we construct the fictitious "N+N" reaction. The "nucleon" N reflects the isospin content of the Pb nucleus:

$$N = 0.39p + 0.61n$$

Let us label the spectrum of net protons originating from this reaction by $N + N \to p$. The two-component picture discussed in Ch. 2 implies that the projectile component of this spectrum is independent of the target hadron. Thus, for the projectile component, the following can be written:

$$N+N \to p \;\;\equiv\;\; N(projectile)+N(target) \to p \;\;=\;\; N(projectile)+any\ hadron \to p \;\;\equiv\;\; N+h \to p$$
$$(B.1)$$

where the last equivalence serves uniquely to simplify the notation. The $N + h \to p$ term can be imagined as composed of two contributions:

$$N + h \to p \;\;=\;\; 0.39(p + h \to p) \;\;+\;\; 0.61(n + h \to p) \qquad (B.2)$$

Note that these contributions can be attributed to the projectile components of net proton spectra in p+h and n+h collisions. The projectile component being target-independent, isospin symmetry gives

$$n + h \to p \;\;=\;\; p + h \to n \qquad (B.3)$$

None of the terms in Eqs. B.1- B.3 depends on the target hadron h, so $h = p$ can be assumed. Thus, Eqs. B.1- B.3 give the following for the N+N projectile component:

$$N + N \to p \;\;=\;\; 0.39(p + p \to p) \;\;+\;\; 0.61(p + p \to n) \qquad (B.4)$$

In other terms, the projectile component of the net proton spectrum in N+N collisions can be obtained from a weighted sum of projectile components of p+p net proton and net neutron spectra. For the symmetric N+N collision, exactly the same conclusion can be obtained for the target component. Thus, Equation B.4 holds also for the total N+N net proton spectrum.

B.2   Assumptions and corresponding uncertainties

B.2.1   Asymmetric $B\bar{B}$ production

At least for $x_F < 0.2$, the baryon number transfer studies presented in Ch. 2 rely uniquely on net proton $(p - \bar{p})$ spectra. However, in Sec. 2.1.2, a non-zero projectile component of the $p - \bar{p}$ distribution in π+p collisions has been attributed to asymmetric $B\bar{B}$ pair production. In this specific case, the net proton spectrum is not a fully correct measure of the transfer of baryon number from the proton target to the final state baryon - a contribution of $B\bar{B}$ pair production remains in this spectrum even after $\bar{p}$
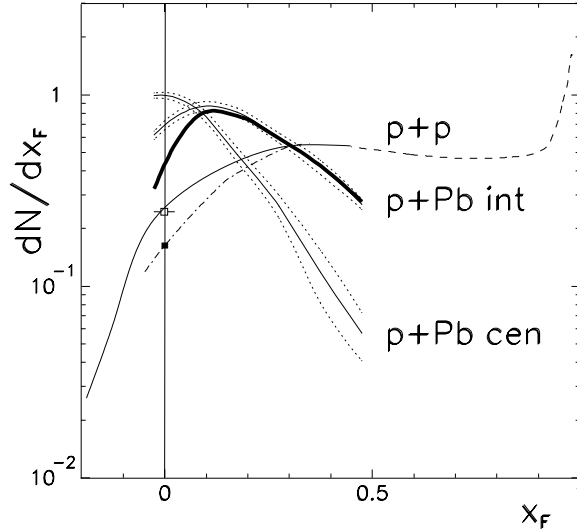
Figure 58: Sensitivity of the p+p and p+Pb results obtained in Ch. 2 to assumptions made in the study. The thin solid curves correspond to projectile components of net proton spectra from Figs 17a and 21 (extended to the forward p+p region by means of the dashed curve). The thick solid, dotted, and dash-dot curves give estimates of their uncertainties, as described in the text.

subtraction. In principle, a similar situation could happen also in p+p and p+A collisions, where the projectile is not isospin-symmetric. For simplicity, the discussion in Sec. 2.2 contains the assumption that this latter problem can be neglected. Let us investigate the importance of this assumption. If the $p - \bar{p}$ spectrum were still contaminated by additional pair produced protons, how would that change the uniform picture of baryon number transfer presented in Ch. 2?

In p+p reactions at 158 GeV beam energy, the $\bar{p}/p$ ratio at $x_F = 0$ is roughly 0.25, and goes smoothly to 0 at $x_F \approx 0.3$. Assuming a very extreme situation, in which the number of pair produced protons would be *twice* that of antiprotons, the correct subtraction procedure would imply $p - 2\bar{p}$ instead of $p - \bar{p}$. At $x_F = 0$, the projectile component of this "correct net proton spectrum" would go down by 33%. It would not change at $x_F \approx 0.3$. On this basis, a tentative (dash-dot) curve has been drawn in Fig. 58. In the extreme case assumed here, that would be the correct curve to reflect the transfer of projectile baryon number to the proton final state. The uncertainty induced by this problem is given by the difference between the dash-dot and solid p+p curves. In p+Pb reactions, the $\bar{p}/p$ ratio does not exceed that observed in p+p, so the same could be expected for the uncertainty of the spectra. For Pb+Pb collisions, this problem would be less important - the Pb nucleus is nearly isospin-symmetric.

It is hoped that more insight into this problem will be provided by dedicated studies made by NA49. Preliminary results of such studies are presented in [52].

B.2.2   Centrality definition in p+Pb and π^++Pb reactions

The target subtraction procedure in p+Pb collisions (Sec. 2.2.2) assumes that the same n_{grey} selections in p+Pb and π^++Pb reactions correspond to the same $<\nu>$ values. This simplest assumption does not have to be correct. For instance, the $<\nu>$ values which the VENUS model gives for the two considered samples of π^++Pb collisions are lower by ca. 25% than for p+Pb samples obtained by the same n_{grey} selections.

In principle, the presented study could rely on a given model (like VENUS), and use n_{grey} selections such as to obtain identical VENUS $<\nu>$ values. There are two reasons why this has *not* been done. First, no π^++Pb sample corresponding to $<\nu> \approx 6$ could have been isolated. Second, the obtained $<\nu>$ values would anyway depend on the scenario which the model assumes for grey proton production. Only a model describing in very great detail the centrality dependence of h+A collisions could be expected to give reliable results[1].

---

[1] The VENUS 4.12 version of the model used in this study does not fulfil the severe requirement mentioned above [29].

A *model-independent* estimate of corresponding uncertainties is difficult. Below, it is judged by the difference between the results obtained as suggested by VENUS and using our simple n_{grey} selection. For the intermediate p+Pb sample ($0 \leq n_{grey} \leq 3$), the π^++Pb selection suggested by VENUS is $3 \leq n_{grey} \leq 5$. The analysis has been repeated using this π^++Pb sample for target subtraction. The result is presented in Fig. 58 by means of the thick solid curve. A comparison with the corresponding thin solid curve gives an idea of the uncertainty induced by the problem.

Further insight could be gained here by comparing the results obtained by many different models of h+A reactions. Another idea would be to construct a model on the detailed basis of centrality-selected NA49 and E910 data.

B.2.3 The π^++Pb projectile component

In the extraction of the p+Pb projectile component (Sec. 2.2.2), the $\pi^\pm$+Pb curves used for target subtraction are obtained on the basis of π^++Pb spectra. The procedure assumes that the π^++Pb projectile contribution to these spectra is constant with centrality and identical to that in π^++p collisions. In reality it could change size and shape.

In order to estimate the corresponding uncertainties, two exercises have been made: the target subtraction has been repeated assuming the π^++Pb projectile component has *vanished*, and assuming it has *doubled*. Fig. 58 illustrates the results of this study for both intermediate and central p+Pb projectile components (dotted curves). These give an idea of the induced uncertainty.

The problem will be soon fully clarified. The $\pi^\pm$+Pb curves will be extracted experimentally using new NA49 data on π^-+Pb reactions. These new data were taken in late 2001 and will be soon available for analysis.

B.2.4 Conclusions

The lack of knowledge about specific phenomena discussed above introduces several uncertainties to the results of the study made in Ch. 2. Their importance depends on x_F and reaction type. It may be sizeable in the central region. However, none of them seems large enough to cause important modifications of the general uniform picture of baryon number transfer in p+p, p+Pb and Pb+Pb reactions, which has been presented in Fig. 21.

Acknowledgements

Bibliography

[1] G. Białkowski, R. Sosnowski, "Reggego metoda", and G. Białkowski, R. Sosnowski, S. Gąsiorowicz, "Reggego model", in: "Encyclopaedia of Physics", Państwowe Wydawnictwo Naukowe, Warszawa 1972 (*in Polish*).

[2] D. H. Perkins, "Introduction to High-Energy Physics," Polish edition: Państwowe Wydawnictwo Naukowe, Warszawa 1989 (*in Polish*).

[3] G. Białkowski, R. Sosnowski, "Cząstki elementarne", Państwowe Wydawnictwo Naukowe, Warszawa 1971 (*in Polish*).

[4] K. Fiałkowski and W. Kittel, Rept. Prog. Phys. **46** (1983) 1283.
(A description of the "sea-gull effect" can be found in p. 1382.)

[5] A detailed review can be found in:
A. Capella, U. Sukhatme, C. I. Tan and J. Tran Thanh Van, Phys. Rept. **236** (1994) 225.
A simplified description can be found in e.g.:
M. Różańska, Institute of Nuclear Physics Internal Report 1524/PH, Kraków, 1991 (*in Polish*).

[6] B. Andersson, G. Gustafson and B. Nilsson-Almqvist, Nucl. Phys. B **281** (1987) 289.
B. Nilsson-Almqvist and E. Stenlund, Comput. Phys. Commun. **43** (1987) 387.

[7] K. Werner, Phys. Rept. **232** (1993) 87.

[8] S. Fredriksson, G. Eilam, G. Berlad and L. Bergstrom, "High-Energy Collisions With Atomic Nuclei. Part 1," TRITA-TFY-84-06, May 1984.

[9] S. Mrówczyński, Acta Phys. Polon. B **29** (1998) 3711, and references therein.

[10] U. W. Heinz and M. Jacob, arXiv:nucl-th/0002042.

[11] A. Capella, Acta Phys. Polon. B **30** (1999) 3541.

[12] For a review of more recent A+A data, see e.g.:
"Quark matter '99. Proceedings...", ed. L. Riccati *et al.*, Nucl. Phys. A **661** (1999) 1c,
and references therein.

[13] S. Afanasev *et al.* [NA49 Collaboration], Nucl. Instrum. Meth. A **430** (1999) 210.

[14] G. E. Cooper [NA49 Collaboration], Nucl. Phys. A **661** (1999) 362c.

[15] S. V. Afanasev *et al.* [NA49 Collaboration], CERN-SPSC-2001-008.

[16] C. Caso *et al.* [Particle Data Group], "Review of Particle Physics", Eur. Phys. J. C **3** (1998) 1.

[17] B. A. Cole [E910 Collaboration], Nucl. Phys. A **638** (1998) 423c.

[18] Unpublished preliminary NA49 data, partially available in:
G. H. Arakelian, A. Capella, A. B. Kaidalov and Y. M. Shabelski, arXiv:hep-ph/0103337.

[19] Preliminary NA49 data. Some results of this analysis have been published in:
J. Bächler *et al.* [NA49 Collaboration], Nucl. Phys. A **661** (1999) 45c.

[20] Unpublished preliminary NA49 data, presented by
A. Rybicki [NA49 Collaboration] at CERN Heavy Ion Forum, 18 Oct. 2000.

[21] A. Rybicki, "Study of particle yields using dE/dx fits", NA49 Internal Note 191,
available on the Internet via the NA49 Home Page: http://na49info.cern.ch

[22] Vertex and trigger losses: O. Chvála, MFF UK Prague, Ph.D. Thesis in preparation,
Hyperon feed-down: M. Kreps, Comenius Univ., Bratislava, Ph.D. Thesis in preparation.

[23] "GEANT, Detector Description and Simulation Tool", CERN Program Long Writeup W5013.

[24] J. Whitmore, S. J. Barish, D. C. Colley and P. F. Schultz, Phys. Rev. D **11** (1975) 3124.
J. Whitmore, Phys. Rept. **10** (1974) 273.
M. G. Albrow *et al.*, Nucl. Phys. B **108** (1976) 1.
M. G. Albrow *et al.*, Nucl. Phys. B **73** (1974) 40.

[25] D. Varga, RMKI Budapest, Ph.D. Thesis in preparation.

[26] W. Busza, Nucl. Phys. A **418** (1984) 635c.

[27] H. Boeggild *et al.*, Nucl. Phys. B **72** (1974) 221.

[28] A. Białas, M. Bleszyński and W. Czyż, Nucl. Phys. B **111** (1976) 461.

[29] A. Rybicki *et al.* [NA49 Collaboration], Proc. XXXIVth Rencontres de Moriond:
'99 QCD and High Energy Hadronic Interactions, Les Arcs, France, March 20-27, 1999, p. 211.

[30] H. Grassler *et al.*, Nucl. Phys. B **132** (1978) 1.

[31] G. Jancso *et al.*, Nucl. Phys. B **124** (1977) 1, and references therein.

[32] J. Bartke *et al.*, Nucl. Phys. B **127** (1977) 269.

[33] D. Drijard, H. G. Fischer and T. Nakada, Nucl. Instrum. Meth. A **225** (1984) 367.

[34] M. Aguilar-Benitez *et al.* [LEBC-EHS Collaboration], Z. Phys. C **50** (1991) 405.

[35] D. Drijard *et al.*, Z. Phys. C **21** (1984) 321.

[36] J. D. Jackson, Nuovo Cim. **34** (1964) 1644.

[37] M. Deutschmann *et al.*, Nucl. Phys. B **103** (1976) 426.

[38] J. Bartke *et al.*, Nucl. Phys. B **107** (1976) 93.

[39] J. Bartke *et al.*, Nucl. Phys. B **137** (1978) 189.

[40] D. E. Groom *et al.* [Particle Data Group],
"Review of Particle Physics," Eur. Phys. J. C **15** (2000) 1.
(Relevant cross-sections are obtained from fits to existing data.)

[41] M. Schouten *et al.*, Z. Phys. C **9** (1981) 93.

[42] J. Bracinik, Ph.D. Thesis, Comenius Univ., Bratislava (2000), p. 111 (*in Slovakian*).

[43] T. Susa [NA49 Collaboration], Nucl. Phys. A **698** (2002) 491c.
See also: F. Antinori *et al.* [WA97 Collaboration], Nucl. Phys. A **661** (1999) 130c.

[44] B. B. Back *et al.* [PHOBOS Collaboration], Nucl. Phys. A **698** (2002) 54c.

[45] F. Bieser *et al.*, Nucl. Instrum. Meth. A **385** (1997) 535.

[46] P. Seyboth, "NA49 Numbering Conventions", NA49 Internal Note 37,
available on the Internet via the NA49 Home Page: http://na49info.cern.ch

[47] W. Blum *et al.*, The ALEPH Handbook, ALEPH 89-77 CERN, 1989.
D. Decamp *et al.* [ALEPH Collaboration], Nucl. Instrum. Meth. A **294** (1990) 121.

[48] A. De Min *et al.*, IEEE Trans. Nucl. Sci. NS-42 (1995) 491.

[49] C. Whitten, unpublished, "Note on Electron Energy Deposited at Sites of $^{83m}_{36}$Kr Decay"
(February, 1995).

[50] H. Enge, "Introduction to Nuclear Physics", Addison-Wesley World Student Series edition, 1972.

[51] W. Blum, L. Rolandi, "Particle Detection with Drift Chambers", Springer-Verlag Berlin Heidelberg 1993.

[52] H. G. Fischer *et al.* [NA49 Collaboration],
Proc. Cracow Epiphany Conference on Quarks and Gluons in Extreme Conditions,
Cracow, Poland, January 3-6, 2002, to appear in Acta Phys. Polon. B.